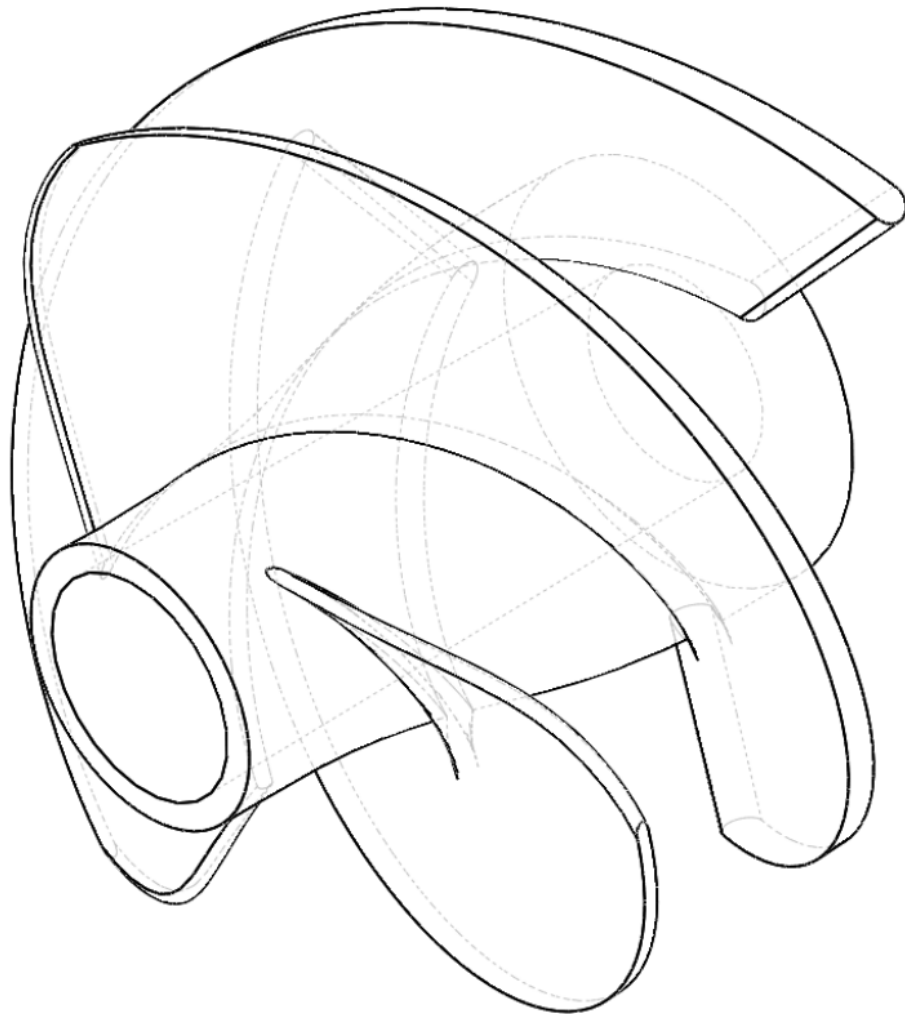


Rocket engine inducer design optimisation to improve its suction performance

M. J. Lubieniecki



Rocket engine inducer design optimisation to improve its suction performance

by

M. J. Lubieniecki

to obtain the degree of Master of Science
at the Delft University of Technology,
to be defended publicly on Friday December 7, 2018 at 14:00 PM.

Student number:	4617037
Project duration:	February 12, 2018 – December 7, 2018
Supervisors:	Dr. A. Cervone, Dr. C. Lettieri
Thesis committee:	Prof. E. K. A. Gill., TU Delft, Committee Chair Dr. A. Cervone, TU Delft, Supervisor Dr. M. Pini TU Delft

An electronic version of this thesis is available at <http://repository.tudelft.nl/>.

Acknowledgements

This thesis is the final chapter of my Delft adventure. I must admit that it surpassed all my expectations that I had when I arrived to Delft at the beginning of the Introduction Programme. During that adventure I met new friends, visited exciting places and fulfilled my dream of becoming a qualified Space Engineer. This would not be possible without the support of many people from many different countries.

First, I would like to thank my supervisors. Dr. Lettieri introduced me to the project and was a constant source of motivation and love to fluid dynamics. Experience of Dr. Cervone in cavitation research proved to be crucial during this project, especially when problems were encountered. Thanks to their guidance I was able to develop myself as a researcher and engineer.

My stay in Osaka certainly would not be possible without the support of Prof. Kawata and Prof. Miyabe from the Osaka Institute of Technology. They were always ready to help and discuss the project. Cooperation with them was a real pleasure. So was the work with all students of the Fluid Machinery Lab, who showed me Japan and supported in everyday activities. I owe special thanks to Kakio-San, Nakamura-San and Hayashi-San that thought me how to 3D print the pump and measure its characteristics. I hope that they learned something from me too and that we will have a chance to meet again.

Although the courses at TU Delft proved to be challenging, they also lead to many strong friendships. I am so happy that I could work with TU Delft students on so many different projects. I send special thanks to my beloved MicroSatelite group: Krishti, Sean and Serban. They thought me what the real team means. I am also thankful for the support of all my friends from Poland that didn't forget me during this time.

Finally, I want to express my gratitude to my family that made all of this possible and constantly supported me, even though they were not happy to see me so seldom. I hope that my achievements make them proud.

M. J. Lubieniecki
Delft, December 2018

Abstract

Turbopumps are essential components of every modern liquid-propellant engine. They are used to increase the static pressure of the propellants to deliver them to a high pressure combustion chamber. In order to achieve high power density and keep the pump mass as low as possible the pumps operate at high rotational speeds. The main limit to further increase the rotational speed is a phenomenon of cavitation. It is a process of vapour bubbles forming in a flow, which decreases pump performance and leads to flow instabilities. The inducer is an axial flow pump which pressurises the flow and suppresses cavitation before the main pump stage. Its design has a huge impact on suction performance of a turbopump that is its ability to maintain pressure rise while cavitation develops.

The main goal of this thesis was to optimise an inducer blade shape to improve its suction performance and propose new design guidelines for future turbopumps. In order to conduct the optimisation process a response surface based optimisation framework was established. A response surface is a mathematical model that approximates the relationship between the input parameters and the objective function from a finite number of learning points within the design space. The design space was defined by four parameters: sweep angle, sweep radius, incidence angle and blade solidity at the tip that controlled the blade shape. The performance of each design was evaluated with a CFD simulation established in a commercial solver. The optimisation goal was to minimise the critical cavitation number that corresponds to a 5% drop of pressure increase through the pump due to cavitation.

A starting point of the optimisation was the industrial pump designed by a Japanese company Teral. The results of the numerical optimisation show that the critical cavitation number was decreased by 17% with respect to the baseline design. Results of the simulations were validated by measuring the performance of both baseline and optimised design in a test facility of Osaka Institute of Technology. The inducers were 3D printed in ABS plastic and their wetted and cavitating characteristics measured. The tests confirmed that the optimised inducer can maintain its wetted performance at lower cavitation numbers. However the scatter in the measurements made the estimation of the critical cavitation number quite inaccurate. On average a 15.4% improvement was achieved.

Examination of the CFD results revealed that the performance improvement was achieved mainly by increasing the sweep radius and blade solidity. Increased sweep radius resulted in higher static pressure around the leading edge due to lower flow velocity in this region. Higher blade solidities allow the blade to operate better even with high cavity lengths. These conclusions were used to formulate a more detailed design guidelines for future inducers.

Contents

List of Figures	iii
List of Tables	vii
List of Symbols	x
1 Introduction	1
1.1 Relevance and motivation	1
1.2 Research questions and goals of the thesis	3
1.3 Report structure	4
2 Turbopump performance parameters and optimisation problem description	5
2.1 Notation.	5
2.2 Fundamental equations	6
2.3 Dimensional analysis and similarity laws.	8
2.4 Pump characteristic	11
2.5 Cavitation and suction performance	14
2.6 Optimisation problem statement	17
3 Baseline pump design	19
3.1 Pump overview	19
3.2 Meridional profile	21
3.3 Blade angle distribution	21
3.4 Blade thickness distribution	24
4 Optimisation framework	27
4.1 Framework overview.	27
4.2 Optimisation strategy	27
4.3 Parametrisation of inducer geometry	29
4.4 Design of Experiment	33
4.5 Geometry generation	34
4.6 Inducer design example	37
4.7 Meshing	39
4.8 Solver setup.	41
4.9 Baseline simulation results	42
4.10 Response surface	43
4.11 Optimisation algorithm	45
5 Optimisation results	47
5.1 Design space size.	47
5.2 Optimisation	48
5.3 Improved blade design optimisation.	52
5.4 Simulation verification	55
6 Performance improvement analysis	63
6.1 Geometry comparison	63
6.2 Inducer suction performance analysis.	65

7	Conclusions and recommendations	75
7.1	Conclusions	75
7.2	Recommendation for future work	76
A	Inducer design method	79
B	Test loop components specifications	87
	Bibliography	89

List of Figures

1.1	Turbopump specific power as a function of rotating speed for different rocket engines.	2
1.2	Cross-sections of two turbopumps: Rocketdyne Mark 3 and Vulcain 2 Turbopump with highlighted inducers and impellers.	3
2.1	Cylindrical coordinate system used to define blade and flow field coordinates. .	6
2.2	Generalised turbopump blade in meridonal view.	6
2.3	Inlet velocity triangle.	8
2.4	Outlet velocity triangle.	9
2.5	Ideal pump characteristic expressed in nondimensional parameters for several outlet angles.	12
2.6	Velocity triangles for different blade outlet angles.	13
2.7	Real pump characteristic.	13
2.8	Basic sources of losses in the centrifugal pump.	14
2.9	Cavitating characteristic at a fixed flow coefficient.	15
2.10	Cavitating characteristics at different flow coefficients.	16
2.11	Different possible types of cavitation in an open axial impeller	17
3.1	Main and splitter blades of the baseline impeller.	20
3.2	Side view of the baseline geometry.	20
3.3	Meridional profile of the baseline inducer.	21
3.4	Meridional profile of the baseline impeller.	22
3.5	Definition of β blade angle.	23
3.6	θ_B and β_B angles used to define blade shape.	23
3.7	Relationship between θ_B and β_B angles.	24
3.8	θ_B blade angle distribution of the baseline inducer.	24
3.9	β_B blade angle distribution of the baseline inducer.	25
3.10	Blade angle distribution of the impeller.	25
3.11	Blade thickness distribution of the baseline inducer design.	26
3.12	Blade thickness distribution of the impeller.	26
4.1	Optimisation framework overview.	28
4.2	Optimisation strategy: head coefficient at critical cavitation number σ_5 is maximised.	29
4.3	Parametrisation of a leading edge shape with sweep angle λ and sweep radius r_s . .	32
4.4	Blade chord length at the tip C and spacing between blades L used to define blade solidity.	32
4.5	Comparison of Latin Hypercube and Optimal Space Filling methods.	34
4.6	Leading edge and meridional profile reconstruction from the design parameters. .	34
4.7	Comparison between a) a blade curved at the tip and b) a blade with correct tip. .	35
4.8	Blade with no sweep and radial leading edge.	35
4.9	Blade with sweep and curved tip.	35
4.10	Blade with sweep and no curvature.	36

4.11	Graphical interpretation of the error between the hub and tip θ angle distributions.	37
4.12	Comparison between baseline and example inducer blade angle distributions.	38
4.13	Comparison between baseline and example inducer blade meridional profiles.	38
4.14	The division of the computational domain into three parts of the mesh: inlet with inducer, impeller and outlet.	39
4.15	Mesh topology in blade-to-blade view.	40
4.16	Solution convergence with increasing number of elements.	40
4.17	Two versions of the outlet: a) simplified for calculations, and b) the real volute.	41
4.18	Boundary conditions of the simulation.	42
4.19	Simulation results of baseline wet performance.	43
4.20	Simulation results of baseline suction performance.	44
5.1	Wet performance of sampled designs.	48
5.2	Suction performance of sampled designs as a function of sweep angle and sweep radius.	48
5.3	Suction performance of sampled designs as a function of incidence angle and solidity.	49
5.4	Response surface based on two parameters: sweep angle and sweep radius.	50
5.5	Refined response showing cavitating head coefficient based on two parameters: sweep angle and sweep radius.	51
5.6	Refined response showing efficiency based on two parameters: sweep angle and sweep radius.	52
5.7	Comparison between the suction characteristics of baseline and optimised design.	53
5.8	Comparison of the absolute circumferential velocity distribution at the outlet between the baseline and optimised inducer.	54
5.9	Position of the leading edge in the case of baseline, excel and modified design.	54
5.10	Wet head coefficient of the sampled inducers with the modified designs.	55
5.11	Response surface of the cavitating head coefficient based on sweep angle and radius.	56
5.12	Comparison of the cavitating characteristic between the baseline and the modified optimised inducer.	56
5.13	Test loop schematic.	57
5.14	Inlet pressure measurement position.	58
5.15	3D printed inducer and impeller.	59
5.16	Dimensions measured to verify the accuracy of the 3D printing process.	59
5.17	Simulated and measured wet characteristics of the baseline and optimised designs.	60
5.18	Simulated and measured efficiency of the baseline and optimised designs.	61
5.19	Simulated and measured cavitating characteristics of the baseline and optimised designs.	61
6.1	Comparison of leading edge and meridional shapes between the baseline and optimised design.	63
6.2	Comparison of the β blade angle distribution between the baseline and optimised design.	64
6.3	Comparison of: a) incidence angle b) outlet angle, between the baseline and optimised design.	65
6.4	Comparison of: a) slip angle b) absolute circumferential velocity at the outlet of the inducer, between the baseline and optimised design.	65
6.5	Simulated cavitating characteristic of baseline and optimised design.	66

6.6	Impeller cavitation number as a function of inducer cavitation number for baseline and optimised design.	66
6.7	Percentage of vapour volume in the flow channel a function of inducer cavitation number for baseline and optimised design.	67
6.8	Inducer head coefficient as a function of percentage of vapour volume in the flow channel for baseline and optimised design.	67
6.9	Isosurfaces of vapour volume fraction equal to 10% at two cavitation numbers: 0.111 and 0.050 for baseline and optimised design.	68
6.10	Total pressure rise distribution along the inducer blade without and with cavitation for the baseline and optimised design.	69
6.11	Blade loading distribution without cavitation at 95% of span for the baseline and optimised design.	70
6.12	Blade loading distribution at $\sigma = 0.050$ at 95% of span for the baseline and optimised design.	70
6.13	The distribution of minimal pressure coefficient along the leading edge span for the baseline and optimised design.	71
6.14	The distribution of minimal pressure coefficient along the leading edge span for the high and low sweep design.	72
6.15	Comparison of radial velocity distribution V_r at 75% of the span around the leading in blade-to-blade view.	72
6.16	Comparison of relative velocity distribution w at 75% of the span around the leading in blade-to-blade view.	73
6.17	Comparison of pressure coefficient C_p distribution at 75% of the span around the leading in blade-to-blade view.	73
A.1	Calculation of θ_0 angle from λ angle.	79
A.2	Calculation of θ_0 angle from sweep radius r_s	80
A.3	Example of leading edge shape for $\lambda = 40^\circ$ and $r_s = 40\%$ <i>span</i>	82
A.4	Coordinates of the most important points defining the meridional view of an inducer.	83

List of Tables

3.1	Design operating conditions of the baseline pump.	19
4.1	Optimisation requirements.	29
4.2	UP Plus 2 3D printer specifications.	30
4.3	Parameters defining the example design.	37
4.4	Pump operating conditions used during simulation.	41
4.5	CFX solver setup.	42
5.1	Design space size.	47
5.2	Quality of fit for two kinds of response surface.	49
5.3	Parameters of the first candidate points of the optimisation.	50
5.4	Comparison between the predicted and simulated performance of the first candidate designs.	50
5.5	Size of the refined design space.	51
5.6	Candidate points obtained from the refined response surface.	51
5.7	Comparison between the predicted and simulated performance of the candidate designs obtained from the refined response surface.	52
5.8	Parameters of the modified candidate design.	55
5.9	Comparison between the predicted and simulated performance of the modified candidate design.	55
5.10	Closed-loop testing rig specifications.	57
5.11	Measurements of the dimensions of baseline inducer after 3D printing.	59
5.12	Measurements of the dimensions of optimised inducer after 3D printing.	60
6.1	Comparison of the parameters defining the baseline and optimised design.	64
6.2	Parameters defining high and low sweep designs and simulated performance of these designs.	71
B.1	Inverter and test pump specifications.	87
B.2	Vacuum and booster pump specifications.	87
B.3	Inlet pressure sensor and differential pressure sensor specifications.	88
B.4	Differential pressure sensor (used for flow rate measurements) and torque transducer (used for efficiency measurement) specifications.	88

List of Symbols

Latin

a	[m]	Vertical dimension of an leading edge ellipse
b	[m]	Horizontal dimension of an leading edge ellipse
C_p	[-]	Pressure coefficient
C	[-]	Circumferential direction or chord length
c	$[\frac{m}{s}]$	Absolute fluid velocity
D, d	[m]	Diameter
F, f	[-]	Objective function
g	$[\frac{m}{s^2}]$	Earth gravitational acceleration
g_i	[-]	Inequality constraints (optimisation problem)
H	[m]	Pump head
h	$[\frac{J}{kg}]$	Enthalpy
h_j	[-]	Equality constraints (optimisation problem)
i	[°]	Incidence angle
L	[m]	Spacing between blades
\dot{m}	$[\frac{kg}{s}]$	Mass flow rate
Q	$[\frac{m^3}{s}]$	Volume flow rate
P	[W]	Power supplied to the pump
P_u	[W]	Useful power transferred to the fluid
p	[Pa]	Pressure
p_v	[Pa]	Vapour pressure
R, r	[m]	Radius or radial direction
r_s	[m]	Sweep radius
S	[-]	Fraction of a distance along a curve
S_s	[-]	Suction specific speed
s	[-]	Solidity
T	[Nm]	Torque
u	$[\frac{m}{s}]$	Blade velocity in circumferential direction
V_B	$[m^3]$	Volume of a single vapour bubble
w	$[\frac{m}{s}]$	Relative fluid velocity
x	[-]	Span fraction
X	[-]	Design vector
x^*	[-]	Optimisation problem solution
Z	[-]	Axial direction or coordinate

Greek

α	[°]	Absolute flow velocity angle or Optimisation step length
β	[°]	Relative flow velocity angle
β_B	[°]	Relative blade angle
Γ	[°]	Leading edge lean angle
δ	[°]	Slip angle
θ	[°]	Circumferential coordinate
θ	[°]	Absolute blade angle
λ	[°]	Sweep angle
η	[-]	Efficiency
ϕ	[-]	Flow coefficient
ψ	[-]	Head coefficient
σ	[-]	Cavitation number
ρ	$[\frac{kg}{m^3}]$	Fluid density
Ω, ω	$[\frac{rad}{s}]$	Pump rotational speed

Subscripts

1	blade or flow property at the leading edge
2	blade or flow property at the trailing edge
a	fluid velocity component in axial direction
r	fluid velocity component in radial direction
u	fluid velocity component in circumferential direction
m	fluid velocity component in meridional direction
s	static
t	total

Abbreviations

NPSP	Net Positive Suction Pressure
NPSH	Net Positive Suction Head
NPSE	Net Positive Suction Energy
RMAE	Relative Maximum Absolute Error
RMS	Root Mean Square Error

Introduction

1.1. Relevance and motivation

Liquid-propellant engines are essential parts of every launcher. They are used in heavy rockets delivering payloads weighing several tons to Earth's orbit, and in smaller launchers designed to carry satellites smaller than a shoebox. This popularity of liquid-propellant engines is a result of several advantages that they have over the other types of rocket engines. These include the ability control the thrust of the engine, higher specific impulse and reduced volume and mass of the propellant tanks that do not have to be pressurised. All these characteristics combined allow to build lighter and more efficient launchers what reduces the cost of launching payloads into space. However, this would not be possible without turbopumps that deliver the propellants from tanks to a high pressure combustion chamber. They are incredibly challenging machines because of the high required power output and resistance to extreme temperatures of cryogenic propellants. In addition, high performance must be achieved while keeping the mass of the pump as low as possible, what results in extremely high power density (power per unit mass) achievable in such engines. Figure 1.1 shows values of specific power for several rocket engine turbopumps as a function of their rotational speed. Values for a turbofan jet engine and a car engine are also presented to provide points of reference. It is clearly visible that specific power increases with rotational speed of the rotor. As higher specific power results in smaller and lighter pump it is beneficial to operate the pump at the highest possible rotational speed.

Unfortunately, increasing the rotational speed leads to increasing flow accerelation and higher static pressure drop near the leading edge of the blade. If this drop is sufficiently high, cavitation starts developing inside the flow channel. Cavitation is a process of vapour bubbles forming in the regions where static pressure of the flow decreases below the vapour pressure of a liquid at given temperature. As the volume of the vapour bubbles grows the pressure rise across the pump drops and instabilities occur that may even lead to a total failure of the pump. The limiting effect of cavitation on the further increase of the rotational speed was noticed soon after the start of liquid-rocket propulsion development. Already in 1958 Acosta [4] points out that the flow in a rocket engine pump cannot be cavitation free and the cavitation related requirements dominate the design of the inlet of such pumps. This lead to the search for the best way to suppress cavitation.

Nowadays every rocket engine pump is made of two major elements: an inducer and an impeller. Two examples of such designs are showed in Figure 1.2. The inducer is an axial stage placed

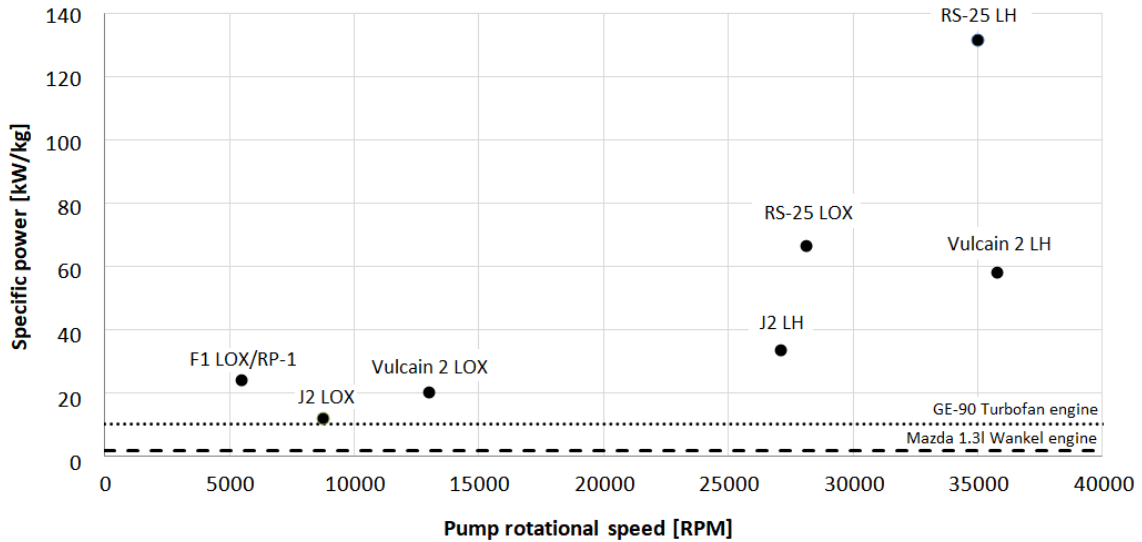


Figure 1.1: Turbopump specific power as a function of rotating speed for different rocket engines. [1–3]

upstream of the impeller. Its main task is to rise the static pressure to avoid caviatation in the impeller. The impeller is a main radial stage and provides more than 90% of the pressure rise through the pump. Many design guidelines were proposed to achieve a robust and high performance design of both components. Nevertheless, many doubts still arise when the relationship between the shape of the blade and the cavitating performance of a pump is considered. They are caused by the complexity of the 3D cavitating flow but also by the sheer number of possibilities of different blade shapes. At the same time the inducer blade shape of the blade has the biggest impact on cavitation in the pump [5]. A rapid development of the Computational Fluid Dynamics (CFD) allowed to speed up greatly the design process of complex pump geometries, as for the first time a relatively accurate prediction of the suction performance was possible. However, those methods alone are not sufficient to tell how the geometry should be changed in order to achieve even better performance. This disadvantage may be overcome by coupling numerical flow simulations with optimisation algorithms.

The thesis presented in this document aimed at exploiting the advantages of the CFD based optimisation to better understand the cavitating flow. This knowledge was used to form better design guidelines regarding the shape of the blades of the inducer. The research approach used in this project is best described as a case study. One particular case was analysed in depth to draw general conclusions about the design of pumps. This form of research is often encountered in the field of turbomachinery because of high computing power required for optimisation and high costs of design verification. The project consisted of two main parts: numerical optimisation to generate the best design and testing to validate the optimisation process. Research was conducted in cooperation with Osaka Institute of Technology in Japan, which provided the baseline geometry of the pump and facilities required to test the new design.

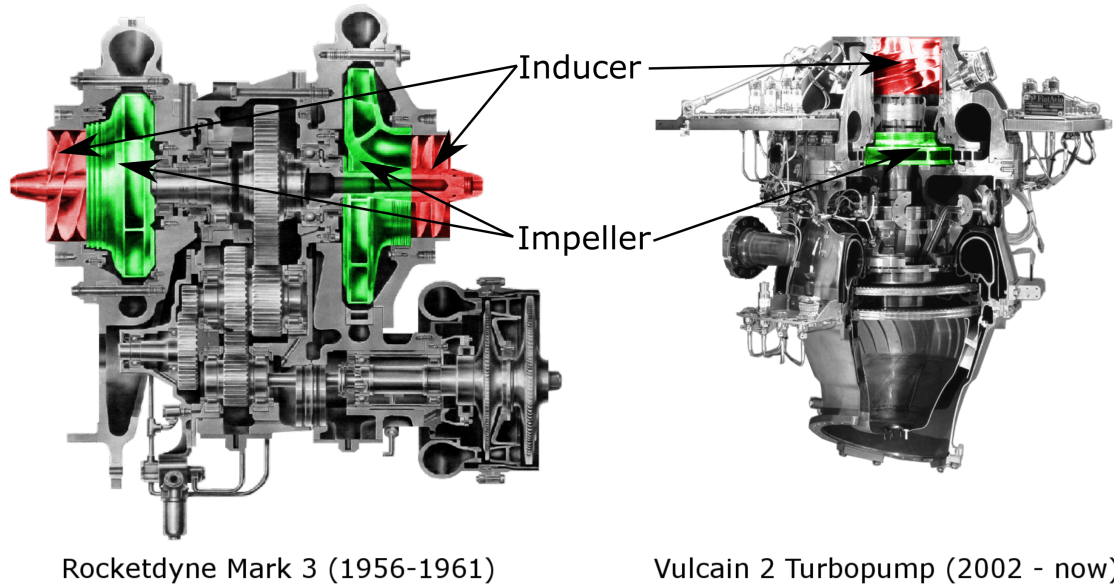


Figure 1.2: Cross-sections of two turbopumps: Rocketdyne Mark 3 and Vulcain 2 Turbopump with highlighted inducers and impellers [1, 6].

1.2. Research questions and goals of the thesis

As stated in the previous section this thesis focuses on finding the geometrical features of the inducer blade that improve the suction performance of the entire pump. Main research question of the thesis is:

How and why the suction performance of a pump is improved by optimising the inducer blades with a surrogate based optimisation method?

This main question can be also divided into smaller and more clear sub-questions:

1. How big improvement of suction performance can be achieved by optimising the shape of the blades?
2. What blade shape gives the improved suction performance?
3. Why the optimised blades improved the suction performance?
4. What design guidelines can be formulated regarding the shape of inducer blades for suction performance improvement?

Main thesis goal can be stated in the following way:

The main goal of the thesis is to identify the key geometrical features causing the improvement of the suction performance achieved by optimising the shape of the pump inducer blades, in order to propose better design guidelines for the future rocket engine turbopumps.

This main goal can be broken into smaller sub-goals. Fulfilling all of those goals is necessary for successful completion of this research project. Therefore those goals can be also treated as a "recipe" for a successful project and define the approach used during the project.

1. Familiarise with the baseline design and choose the best parametrisation method and operating conditions for the simulation.
2. Build a surrogate based optimisation framework that improves the cavitating performance.
3. Obtain an optimised candidate design and characterise the changes in geometry between the candidate and the baseline.
4. Validate the accuracy of the optimisation framework and numerical calculations by testing the cavitating performance of the candidate design.
5. Identify key changes in the flow field that resulted in the improvement of the cavitating performance.

1.3. Report structure

This report consist of the following 7 chapters:

1. Introduction
2. Turbopump performance parameters and optimisation problem description - introduces the most important concepts required to describe the influence of cavitation on pump performance and to define the optimisation problem
3. Baseline pump design - presents the design that was used as a starting point of the optimisation and a reference point for the performance improvement
4. Optimisation framework - shows how the tool made to solve the optimisation problem is structured and how it works
5. Optimisation results - shows the procedure of obtaining the best result and its outcomes
6. Performance improvement analysis - shows the comparison between the baseline and optimised designs and explains the reason for improvement of suction performance
7. Conclusions and recommendation - presents the main conclusions as answers to the research questions and recommendations for future work

2

Turbopump performance parameters and optimisation problem description

This chapter introduces basic information and concepts required to properly state the optimisation problem of this thesis and understand its solution. It focuses on the parameters used to describe turbopump performance and connections between them. The influence of cavitation on the pump is also investigated. Finally, terminology specific to optimisation problems is explained.

2.1. Notation

In a field of turbomachinery blade shape and flow field properties are usually given in a cylindrical coordinate system. Position of each point P is expressed with three coordinates (r, z, θ) defined in the following way:

- r is the distance from the Z axis, coincident with the axis of rotation, to the point P
- z is the distance from a chosen plane perpendicular to the Z axis to the point P
- θ is the angle between the reference direction on the chose plane and the line from the origin to the projection of P on the plane

Figure 2.1 shows the graphical interpretation of this coordinate system. Big letters Z, R and C denote the directions along which z , r and θ are increasing, respectively. These direction are called: axial (Z), radial (R) and circumferential (C).

Figure 2.2 shows a generalised blade in meridional view which is a 2D projection of a blade onto the Z-R plane while neglecting blade curvature in the circumferential direction. This general blade is attached to a rotating hub and extends until its tip. Leading and trailing edges are located at the inlet and outlet of the pump respectively. Their relative position defines the length of the blade. The radii of the leading edge tip, R_{T1} , and leading edge hub, R_{H1} , as well as the radii of the trailing edge tip, R_{T2} , and trailing edge hub, R_{H2} are the main parameters required to start the analysis of pump performance. Subscripts 1 and 2 are used to denote the properties at the inlet and outlet of the pump, respectively. In the meridional view a meridional direction can be defined, which is often used in turbomachinery analysis. Meridional direction is a direction that is tangent to a meridional curve. Meridional curve is a curve of constant spanwise location, which radius R_M defined as:

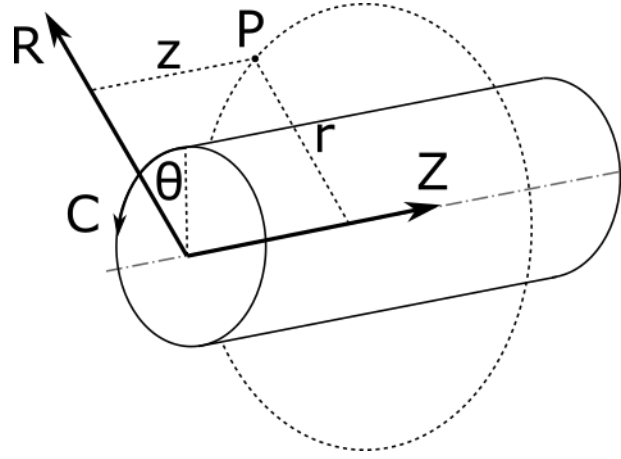


Figure 2.1: Cylindrical coordinate system used to define blade and flow field coordinates.

$$R_M(Z) = x (R_T(Z) - R_H(Z)) + R_H(Z) \quad (2.1)$$

x is a fixed span fraction and $R_T(Z)$ and $R_H(Z)$ are the functions defining the tip and hub radii along the axial direction. The meridional direction can be also defined in terms of how the radial and axial coordinates change along the meridional curve:

$$M = dR + dZ \quad (2.2)$$

Where M , dR and dZ are vectors in R-Z plane.

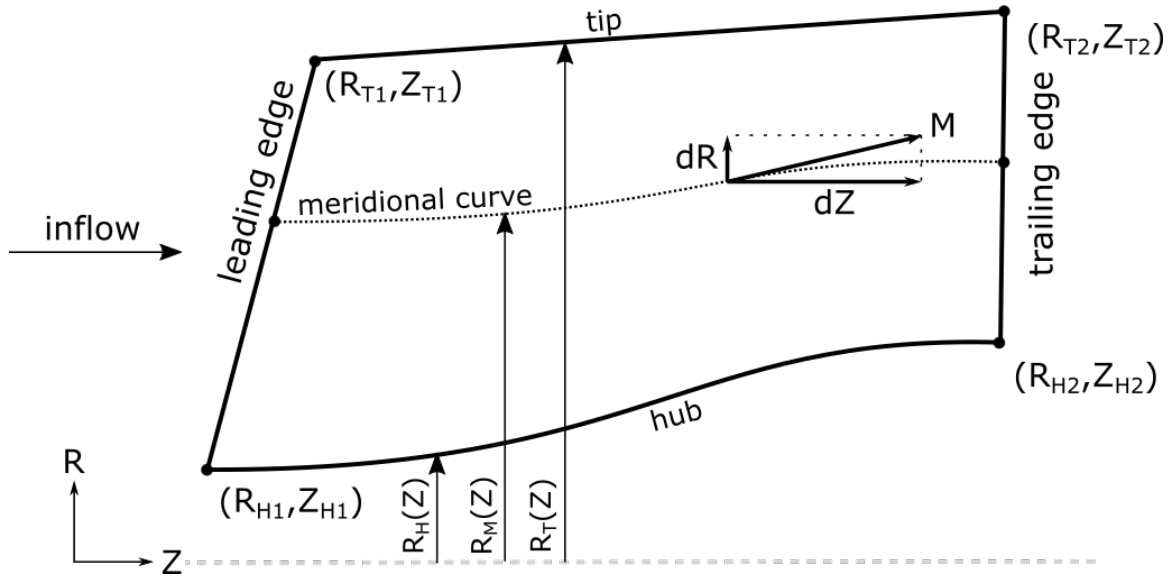


Figure 2.2: Generalised turbopump blade in meridional view.

2.2. Fundamental equations

Every pump is designed to achieve certain static pressure rise Δp_s while delivering certain volume flow Q with certain efficiency η . The pressure rise in the pump can be used to calculate another important parameter, called a head of a pump and usually denoted as H . The head is

defined as the height of the column of the pumped fluid which exerts the static pressure at the bottom of the column equal to the pressure rise in the pump. It is important to distinguish between the total head, H_t , (based on the increase of the total pressure Δp_t) and the static head of the pump, H_s , (based on the increase of static pressure Δp_s). Both heads may be easily calculated as shown in Equation 2.3.

$$H_{t/s} = \frac{\Delta p_{t/s}}{g\rho} \quad (2.3)$$

Where g is the Earth gravitational acceleration (9.81 m/s^2) and ρ is the density of the pumped fluid. Hydrodynamic efficiency is defined as the ratio of useful power P_u (energy transferred to the fluid in a unit of time) to the mechanical power of the impeller P . The useful power transferred to the fluid is obtained by multiplying the mass flow rate through the pump \dot{m} by the specific work of the pump, which is equal to the change of the total specific enthalpy of the fluid. The mechanical power of the impeller is equal to the rotational speed of the shaft ω multiplied by the torque of the shaft T .

$$\eta = \frac{P_u}{P} = \frac{\dot{m}\Delta h_t}{\omega T} = \frac{\rho Q \Delta h_t}{\omega T} \quad (2.4)$$

The change of the total specific enthalpy is equal to:

$$\Delta h_t = \frac{\Delta p_t}{\rho} = gH_t \quad (2.5)$$

What allows to express the hydrodynamic efficiency as:

$$\eta = \frac{Q \Delta p_t}{\omega T} = \frac{\rho g H_t Q}{\omega T} \quad (2.6)$$

More details about calculations of pump efficiency or the relationship between the specific work of the pump and the change of pressure in the fluid can be found in the book by Brennen [7] or Gulich [5]. Equation 2.6 shows that the useful power of the pump increases linearly both with the increase of the volume flow and the pressure rise in the pump.

During the design process of the pump it is crucial to be able to predict the pressure rise for a given geometry of the pump. The total pressure rise in the pump can be calculated from the *Euler's turbine equation*, which allows to calculate the momentum T_{th} acting on the blades. It is derived from the conservation of angular momentum.

$$T_{th} = \rho Q(r_{2m}c_{2u} - r_{1m}c_{1u}) \quad (2.7)$$

where r_{1m} and r_{2m} are the mean radii at the inlet and the outlet of impeller and c_{1u} and c_{2u} are the absolute circumferential velocities at the inlet and the outlet of the impeller respectively. Torque acting on the impeller is used to increase the circumferential velocity of the fluid. By multiplying both sides of this equation by the rotational velocity of the impeller the relationship between the theoretical power of the pump and the change of the circumferential velocity is obtained.

$$P_{th} = T_{th}\omega = \rho Q(u_{2m}c_{2u} - u_{1m}c_{1u}) \quad (2.8)$$

where u_{1m} and u_{2m} are the blade speeds at the mean inlet and outlet radius respectively. In the ideal, lossless case this power is equal to the useful power P_u shown in the previous section. By combining equations 2.4, 2.3 and 2.8 the relationship between the total pressure rise, geometry of the pump and the velocities of the fluid is obtained.

$$\Delta p_t = \rho \Delta h = \frac{P_{th}}{Q} = \rho(u_{2m}c_{2u} - u_{1m}c_{1u}) \quad (2.9)$$

The speed of the blades is determined by the geometry and the rotational speed of the impeller: $u_m = \omega r_m$. Both absolute velocities might be calculated from the velocity triangles, one defined at the inlet and one defined at the outlet of the impeller. The velocity triangle shows a relationship between the absolute and relative fluid velocities. The absolute velocity, denoted by c , is the velocity observed by the stationary observer, while the relative velocity, denoted by w , is observed by the observer on the rotating impeller.

The direction of inlet absolute velocity c_1 is determined by the flow conditions upstream. Usually it contains only a meridional component c_{1m} , but generally a circumferential component c_{1u} may be present. The relation between both components defines the absolute inlet angle α_1 . The relative velocity w_1 is the velocity that is effectively seen by the rotating impeller. It is calculated by subtracting the blade speed u_1 from the absolute velocity c_1 . The relative velocity defines the inlet blade angle β_{1B} . It is usually chosen to be slightly different than the actual inlet flow angle, so that the blade operates with certain incidence angle i . The triangle made by vectors c_1 , w_1 and u_1 is called an inlet velocity triangle. Its graphical representation is shown in Figure 2.3

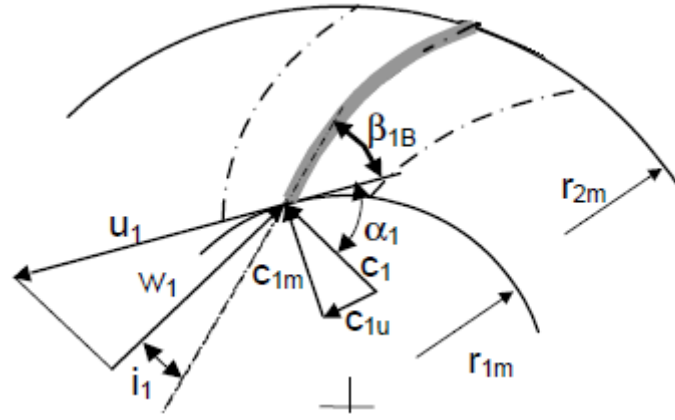


Figure 2.3: Inlet velocity triangle. [5]

At the outlet the situation is reversed - first the relative velocity w_2 is known and the absolute velocity c_2 must be determined. The flow outlet angle β_2 is defined by the blade outlet angle β_{2B} and the slip angle δ . In the ideal conditions the outlet flow angle would be equal to outlet blade angle. However, because there is a finite number of blades the guidance of the flow is not perfect the flow deviates from the path established by the blade. The absolute velocity c_2 is calculated by adding the circumferential blade speed at the outlet u_2 to the relative outlet velocity w_2 . Then the circumferential component c_{2u} may be calculated. This component might be used to calculate the ideal total pressure rise in the pump. The triangle made by vectors c_2 , w_2 and u_2 is called an outlet velocity triangle. Its graphical representation is shown in Figure 2.4.

2.3. Dimensional analysis and similarity laws

Using dimensional parameters like head is necessary when the pump must be chosen for a specific application. However, such parameters are only relevant to pumps with similar per-

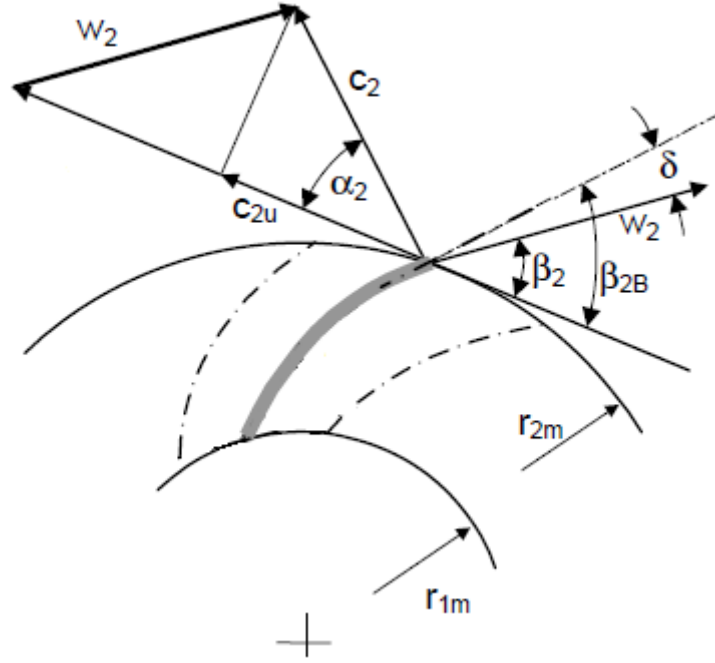


Figure 2.4: Outlet velocity triangle. [5]

formance and size and cannot be used to derive general conclusions about the quality of the design. For the same reasons they cannot be used to derive any universal design guidelines. Expressing the performance and operating conditions in a dimensionless form allows to generalise test results to other pump rotational speeds and sizes. The dimensionless coefficients used in this approach are formed by reducing a group of independent physical variables in a process called dimensional analysis. Its principal goal is to deduce a possible form of a relationship between a number of variables by studying their dimensions. Choice of the independent variables used in this process is arbitrary and the outcome of the analysis is different for different set of chosen parameters. However, not all formulations are equally useful so proper choice of the basic parameters is crucial to the success of this method. More details about dimensional analysis can be found in Sonin [8].

Dixon [9] provides an example of the dimensional analysis applied to a liquid pump. Following parameters are chosen as independent variables: volume flow Q , rotational speed ω , pumped liquid density ρ , pumped fluid viscosity μ and impeller size characterised by its radius R and ratios of other dimensions to this diameter $l_1/D, l_2/D, \dots$. The performance parameters showed in the previous section, efficiency η , power supplied P and energy transfer gH may be expressed a function of these variables:

$$\begin{aligned} gH_t &= f_1(Q, \omega, R, \rho, \mu, \frac{l_1}{D}, \frac{l_1}{D}, \dots) \\ \eta &= f_2(Q, \omega, R, \rho, \mu, \frac{l_1}{D}, \frac{l_1}{D}, \dots) \\ P &= f_3(Q, \omega, R, \rho, \mu, \frac{l_1}{D}, \frac{l_1}{D}, \dots) \end{aligned} \quad (2.10)$$

By using the three primary dimensions, mass, length and time the dimensionless groups can be formed. Selection of ρ , ω and D as common factors allows to make gH , η and P explicit. The functions presented in 2.11 can be transformed to the following forms:

$$\begin{aligned}
\frac{gH_t}{(\omega R)^2} &= f_4 \left(\frac{Q}{\omega R^3}, \frac{\rho \omega R^2}{\mu}, \frac{l_1}{D}, \frac{l_1}{D}, \dots \right) \\
\eta &= f_5 \left(\frac{Q}{\omega R^3}, \frac{\rho \omega R^2}{\mu}, \frac{l_1}{D}, \frac{l_1}{D}, \dots \right) \\
\frac{P}{\rho \omega^3 D^5} &= f_6 \left(\frac{Q}{\omega R^3}, \frac{\rho \omega R^2}{\mu}, \frac{l_1}{D}, \frac{l_1}{D}, \dots \right)
\end{aligned} \tag{2.11}$$

The term on the left-hand side of the first equation is called a head coefficient and denoted ψ . It can be calculated from both static and total head. The characteristic radius is assumed to be the tip radius at the outlet of the impeller. In this case the denominator represents the square of blade tip speed.

$$\psi_{t/s} = \frac{gH_{t/s}}{(\omega R_{t2})^2} = \frac{\Delta p_{t/s}}{u_{t2}^2} \tag{2.12}$$

The dimensionless group $\frac{Q}{\omega R^3}$ is a volumetric flow coefficient. In case of axial flow turbomachines like inducers, an alternative flow coefficient ϕ is often used:

$$\phi = \frac{c_m}{u_{t1}} \propto \frac{Q}{\omega R^3} \tag{2.13}$$

where c_m is the velocity component in the meridional direction and u_{t1} is the blade speed at the tip. Both values are taken at the inlet to the pump. It is important to notice that the angles of the inlet velocity triangle are the same for all pumps operating with the same flow coefficient. Equations 2.11 show that both ψ and η are dependent on a large number of other dimensionless groups of variables. If all of them had to be taken into account the derived relationships would have a limited practical use. However, the problem may be greatly simplified if only *similar* flow field are considered. In general, two flow fields are similar when the following conditions are fulfilled:

- Geometric similarity condition - all dimensions of a small-scale model are scaled to the same ratio with respect to the full-scale model
- Kinematic similarity condition - all velocities of a small-scale flow are scaled to the same ratio with respect to the full-scale flow
- Dynamic similarity condition - all forces acting on of a small-scale flow are scaled to the same ratio with respect to the forces acting on a full-scale flow

If two pumps are geometrically similar then ratios $\frac{l_1}{D}, \frac{l_2}{D}, \dots$ are the same for both machines and can be eliminated. Flow coefficient, defined as a ratio of two velocities, is a form of the kinematic similarity condition. Dynamic similarity is judged by comparing the values of several dimensionless numbers that are defined as a ratio of certain types of forces. The numbers often used in fluid mechanics are [10]:

- Reynolds number - ratio of inertia force to viscous force which dominate in the absence of a free surface and when compressibility of the fluid may be neglected (for example: flow in a pipe).

$$Re = \frac{L v \rho}{\mu}$$

- Froude number: ratio of inertia force to gravity force, used in free surface flows (for example: waves produced by motion of a boat)

$$Fr = \frac{v}{\sqrt{gL}}$$

- Mach number: ratio of inertia force to elastic force, used when compressibility of the fluid cannot be neglected (for example: flows at high velocity)

$$M = \frac{v}{a}$$

- Euler number: ratio of pressure force to inertia force, used when pressure difference in a flow is important (for example: when static pressure in the flow drops below the vapour pressure of a fluid)

$$Eu = \frac{\Delta p}{\rho v^2}$$

Where: L is the characteristic length, v is the flow velocity, μ is the dynamic viscosity of a fluid, g is gravitational acceleration, ρ is the density of a fluid, a is the speed of sound in a fluid at given conditions and Δp is the pressure difference. Each of these numbers is also a product of a dimensional analysis. For example, Reynolds number appears in a dimensionless form of a momentum equation. In fact, the $\frac{\rho \omega R^2}{\mu}$ term on the right hand side of Equations 2.11 is also a form of Reynolds number. Both Froude and Mach number are not important for a flow through a pump because the gravity and elastic forces are negligible with respect to inertia, pressure and viscous forces. Therefore the dynamic similarity condition is fulfilled when both pumps operate with the same Reynolds and Euler number. In practical applications the influence of Reynolds number on the performance of the pumps handling fluids with low kinematic viscosity (like water or liquid oxygen) may be ignored in a first approximation [5, 9]. Low kinematic viscosity means that the value of the Reynolds number remains correspondingly high even when fluid velocity or characteristic dimensions are changing. Similarly, the Euler number is important only when cavitation in the flow is possible. The similarity of a flow through the pump with respect to cavitation is described by a cavitation number σ , which is a form of the Euler number:

$$\sigma = \frac{p_1 - p_v}{0.5 \rho u_{t1}^2}$$

Where p_1 is the static pressure at the inlet to the pump, p_v is the vapour pressure of a fluid at a given temperature and u_{t1} is the blade tip speed also at the inlet. The values at the inlet are used because the static pressure is the lowest near the leading edge of a blade.

2.4. Pump characteristic

The pumps are usually designed to operate at one operating work defined by the specific pressure rise and the specific volume flow at that point. Sometimes the pump designed for one point has to operate at a different point - in the rocket engine it usually means that the thrust required from the engine increases or decreases, so the volume flow must increase or decrease correspondingly. It is important to say that the characteristic presented in this section are valid in the absence of cavitation.

Ideal characteristic

A simplified, ideal characteristic may be derived under the following assumptions: the pump is rotating with the constant speed, the blades are infinitely thin, the viscous losses can be neglected, the flow is incompressible, axisymmetric and steady in the rotating frame of reference. In that case the flow at any streamline will follow the Bernoulli equation for a rotating system [7].

$$\frac{2p_1}{\rho} + w_1^2 - r_1^2\omega^2 = \frac{2p_2}{\rho} + w_2^2 - r_2^2\omega^2 \quad (2.14)$$

This equation can be rewritten in terms of total pressure rise in the pump (using the total pressure definition and the relations from the velocity triangles).

$$\Delta p_t T = p_2 - p_1 + \frac{\rho}{2}(c_2^2 - c_1^2) = \rho(u_2 c_{2u} - u_1 c_{1u}) \quad (2.15)$$

After nondimensionalising, and assuming that no initial swirl is present, a performance characteristic in terms of head coefficient and outlet flow coefficient is achieved. As it can be seen the head coefficient is also a function of the blade angle. The example characteristics for different blade angles are shown in Figure 2.5.

$$\psi = 1 - \phi \cot \beta_{b2} \quad (2.16)$$

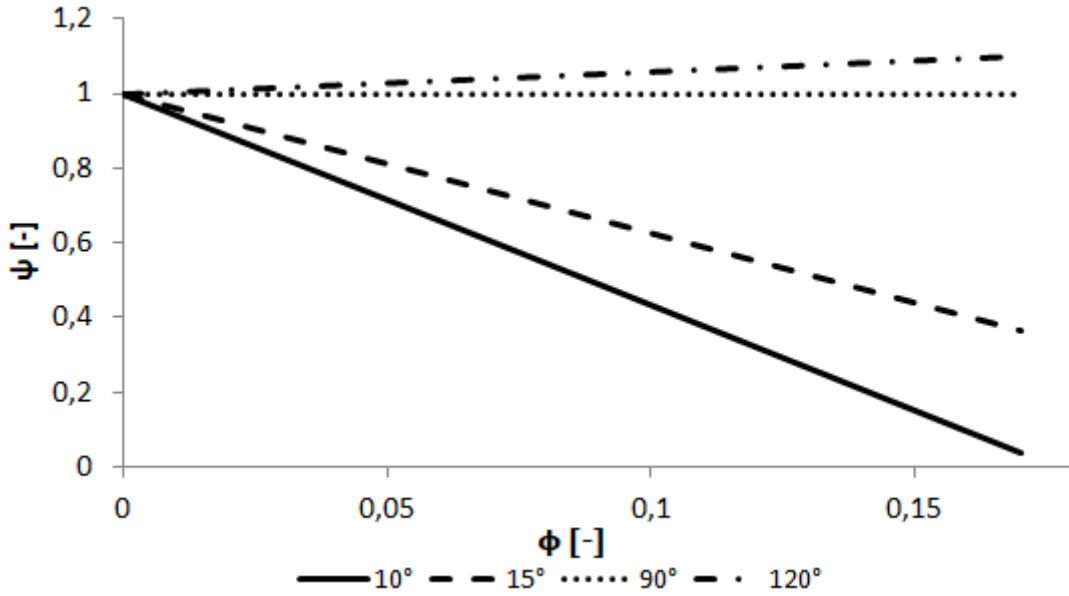


Figure 2.5: Ideal pump characteristic expressed in nondimensional parameters for several outlet angles.

The blades with the outlet angle between 0° and 90° are called backward facing blades. The head coefficient is decreasing with increasing flow because the higher meridional velocity reduces the centrifugal component of the outlet absolute velocity. For the radial blades there is no change in the head coefficient because higher meridional velocity does not effect the circumferential component of the absolute outlet velocity. In case of the forward facing blades the situation is reversed as in the case of backwards facing blades. The comparison of outlet velocity triangles for blades with different angles is shown in Figure 2.6.

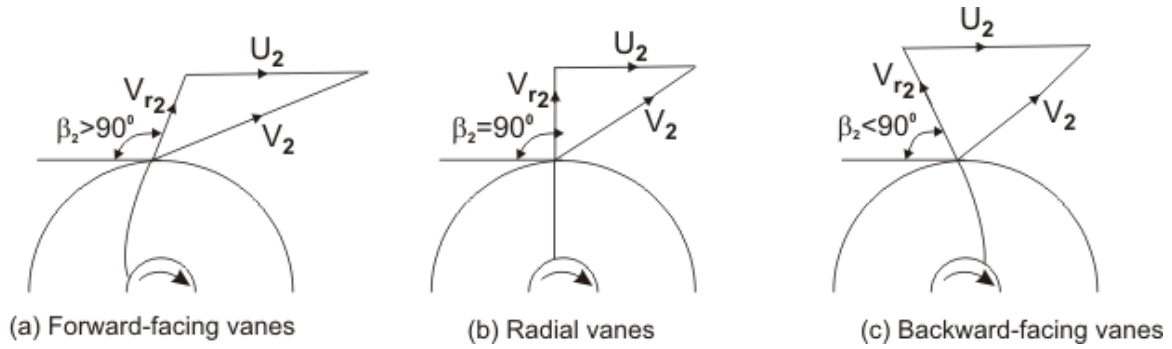


Figure 2.6: Velocity triangles for different blade outlet angles. [11]

Real characteristic

The real pump characteristic of course deviates from the ideal characteristic. The comparison between those two characteristics are shown in Figure 2.7. In the same figure the main sources of losses are highlighted. Figure 2.8 shows each of those loss components separately.

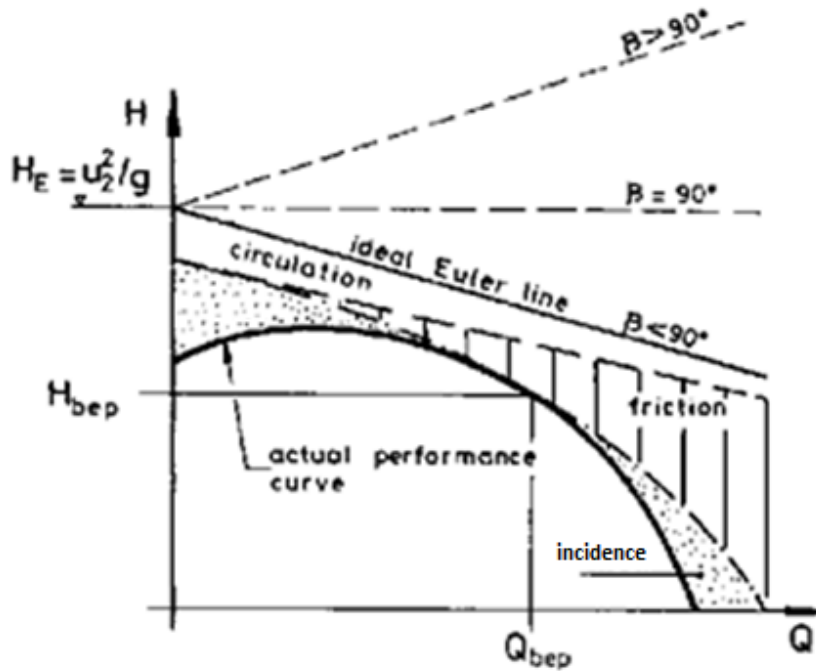


Figure 2.7: Real pump characteristic. [12]

The so-called circulation losses are related to the slip angle present in the outlet velocity triangle. The higher the slip angle the lower the circumferential velocity at the outlet and the lower the pressure rise. The second kind of loss is the friction loss generated by the fluid's viscosity near the solid surfaces of the pump. This loss increases with the square of the flow velocity in the pump and therefore also with the square of the volume flow through the pump. The last kind of loss is the incidence loss which is generated when the flow inlet angle is different than the blade inlet angle. It is zero when those two angles are equal (only at the design volume flow) and increasing at higher and lower flows. The losses are generated due to a flow separation occurring at high incidence angles.

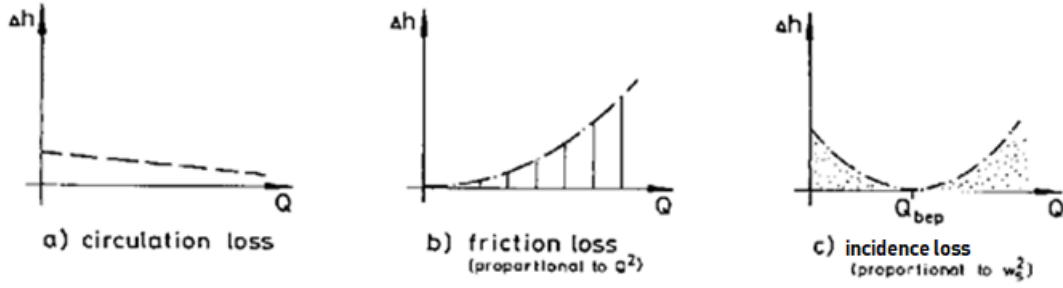


Figure 2.8: Basic sources of losses in the centrifugal pump. [12]

2.5. Cavitation and suction performance

Cavitation is a partial evaporation of liquid in a flow system [5]. It occurs when the local static pressure of the flow falls below the vapour pressure of the fluid. In order to characterise the risk or magnitude of cavitation in a given pump several quantities can be used. In the industry practice the Net Positive Suction Pressure is often used. It is defined as the difference between the inlet static pressure and the fluid vapour pressure. As in the case of the pressure rise, this pressure can be expressed as a height of the fluid column - Net Positive Suction Head.

$$\begin{aligned} NPSP &= p_{t1} - p_v \\ NPSH &= \frac{p_{t1} - p_v}{\rho g} \end{aligned} \quad (2.17)$$

Dimensional quantities NPSP and NPSH refer to one specific case only and do not allow to make a reliable comparisons between different designs. As it was already mentioned, cavitation number σ is used to judge the similarity of flows with cavitation. It relates the NPSP to the dynamic pressure based on blade tip speed at the inlet to the impeller:

$$\sigma = \frac{p_1 - p_v}{0.5 \rho u^2} \quad (2.18)$$

Another dimensionless number that can be used is the suction specific speed. The definition of truly dimensionless suction specific speed requires using the Net Positive Suction Energy instead of NPSH or NPSP.

$$\begin{aligned} NPSE &= \frac{p_{t1} - p_v}{\rho} \\ S_s &= \frac{\omega Q^{0.5}}{NPSE^{0.75}} \end{aligned} \quad (2.19)$$

Term "Suction performance" refers generally to the ability of the pump to deliver required head while the cavitation develops at the inlet of the pump. If the static pressure inlet is high enough the pumps works in the "wet" conditions, that is without cavitation. This situation corresponds to a high cavitation number. As the inlet pressure is lowered the cavitation starts to occur. This moment is called an inception of cavitation and at this stage the cavitation does not effect the performance of the pump. The cavitation number at which the cavitation starts is called the cavitation inception number.

At this point the bubbles will usually show up in the region of reduced pressure in the tip vortex generated at the leading edge. As the inlet pressure further decrease (lower cavitation number) so-called bubble cavitation develops at the suction side of the impeller. The work transfer is slightly influenced and the head coefficient is slightly lower than the baseline wet

value. For many pumps the smallest cavitation number at which a certain drop of head occurs is given. Usually it relates to a 3 or 5 % drop of the head coefficient and is denoted as σ_3 or σ_5 . It means that at all lower cavitation numbers the drop will be bigger. The definition of those numbers is important for this project as the optimisation process will be focused on the minimising the value of this cavitation number.

Further decreasing the inlet pressure leads to faster drop of the head coefficient. Bubbles are so large that they join into a one big bubble attached to the blade. Those bubbles occupy most of the passage and the work transfer is greatly influenced. At some point the cavitation surge occurs and the head coefficient suddenly reaches 0. It is worth saying that measuring the cavitating characteristic at very low cavitation numbers is very inaccurate because the developed cavitation induces many instabilities that continuously change the flow properties inside the pump. A typical cavitating characteristic is shown in Figure 2.9.

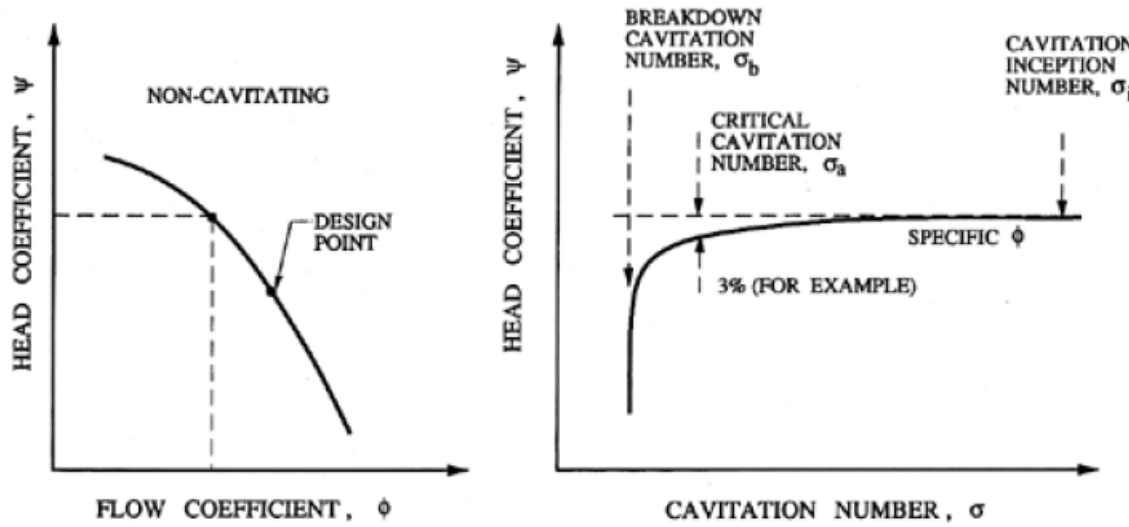


Figure 2.9: Cavitating characteristic at a fixed flow coefficient. [7]

The cavitating characteristic exactly shows why the cavitation is limiting the increase of the rotational speed of the rocket engine turbopumps. The definition of the cavitation number says that high values of that number can be achieved by increasing the inlet static pressure, decreasing the vapour pressure or decrease the inlet tip speed of the impeller. In rocket engines the inlet static pressure is defined by position of the pump with respect to the tank and the pressure inside the tank. Those two factors are usually fixed by the vehicle design. The properties of the pumped fluid (density, vapour pressure) also are fixed. Therefore the only parameter that can be used to achieve certain cavitation number is the blade tip speed. From the previous sections it is known that the rotational speed of the pump should be as high as possible to reduce the mass and size of the pump. At the same time the cavitation number must be high enough to allow efficient energy transfer to the fluid. In that way a constraint is set on the maximal rotational speed possible to achieve in the pump. By reducing the minimal required cavitation number the maximal rotational speed of the pump may be greater.

The cavitating characteristic in Figure 2.9 is given for one specific flow coefficient. In Figure 2.10 three different cavitating characteristics for three different flow coefficients can be seen. The steepness of the characteristic is higher in the case of the lower flow coefficient - the breakdown occurs less suddenly. This behaviour can be explained by looking at the definition of the flow coefficient, which is established by the inlet velocity triangle. At low flows (and

correspondingly low flow coefficients) the incidence angle is high. The incidence angle may be compared to an angle of attack of a wing. At high angles of attack the low pressure region is also big. In case of an impeller that leads to a bigger region influenced by cavitation and faster breakdown of the head.

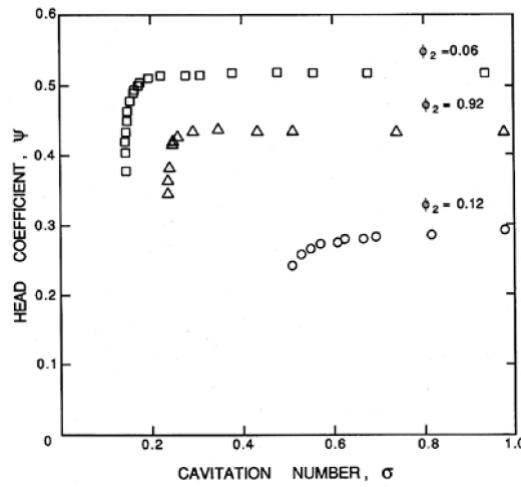


Figure 2.10: Cavitating characteristics at different flow coefficients. [7]

To better imagine the cavitating conditions in the pump, the different types of cavitation possible in an impeller are shown in Figure 2.11. The nuclei highlighted in the inflow are the tiny vapour bubble in the flow that initiate the grow of the cavitation bubbles. The vapour bubbles can exist in a flow with the pressure higher than the vapour pressure because they are adsorbed on non-wetting particles (like dirt or rust particles) [5]. The last cavitation type present in the picture is the backflow cavitation that refers to the all the bubbles and vortices forming in front of the impeller. This situation occurs when the pump is operating at part load and, as a result, low flow and high head coefficients. The high pressure within the impeller may cause a backflow through the tip clearance of the blade and take the vapour bubbles upstream of the impeller.

Apart from the loss of performance cavitation also has other negative effects. The vapour bubbles created in the region of low pressure travel downstream to the regions of the higher pressure where they collapse. This process generates a lot of noise and may damage the pump if the bubbles collapse near the blades (so called cavitation erosion). The cavitation erosion is a relatively slow process and its mitigation is important for pumps designed to operate thousands of hours during their lifetime. This is not the case for rocket engine turbopumps that operate only up to few minutes per launch. However, this might change in the future with a new generation of reusable launchers that extend the cumulated operating time required from an engine. Cavitation also induces different kinds of instabilities that influence the performance, reliability and stability of the pump. Cavitation induced instabilities were the likely cause of a hydrogen turbopump failure during the launch of a Japanese HII rocket in 1999 [13]. Both cavitation erosion and cavitation instabilities are the subject of extensive research but they are outside of the scope of this project. More information about cavitation erosion can be found in the book by Gulich [5] and the cavitation induced instabilities are extensively discussed in the summary of research already done on cavitation instabilities edited by d'Agostino [13].

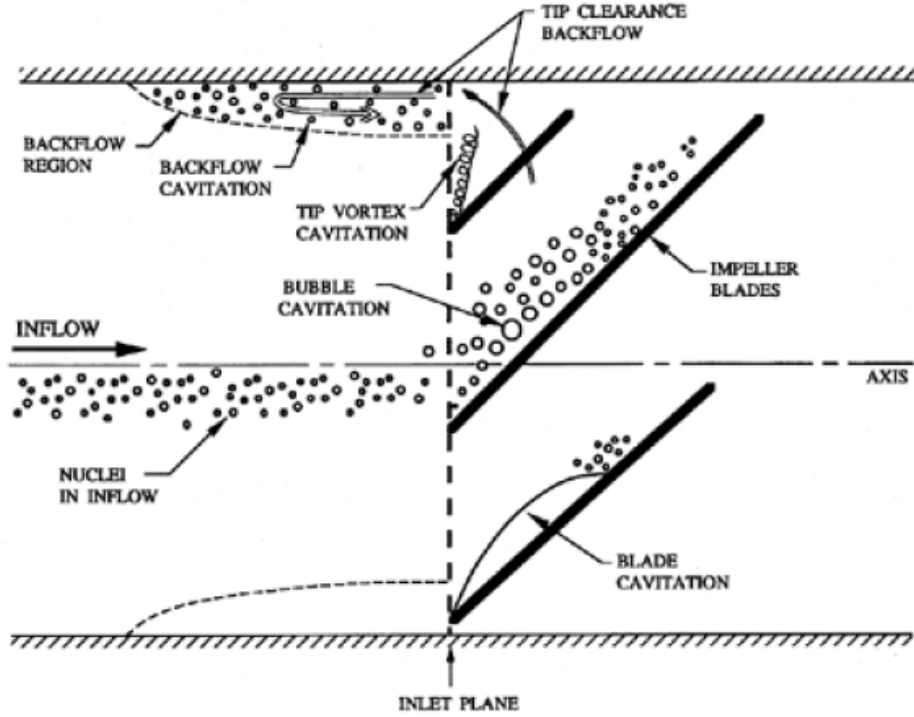


Figure 2.11: Different possible types of cavitation in an open axial impeller. [7]

2.6. Optimisation problem statement

In simple words optimisation is the process of obtaining the best result under given circumstances. Usually this means minimising the effort required to achieve certain results or maximise the benefits from a given effort. This definition, although correct, is not strict enough for the scientific purposes and must be replaced with a more specific one. Since the effort required or the benefit desired can be expressed as a function of certain decision variables, optimisation can be defined as the process of finding the conditions corresponding to the maximum or minimum of this function. Each optimisation process starts with a correct statement of the problem. A generic optimisation problem can be presented in a following way, adopted from the "Engineering Optimization: Theory and Practice" [14]:

$$\text{Find } \mathbf{X} = \begin{bmatrix} x_1 \\ x_2 \\ \vdots \\ x_n \end{bmatrix} \text{ which minimises } f(\mathbf{X}) \quad (2.20)$$

subject to the constraints

$$\begin{aligned} g_i(\mathbf{X}) &\leq 0, \quad i = 1, 2, \dots, m \\ h_j(\mathbf{X}) &= 0, \quad j = 1, 2, \dots, p \end{aligned} \quad (2.21)$$

\mathbf{X} is an n -dimensional vector called the design vector, $f(\mathbf{X})$ is the objective function, and $g_i(\mathbf{X})$ and $h_j(\mathbf{X})$ are known as inequality and equality constraints. Such problem is called a constrained optimisation problem. In this chapter the solution of the optimisation problem will be denoted \mathbf{x}^* .

Design vector

Each engineering system or component is described by a finite number of quantities. Some of them are usually fixed during the entire process and can be called preassigned parameters. The rest of the quantities are the variables in the optimisation process and are called design variables. Each design vector \mathbf{X} represents collectively all of the design variables and defines one design point in an n -dimensional design space. The design space contains every possible combination of the design variables. Some of those design points may be *impossible*, that is the design represented by this point makes no sense (for example imagine a design point for an impeller with a number of blades equal to -6). Therefore it is important to correctly define the design space, so that it only contains *possible* designs.

Design constraints

In most of the designs the design variables and their values cannot be chosen arbitrarily. The acceptable design points are defined by so called design constraints that may be divided into two groups. The *behaviour or functional constraints* represents the requirements with respect to the performance of the component or system (for example: the head of the pump must be higher than ...). The *geometrical constraints* represent the physical limitations of the design related to its manufacturability, transportability or integration (for example: the thickness of the blade must be higher than ... or the impeller must fit into the casing).

The constraints may be also divided into equality and inequality constraints, as it was shown above, in the problem statement. Most of the constraints in the engineering problems are inequality constraints. This is due to the fact that every engineering model approximates reality (especially when a numerical or iterative method is used to solve the problem) and the exact constraint is not likely to be fulfilled.

Objective function

Objective function is maximised/minimised function and the criterion that allows for comparing different designs against each other. In most of the cases the objective function is quite simple to define: the mass of the structure shall be minimal, the efficiency shall be maximal etc. However, this conceptual simplicity usually does not translate into simple mathematical formulation of the objective function. In the simplest case the objective function is defined by an explicit analytical function (for example, $f(x) = x^2$). Unfortunately, such function usually may be obtained only for a very simple or very simplified cases. The growing popularity of the numerical models further complicated the relation between the design variables and the value of the objective function. The problem may also have multiple objective function that often promote conflicting designs. For example, the frame of an aircraft should be strong and light, but the strongest design probably will not be the lightest. As a result of such multi-objective optimisation multiple designs will be obtained and additional trade off is required to choose the best design.

Baseline pump design

3.1. Pump overview

The optimisation starts from a baseline design of a pump which is made from two main components: three-bladed inducer and six-bladed impeller. The impeller is an industrial pump for general purpose designed by a Japanese company Teral. Together with a dedicated electric motor and casing, this pump was given by Teral to the Fluid Machinery Lab at Osaka Institute of Technology in Japan. There it became a standard platform for Master students conducting research related to centrifugal pumps. Table 3.1 presents basic specifications of the original Teral design at its design point.

Model	SJ65x50L63.7
Pumped fluid	Water
Volume flow	8.33 l/min
Static pressure rise	2.6 bar
Static head	26.1 m
Rotational speed	3600 rpm
Rated power	3.7 kW
Flow coefficient	0.204
Static head coefficient	0.381

Table 3.1: Design operating conditions of the baseline pump.

The original impeller had six full blades and did not have an inducer. In 2015 the length of every second blade was reduced in order to study the influence of created in this way splitter blades on suction performance [15]. A cross-section of the impeller showing main and splitter blades is given in Figure 3.1. During the same study the gain of performance from the introduction of splitter blades was compared with the performance gain achieved by adding an inducer. The inducer was designed according to the design guidelines of Japan Society of Mechanical Engineers [16]. The study showed that splitter blades can improve suction performance but adding inducer still proved to be a better method. It was also noticed that combining inducer with the impeller with splitter blades resulted in a pump with the best performance. In 2017 a cooperation between TU Delft and OIT was started. Two students, F. Torre from TU Delft and S. Konno from OIT, investigated the reason why splitter blades help maintain higher head at low cavitation numbers and what is their optimal shape [17]. They

found out that a splitter blade moved closer to the pressure side of the main blade suppresses a cavitation induced flow separation. Unfortunately, a 5% improvement of suction performance was achieved at an expense of 4% efficiency decrease in the wet conditions, what is considered a big drop. At the same time the study confirmed that a CFD-based optimisation is feasible within the constraints of a Master thesis project. Therefore it was concluded that the inducer should be optimised in the next part of the project. As it was mentioned in the introduction, it was hoped to gain a better understanding of the relationship between the shape of the blade and its suction performance. In this project the 2015 impeller with splitter blades was used, because its efficiency was not decreased with respect to the baseline Teral design. A side view of the pump geometry is shown in Figure 3.2. The inducer is moved away from the impeller so that it can be viewed through a transparent pipe during cavitation tests.



Figure 3.1: Main and splitter blades of the baseline impeller.

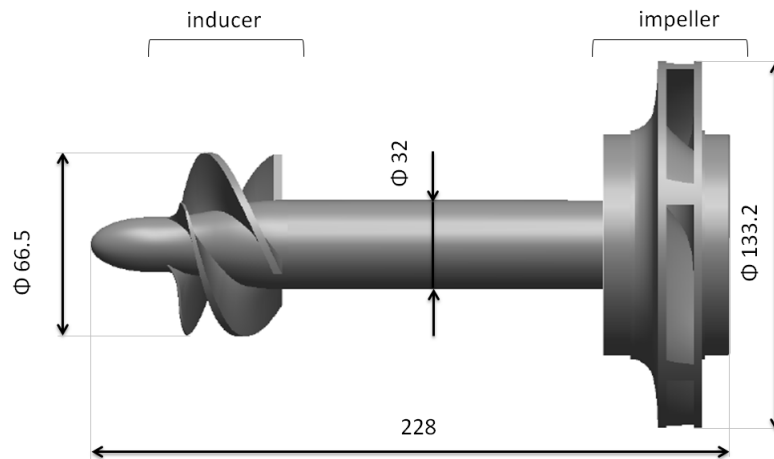


Figure 3.2: Side view of the baseline geometry.

In order to fully characterise design of the inducer (or design of any blade in turbomachinery) three main properties must be given: meridional profile, blade angle distribution and blade thickness distribution.

3.2. Meridional profile

Meridional profile shows the projection of the flow channel onto the plane passing through the axis of symmetry of the inducer. It also shows what is the contour the blade from side view. The meridional profile of the baseline inducer is shown in Figure 3.3 and of the baseline impeller in Figure 3.4. In this case the tip of the inducer has constant a constant radius at the tip and increasing radius at the hub. The radius of the tip is matched with radius of impeller inlet and is 0.5 mm smaller than the radius of the casing. This tip gap creates a margin for inducer movement during operation (for example due to vibrations) or manufacturing tolerance. Tapered hub is beneficial for at least two reasons. First of all, it minimises the velocity at the inlet due to larger cross-section area what reduces cavitation. Secondly, the pressure rise through the inducer is increased as the centrifugal velocity component is added. The meridional profile of the impeller shows that the inflow is axial while the outflow is purely radial. It also reveals where the splitter blade starts. Its leading edge is placed at the 45% of the main blade length.

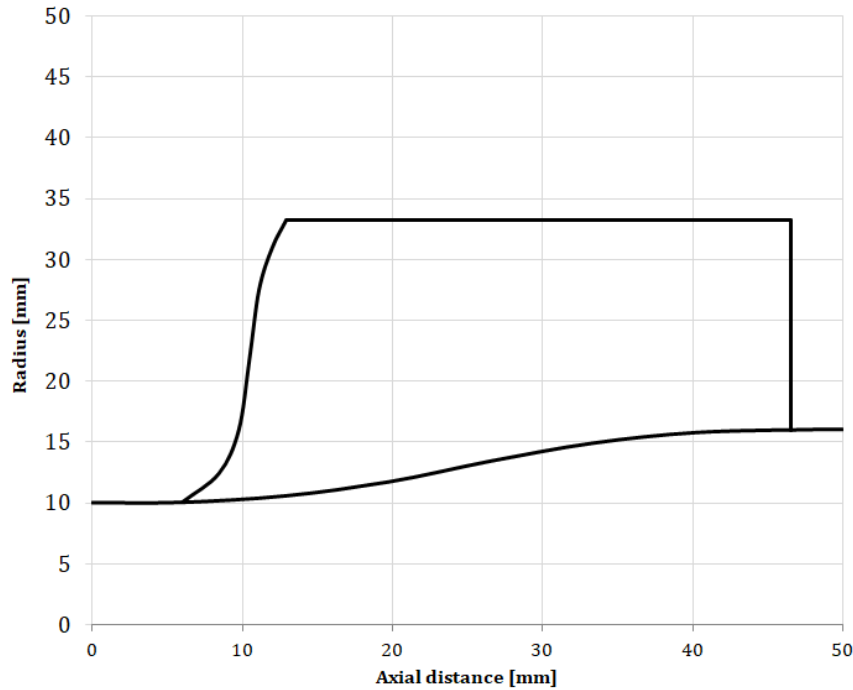


Figure 3.3: Meridional profile of the baseline inducer.

3.3. Blade angle distribution

Blade angle distribution is crucial for blade design. It has a large influence on every pump property, including the head as shows the ideal characteristic presented in Chapter 2. There are two angles that may be used to define blade shape: one denoted θ_B and the other denoted β_B . The former is the same angle used to define the cylindrical coordinate system presented at the beginning of Chapter 1. In that case position of each point on the blade is defined as $\theta_B = f(Z, R)$. The latter is defined as the angle between the direction defined by the blade at a given point and the axial direction, as shown in Figure 3.5. β_B angle provides more insight during flow analysis as it directly shows how the flow is turned by the blade, while θ_B

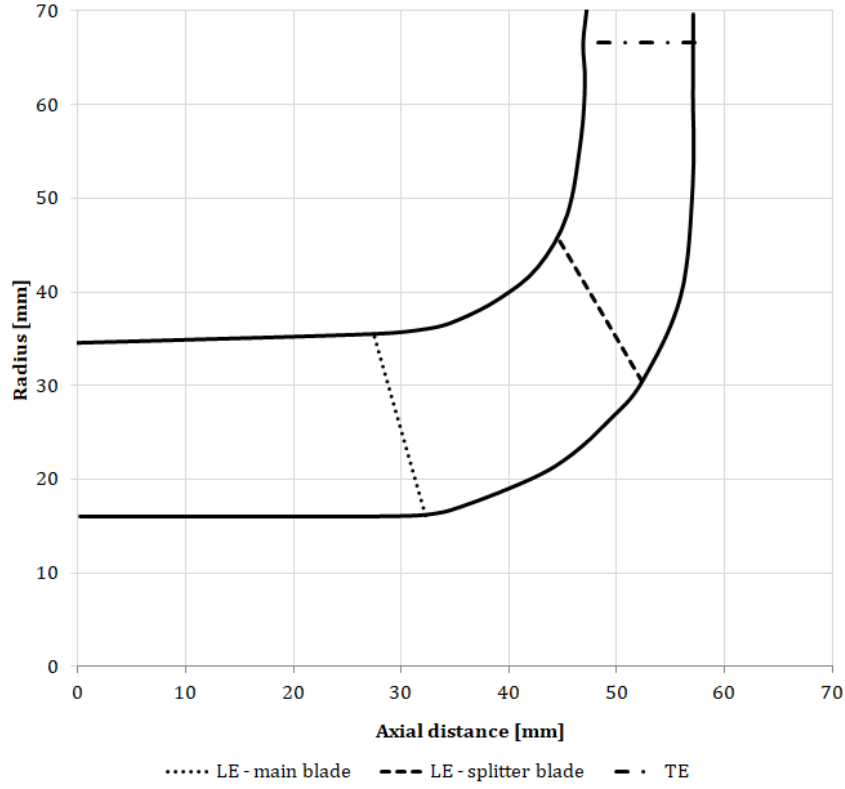


Figure 3.4: Meridional profile of the baseline impeller.

angle is more useful for accurate control of the blade shape. Both β_B and θ_B angles may be calculated if the distribution of the other angle is given. To derive the relationship between them, let's consider two points on the blade with the same spanwise position but at different axial coordinates, as shown in Figure 3.6. In this case we can define following quantities:

$$\begin{aligned}\Delta Z &= Z_2 - Z_1 \\ \Delta R &= R_2 - R_1 \\ \Delta \theta &= \theta_{b2} - \theta_{b1}\end{aligned}\tag{3.1}$$

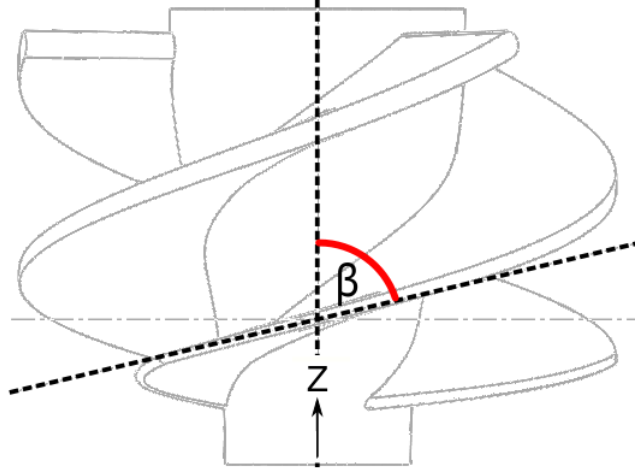
As ΔZ approaches 0, ΔR and $\Delta \theta$ also approach 0. These quantities become infinitesimal and are denoted δZ , δR and $\delta \theta$. Figure 3.7 shows how these small changes in coordinates between two points are used to construct a triangle containing β_B angle. It is a right triangle which sides have the following lengths:

$$\begin{aligned}a &= \sqrt{\delta Z^2 + \delta R^2} \\ b &= (R + \delta R)\delta \theta\end{aligned}\tag{3.2}$$

Since $\delta R \delta \theta \approx 0$ we can write that $b = R \delta \theta$ and express β_B as a function of $(\delta Z, R, \delta \theta)$:

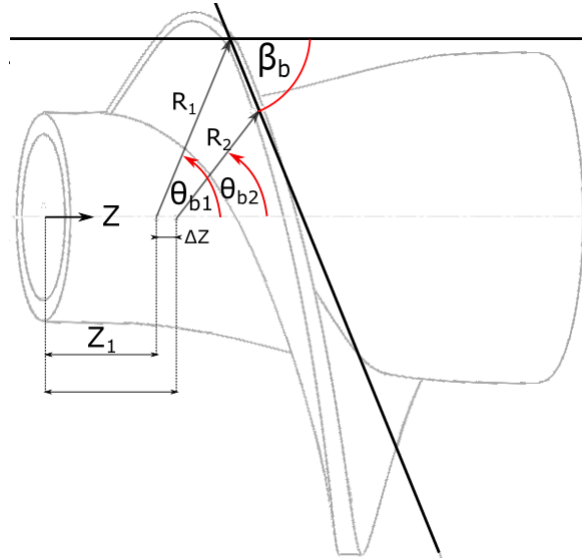
$$\beta_B = \text{atan}\left(\frac{b}{a}\right) = \text{atan}\left(\frac{R \delta \theta}{\sqrt{\delta Z^2 + \delta R^2}}\right)\tag{3.3}$$

Equation 3.4 defines the relationship between both angle and can be transformed if θ_B needs to be calculated from β_B angle distribution:

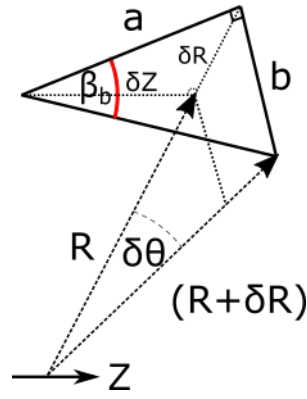
Figure 3.5: Definition of β blade angle.

$$\begin{aligned}\delta\theta &= \tan(\beta) \frac{\sqrt{\delta Z^2 + \delta R^2}}{R} \\ \theta_B &= \int_0^S \delta\theta ds\end{aligned}\tag{3.4}$$

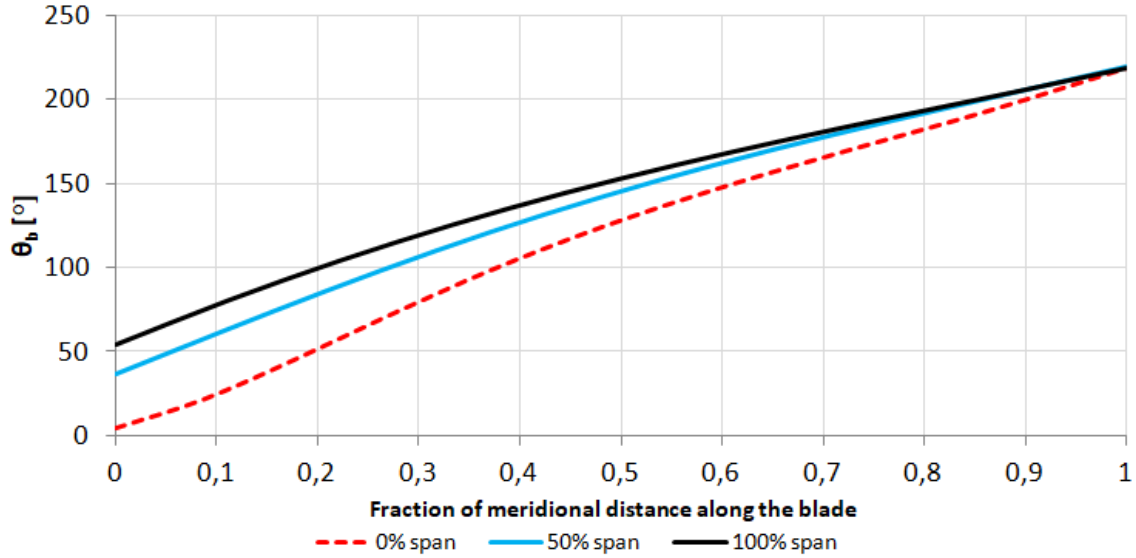
Where S is a fractional distance along the blade: $S \in [0, 1]$.

Figure 3.6: θ_B and β_B angles used to define blade shape.

Of course the angle changes not only along the blade, but also at different spanwise locations. Inducer blade angle distributions are shown in Figures 3.8 and 3.9 and are given for hub, tip and mid-span of the blade. It can be seen that θ_B angle at the beginning of the blade is increasing with increasing span. This means that the leading edge is not extending radially from the hub but is inclined by some angle. On the other hand the trailing edge is radial because θ_B angle at the end of the blade is the same for all spanwise layers. Blade angle distributions of the impeller blade are shown in Figure 3.10. The impeller design remained the same during the entire project and θ_B was not used and therefore it is not presented. Impeller blade is less complicated and therefore only hub and shroud angle distributions are shown. The outlet angle

Figure 3.7: Relationship between θ_B and β_B angles.

of the impeller, together with the outer diameter and width of the flow passage, determines the head of the entire pump.

Figure 3.8: θ_B blade angle distribution of the baseline inducer.

3.4. Blade thickness distribution

Thickness of a blade is mostly determined by the required strength of the blade. From the hydrodynamic point of view the blade should be as thin as possible. In this case the thickness of both inducer and impeller blade is constant along the span of the blade, but changes along the meridional direction. The thickness distribution of the inducer blade is shown in Figure 3.11 and of the impeller blade in Figure 3.12. Reduced blade thickness at inducer leading edge allows to increase suction performance by decreasing inlet flow velocity. Thickness of impeller blade does not change as much because its driven by the strength requirements.

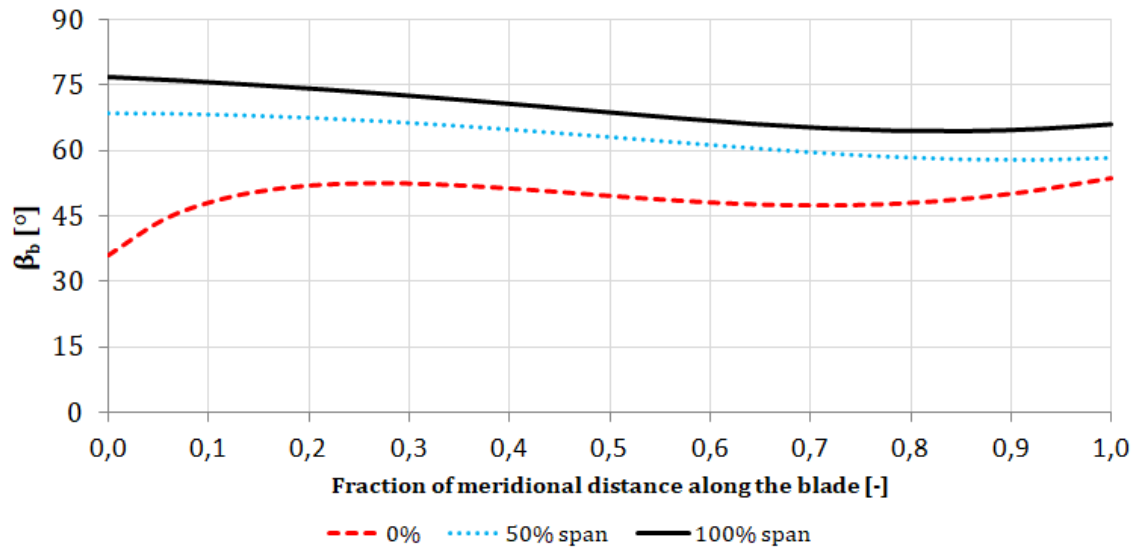


Figure 3.9: β_B blade angle distribution of the baseline inducer.

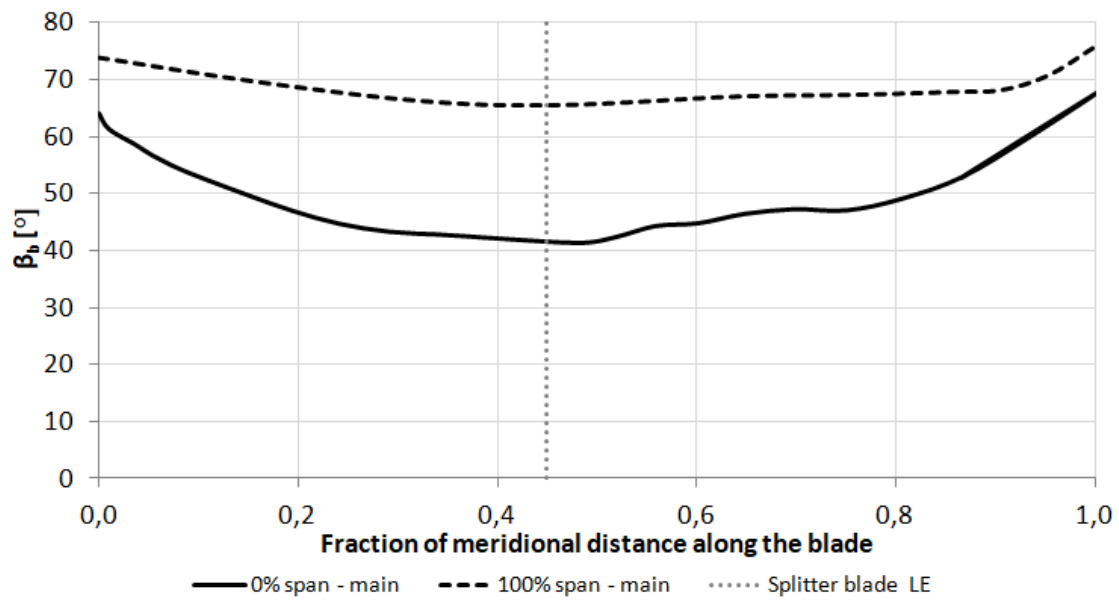


Figure 3.10: Blade angle distribution of the impeller.

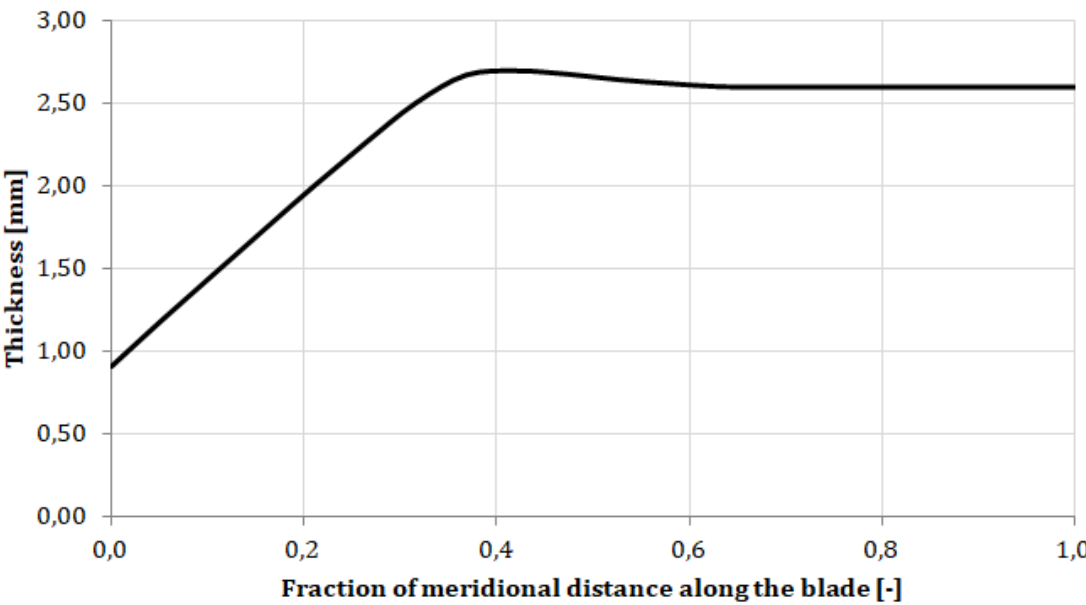


Figure 3.11: Blade thickness distribution of the baseline inducer design.



Figure 3.12: Blade thickness distribution of the impeller.

4

Optimisation framework

4.1. Framework overview

An optimisation framework is a tool created during this project to optimise the suction performance of the inducer parametrised with four parameters presented in the previous chapter. It is established in Ansys Workbench 17.1 environment and makes use of the built-in optimisation toolbox. The framework is made of several smaller blocks that exchange information between each other. The schematic of the framework is shown in Figure 4.1. In this Chapter the composition and functions of each block is explained.

4.2. Optimisation strategy

The main goal of the thesis is to improve suction performance of a pump by optimising the shape of an inducer. Improving the suction performance means that the pump can maintain desired head at lower cavitation numbers. This can be represented as a shift of the cavitating characteristic to the left, as shown in Figure 4.2. Unfortunately, this relatively simple concept does not give a clear idea about its implementation. In literature several ways of approaching the problem can be found. Some of them focus on minimising certain flow properties like the vapour volume inside the flow channel or pressure drop at the leading edge of the blade [18, 19]. Although those parameters greatly influence the suction performance of a pump, such criteria do not guarantee the best possible result, as the distribution of vapour volume and static pressure are equally important. Other approach may be to directly optimise the head of the pump while cavitation occurs. In that case a direct minimisation of a critical cavitation number provides the most robust approach, as it ensures that the range will be extended. Unfortunately, prediction of a critical cavitation number for a new design is computationally expensive, as it requires a transient two-phase simulation or at least several steady state simulations [20, 21]. The time required to make those simulations makes this type of optimisation infeasible with the computing power available during this MSc thesis.

A reduction of computing cost can be achieved by reducing the number of cavitation simulations needed per design. Such approach was used in a project aimed at optimisation of splitter blades of an impeller [22]. In this method a head coefficient of an entire pump at a critical cavitation number is maximised, so only one two-phase simulation per design is required during an optimisation process. Still, the main goal of the optimisation is achieved, as a pump with a higher head coefficient at certain cavitation number should have a larger operating range.

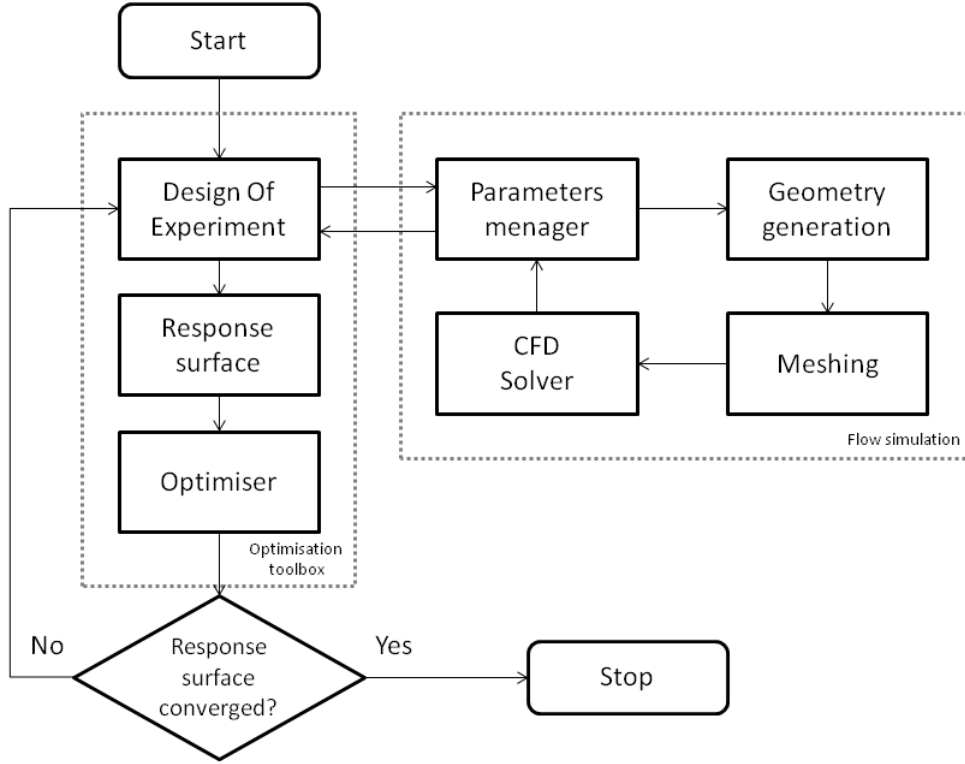


Figure 4.1: Optimisation framework overview.

This approach was adopted in the presented framework. Suction performance of each created design was evaluated at only one cavitation number that is the critical cavitation number of the baseline pump, denoted as σ_5 . In order to ensure that increase of suction performance will not be achieved at the expense of wet performance, constraints are imposed on the head coefficient and efficiency in the wet conditions. They can be expressed in the following way:

$$\begin{aligned} 0.99 \psi_{base} < \psi_{opt} < 1.05 \psi_{base} \\ \eta_{opt} &\geq \eta_{base} \end{aligned} \quad (4.1)$$

where ψ_{base} and η_{base} are the baseline values of head coefficient and efficiency in the design conditions, while ψ_{opt} and η_{opt} refer to the optimised design. These constraints mean that the head coefficient has to stay within the specified threshold and the efficiency shall not decrease. Now the formal statement of the optimisation problem can be written:

$$\text{Find } \mathbf{X} = \begin{bmatrix} x_1 \\ x_2 \\ \vdots \\ x_n \end{bmatrix} \text{ which maximises } \psi(\sigma_5, \mathbf{X}) \quad (4.2)$$

subject to the constraints:

$$\begin{aligned} 0.99 \psi_{base} - \psi_{opt}(\sigma_w, \mathbf{X}) &\leq 0, \\ \psi_{opt}(\sigma_w, \mathbf{X}) - 1.05 \psi_{base} &\leq 0, \\ \eta_{base} - \eta_{opt}(\sigma_w, \mathbf{X}) &\leq 0 \end{aligned} \quad (4.3)$$

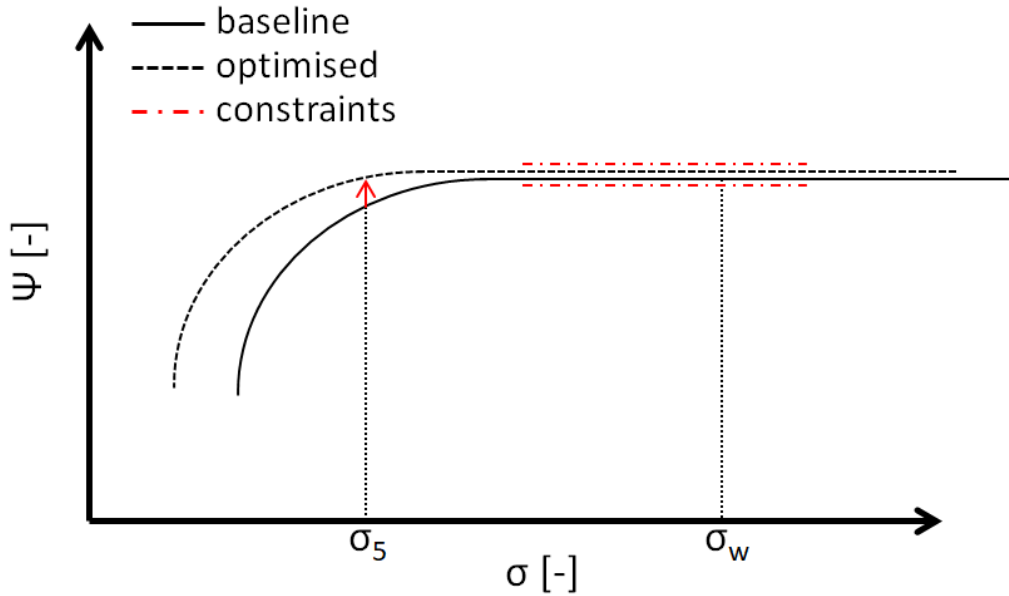


Figure 4.2: Optimisation strategy: head coefficient at critical cavitation number σ_5 is maximised.

4.3. Parametrisation of inducer geometry

Correct choice of parameters is crucial for every optimisation problem. The geometry of the baseline inducer is quite complex - it incorporates a curved hub and curved leading edge, as well as angle distribution changing along the span of the blade. Certainly not all of those features can be optimised due to limited computing power and difficulty to interpret the influence of many parameters on suction performance. Therefore the parameters must be carefully chosen and their number minimised. Table 4.1 shows requirements that were established to guide the parameters selection process. For clarity explanation for each requirement is given below the table.

ID	Requirement
GR1	The influence of the chosen parameters on suction performance of an inducer shall be unknown or unexplained according to the information found in literature.
GR2	The optimised inducer shall have the same theoretical wet head coefficient as the baseline inducer.
GR3	Any inducer created with the chosen parameters shall fit into the testing rig and match the impeller.
GR4	Any inducer created with the chosen parameters shall be suitable for 3D printing.
GR5	The number of parameters shall not exceed 5.

Table 4.1: Optimisation requirements.

GR1

As stated in the introduction the research related to cavitation in turbopumps was started already in the 1950s and the influence of several geometric parameters on the inducer suction performance is already known. One of the first complete inducer design guides describing these relationships were included in NASA publications summarising experience gathered during the

Space Race in the 1950s and 1960s [2, 23–25]. These basic guidelines remain valid also today, what can be confirmed by a constantly growing number of publications referring to them. Thanks to this research we can say that:

- Inlet area should be as high as possible to minimise inlet flow velocity. As a result inlet hub diameter should be as low as possible and inlet tip diameter should be as high as possible.
- Outlet hub diameter is usually fixed by impeller requirements. However, it is beneficial to have a higher hub diameter at the outlet to increase the head of an inducer through centrifugal forces. Outlet tip diameter should be matched to the impeller.
- Incidence angle of the leading edge should be in the range from 1° to 4° to avoid excessive flow acceleration at the suction side of the blade.
- For the best suction performance at a fixed flow rate the leading edge should be as sharp as possible. If the pump has to operate at partial flow rates an elliptical leading edge is more beneficial as it is less sensitive to changing incidence angle. Nevertheless the thickness should be as small as possible and is limited by the strength requirements.
- Shape of the trailing edge has a minor influence on inducer suction performance.

GR2

Theoretical head coefficient of an inducer can be calculated from the Euler’s turbine equation and outlet velocity triangle. Identical theoretical wet performance of both inducers is required in order to simplify the comparison process. If the simulated or measured performance of the optimised inducer is different than the performance of the baseline design it is easier to find the reason for it.

GR3 and GR4

Both baseline and optimised inducer should be 3D printed and tested in a dedicated testing rig located in Osaka University of Technology. It imposes several constraints on the size of the inducer. First, let’s consider the manufacturing constraints. The Fluid Machinery Lab at OIT uses UP Plus 2 printers for creating parts for testing, which basic specifications are given in Table 4.2. During this project all parts were printed with ABS because its mechanical strength is better than the in the case of PLA [26].

Property	Value
Printing material	ABS or PLA
Layer thickness	0.15 - 0.40 mm
Nozzle diameter	0.4 mm
Print Speed	10 – 100 cm ³ /h
Printing volume	245 x 260 x 350 mm
Extrusion temperature	ABS: 260-270 °C, PLA: 200 °C
Platform temperature	ABS: 100 °C, PLA: 50 °C

Table 4.2: UP Plus 2 3D printer specifications [27].

The constraints that have to be taken into account are the dimensions of the individual ABS layer: its thickness and width, determined by nozzle diameter. They constraint the minimal dimensions that can be resolved by a printer.

Another constraint on the choice of the blade parameters are imposed by the dimensions of the test rig. The tip diameter is limited by a fixed diameter of a casing equal to 67.5 mm. The inlet hub diameter must be higher than 10 mm because of a screw that is used to attach the inducer to the shaft. The outlet hub diameter must be equal to the impeller inlet diameter equal to 32 mm. These dimensions provide an envelope for the design of the optimised inducer.

GR5

A feasible number of parameters taking into account available computing power. Based on the experience gained during a similar thesis at TU Delft [22].

In the previous chapter it was shown that a full blade definition consists of three parts: meridional profile, blade angle distribution and thickness distribution. Derived requirements allow to make a first cut of the parameters that certainly will not be useful during optimisation. The following parameters were eliminated:

- Blade and hub diameters along the blade (GR1, GR2, GR3) - diameters of the inducer are fixed by the testing rig dimensions and in order to achieve the same theoretical wet performance as in the baseline design.
- Thickness distribution (GR1, GR4) - influence of blade thickness on suction performance is already known. In addition available 3D printer would not be able to accurately reproduce changes in blade thickness.
- Trailing edge shape and outlet angle (GR1, GR2) - influence of trailing edge shape on suction performance is small and the outlet angle is fixed in order to achieve the same theoretical performance.

After the first cut the following parameters remained:

- Position of leading and trailing edges in the meridional view
- Shape of the leading edge
- Blade angle distribution along the blade at different spanwise layers

The design of a leading edge is crucial for suction performance as it is in the region of the lowest pressure. Existing design guidelines suggest that introducing a swept leading edge, that can be defined with radius r_s and angle λ as shown in Figure 4.3, significantly improves suction performance of an inducer [5, 7, 24]. The effect of the round leading edge on suction performance was already investigated [28–30] and improvement of suction performance confirmed. However, the explanation is relatively vague and states: "This disappearance of cavitation bubbles with different cuttings is related to the favourable reorganization of the velocity field at the inducer". At the same time it is not clear if the sweep should be as big as possible or maybe there is an optimal value, therefore those two parameters were chosen for optimisation.

The incidence angle also has a big impact on suction performance as it hugely influences the pressure distribution at the leading edge. It was already mentioned that the incidence angle should be between 1° and 4°, but it was never investigated how adding sweep interacts with different incidence angles. Because of that the incidence angle was chosen as the third parameter.

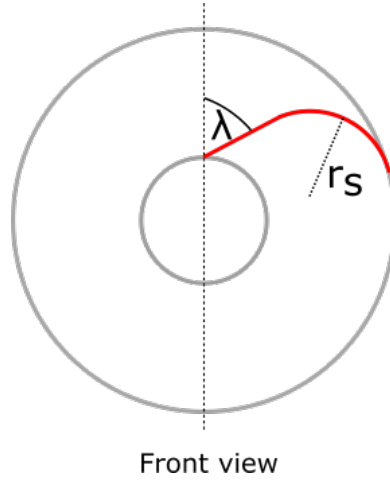


Figure 4.3: Parametrisation of a leading edge shape with sweep angle λ and sweep radius r_s .

Contrary to the leading edge, shape of the trailing edge has a minor impact on the suction performance and it will remain as in the baseline design. This means a radial trailing edge with the same outlet angle. On the other hand, position of the trailing edge in the meridional profile does matter, as it defines the length of the blade and different blade lengths are also reported to influence the suction performance. In literature blade length is usually represented indirectly, through a parameter called solidity, s . It is a ratio of the spacing between the blades at the tip, denoted L , and the chord length of the blade, denoted C . It represents the ratio of channel flow length to its width. It is measured at the tip because cavitation starts there. Figure 4.4 shows these lengths on a 3D view of an inducer. The spacing between blades at the tip can be calculated from the tip diameter D_{T1} and number of the blades n :

$$\begin{aligned} S &= \frac{C}{L} \\ L &= \frac{\pi D_{T1}}{n} \end{aligned} \tag{4.4}$$

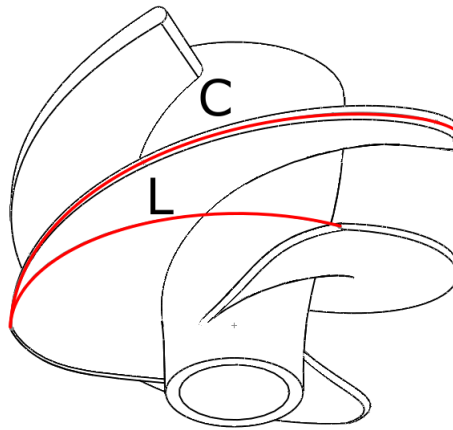


Figure 4.4: Blade chord length at the tip C and spacing between blades L used to define blade solidity.

A longer blade provides more space for the cavity to collapse and therefore should have a better suction performance. Recommended values of solidity lie within a considerably wide range: from 1.5 to 2.5. Decreasing this uncertainty would certainly help during the design stages. It is also not clear if it is an independent parameter or the shape of the leading edge influences it. As solidity is an important parameter that is chosen early in the design process due to its relationship with length of the blade, it was decided to include it in the optimisation process.

As a result of this analysis four parameters were chosen for optimisation:

- Sweep angle λ
- Sweep radius r_s
- Solidity s
- Incidence angle i

The following parameters will not be optimised and remain fixed with respect to the baseline inducer:

- Hub and tip diameters along the blade
- Outlet angle distribution along the span of the trailing edge
- Blade thickness and trailing edges shape

4.4. Design of Experiment

Each optimisation starts from a Design of Experiment (or DoE) that is necessary to build a response surface. During a DoE the design space is sampled by evaluating objective function at a finite number of design points. Sampling is required to build a response surface and reduce the computational cost of the optimisation. Obviously a choice of sampling points has a huge influence on the accuracy of the response surface. During this project an Optimal Space Filling (OSF) method was used that is an extended version of the Latin Hypercube Filling (LHF) method. In both methods the design space is divided into s^n equally spaced boxes, where s is a number of parameters and n is the number of design points. Then the boxes are randomly filled in a way that ensures that no point shares the same row with any other point with respect to all the parameters. This approach ensures that no part of the design space will be sampled more than once, what would be a waste of computing resources. At this point the LHF algorithm is finished, however it may happen the randomly chosen design points will be concentrated in a certain part of the design space, leaving the rest of it poorly sampled. The OSF method provides a solution to this problem by additionally maximising the distance between the points and provide the most even coverage of the design space. The difference between both methods can be easily visualised in a case with two parameters, as shown in Figure 4.5. It is clearly visible that the OSF method provides a more even distribution of sampling points. Number of points required to make an accurate response surface depends on the complexity of the investigated problem. The minimal recommended number is twice the number of the parameters. However, due to the complexity of the cavitating flow combined with a relatively large design space, many more are expected. The final number will be established during the process of response surface refinement.

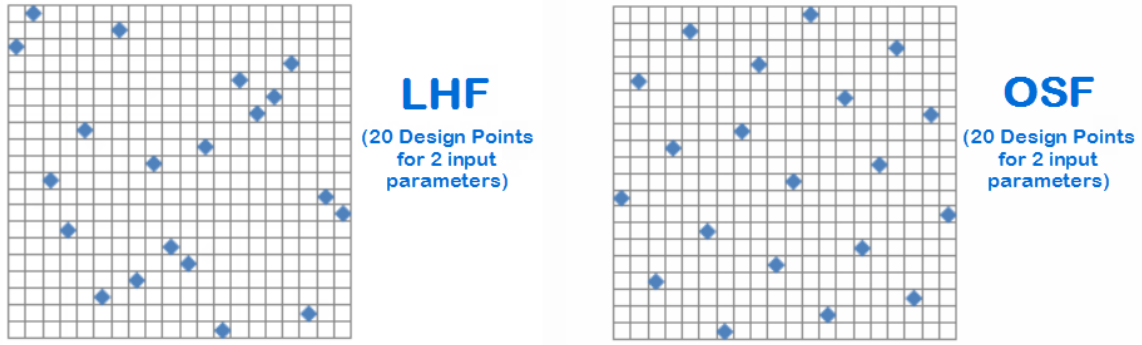


Figure 4.5: Comparison of Latin Hypercube and Optimal Space Filling methods. [31]

4.5. Geometry generation

Once the design points are selected their performance must be simulated. Each set of parameters defining a single design is transferred to the geometry generation module through the parameters manager. There the parameters are translated into a 3D model of a blade in two steps. First the parameters are loaded into an Excel file that calculates the θ angle distribution at several spanwise layers and the shape of the meridional profile of the blade. The complete design of the blade is then transferred to the Design Modeller, a CAD software used in the Ansys Workbench package. The construction of inducer geometry from the parameters is made in several steps. It begins with the reconstruction of the leading edge shape from two of the parameters: sweep angle and sweep radius. This is done by calculating the θ_1 at different spanwise layers as shown in Figure 4.6. This angle defines the profile of the leading edge as seen in the front view. Introduction of sweep combined with a straight, radial leading edge leads to unfavourable blade curvature near the tip. Figure 4.7 provides an example of such curved blade.

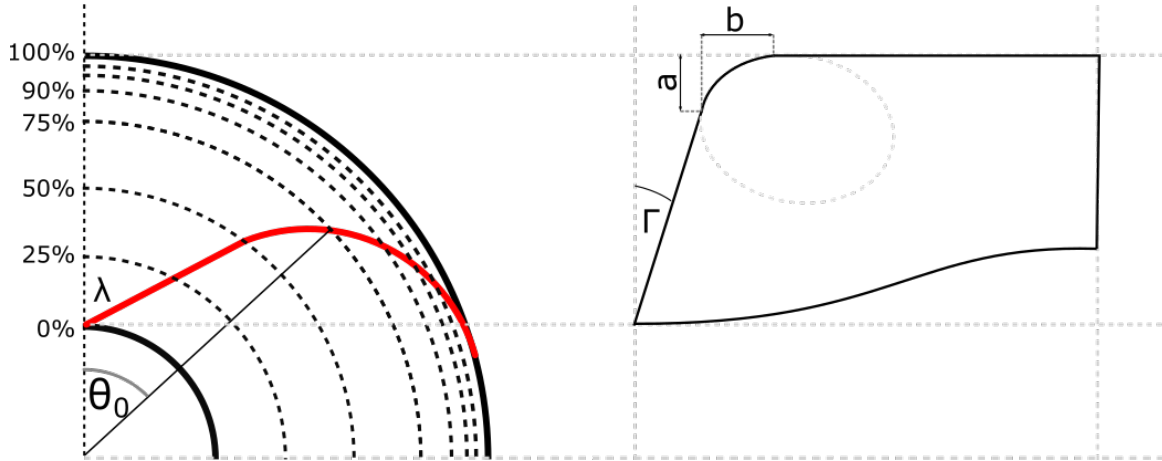


Figure 4.6: Leading edge and meridional profile reconstruction from the design parameters.

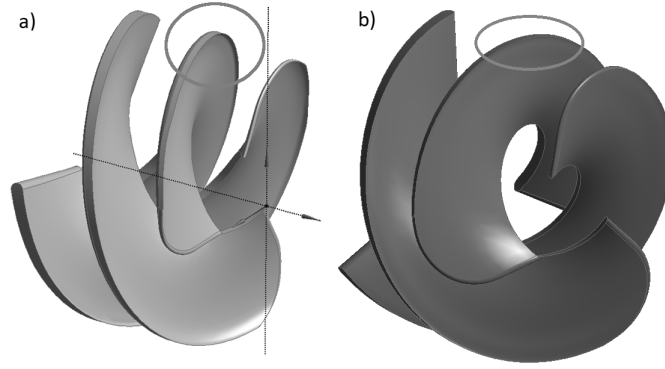


Figure 4.7: Comparison between a) a blade curved at the tip and b) a blade with correct tip.

In order to understand why this curvature exists the distribution of θ_B blade angle along the blade span must be examined. First, let's consider a blade with straight, radial leading edge. If there is no sweep the $\theta_B(Z)$ should be the same for each spanwise layer. Example of such blade is shown in Figure 4.8.

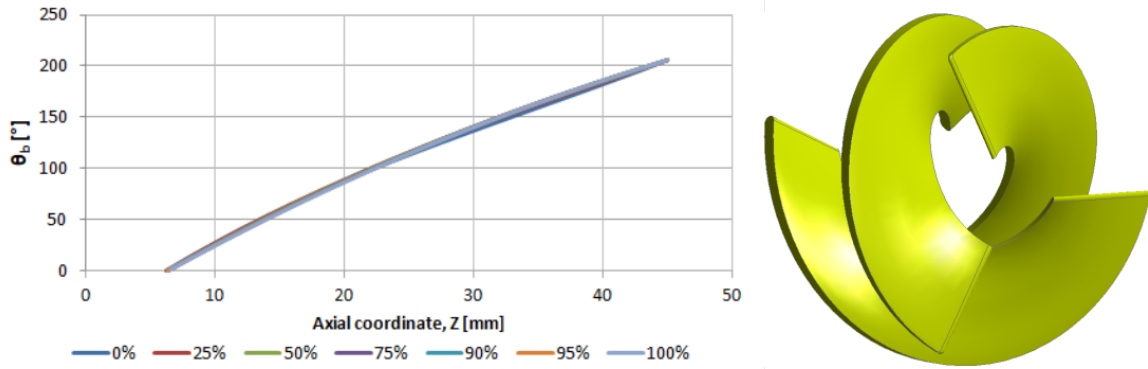


Figure 4.8: Blade with no sweep and radial leading edge.

When sweep is applied $\theta_B(Z)$ changes along the span but the axial position of the leading edge remains the same. As a result the tip of the leading edge starts curving and the blade is no longer straight. Such case is shown in Figure 4.9.

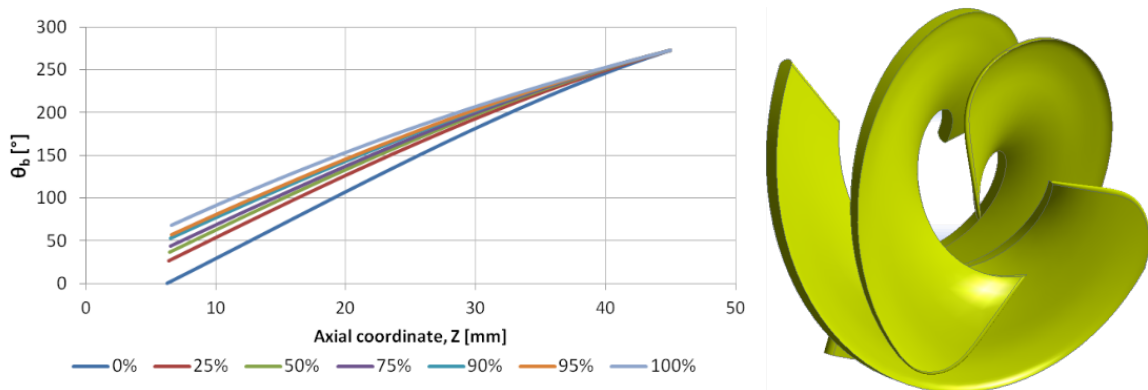


Figure 4.9: Blade with sweep and curved tip

To fix this geometry problem the meridional shape of the leading edge must be adjusted by

leaning it backwards. As the curvature increases near the tip, the blade must be leaned stronger. Therefore the shape of the leading edge is made of two parts: a straight line that is inclined with respect to the radial direction at angle Γ and a part of an ellipse that is tangent to this straight line. The dimensions of the ellipse are controlled by two parameters, a and b that determine the point of transition between the line and ellipse, as well as how far the tip of blade is moved backwards. A blade with correct tip is shown in Figure 4.10. As in the first case θ_B follows a single curve at every spanwise layer.

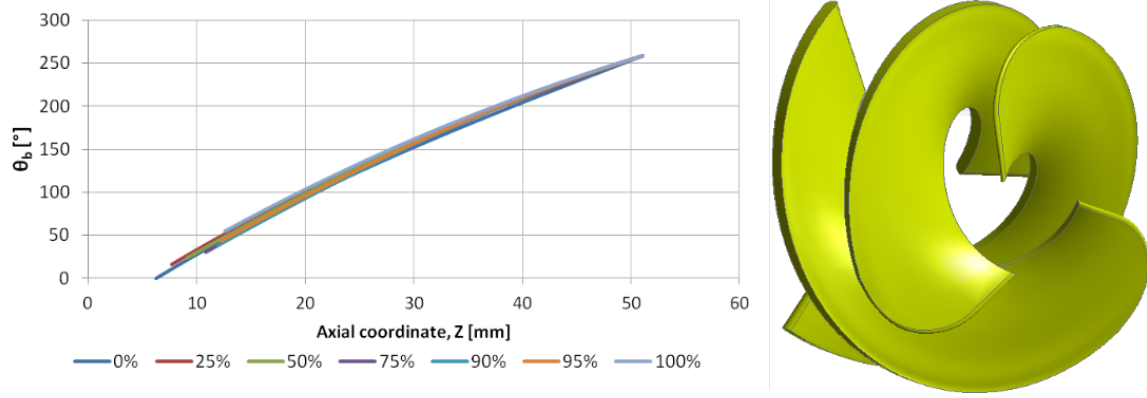


Figure 4.10: Blade with sweep and no curvature.

The values of new parameters Γ , a and b , are expressed as a functions of already existing parameters, λ and r_s . To find a correct ratio between them a value of the following expression was minimised:

$$e = |\theta_{tip-LE} - \theta_{hub}[Z_{tip}(\Gamma, a, b)]| \quad (4.5)$$

It expresses the difference between the θ_B angle of the leading edge tip and θ_B angle resulting from the angle distribution at the hub at axial position of the tip. Graphical interpretation of e is shown in Figure 4.11. It would be interesting to see how different values of Γ , a and b influence inducer suction performance. However, it was noticed that many combinations lead to an incorrect geometry. Adding another three parameters to the design space would also greatly increase the cost of optimisation. Because of this reasons the relationship between leading edge sweep and its meridional profile remained fixed. It was found that the following values can be used for all designs:

$$\Gamma = \frac{\lambda}{7}, \quad a = r_s, \quad b = 0.4r_s \quad (4.6)$$

Once the meridional profile of a blade is established its blade angle distribution is determined. Blade angle calculations are based on θ_B angle, which distribution is defined at each layer shown in Figure 4.6. First the angle at the tip is determined using the following conditions:

- Angle at the leading edge is equal to θ_1
- Inlet β_1 angle calculated from the flow angle and given incidence angle
- Outlet β_2 angle taken from the baseline design

β angle defines the value of the derivative of the θ angle function, according to Equation 4.7. With these three conditions a second order polynomial is used to define the θ angle as a function of a meridional distance along the blade. Then length of the blade is adjusted to

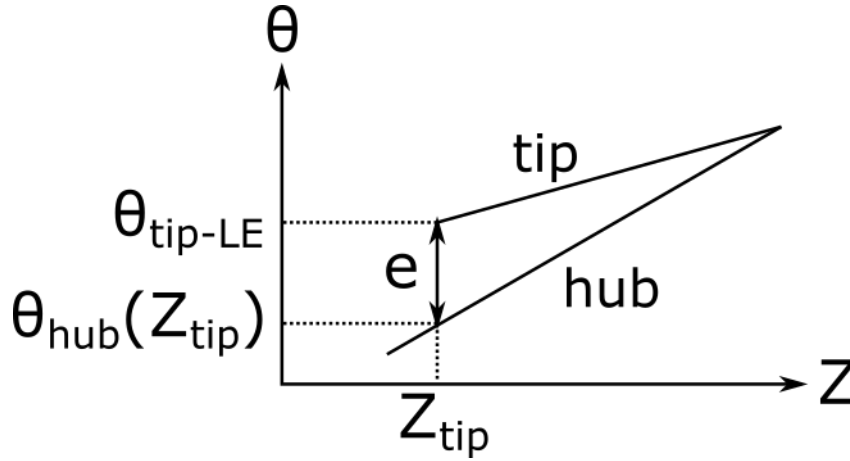


Figure 4.11: Graphical interpretation of the error between the hub and tip θ angle distributions.

achieve the desired solidity at the tip. This in return allows to compute the θ_2 angle that defines the position of the trailing edge.

$$\beta = \text{atan} \left(\frac{\delta\theta \cdot R}{\sqrt{\delta Z^2 + \delta R^2}} \right) \quad (4.7)$$

θ angle distribution at the rest of the layers is computed in a similar way. However, four parameters are used instead of three to ensure that the trailing edge at each layer will have the same θ_2 angle. This is necessary to obtain a straight and radial trailing edge, similar to the one in the baseline design. Exact equations and algorithms used for blade design are given in Appendix A.

4.6. Inducer design example

The design method presented in the previous section allows to create a wide range of inducer geometries. In this section one example geometry is presented to show how it compares with the baseline geometry. Table 4.3 shows the values of the parameters adopted for this design. They were chosen to conserve the incidence angle at the tip of the blade and the axial length of the blade.

Sweep angle	60
Sweep radius	11.875 mm (50% of the span)
Incidence angle	2°
Solidity	1.61

Table 4.3: Parameters defining the example design.

The comparison between blade angle distributions in Figure 4.12 shows that indeed the blade angle at the leading edge tip is conserved. However, at other locations blade angles deviate from the baseline design, especially at the hub. The difference in leading edge meridional shape is shown in Figure 4.13. The importance of these differences is discussed in the next chapter.

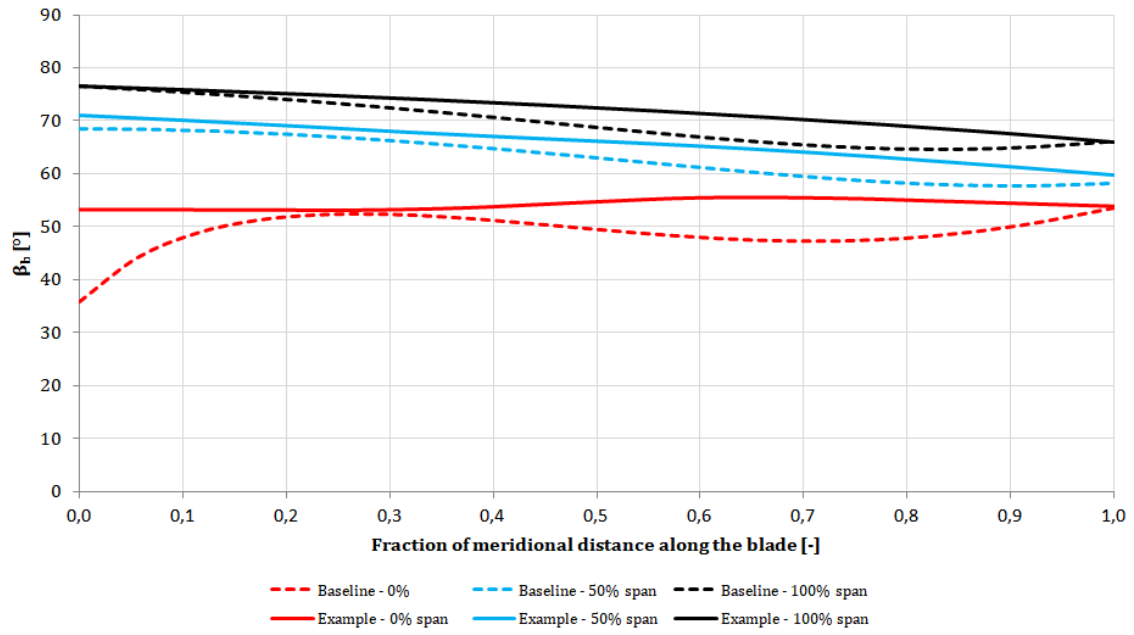


Figure 4.12: Comparison between baseline and example inducer blade angle distributions.

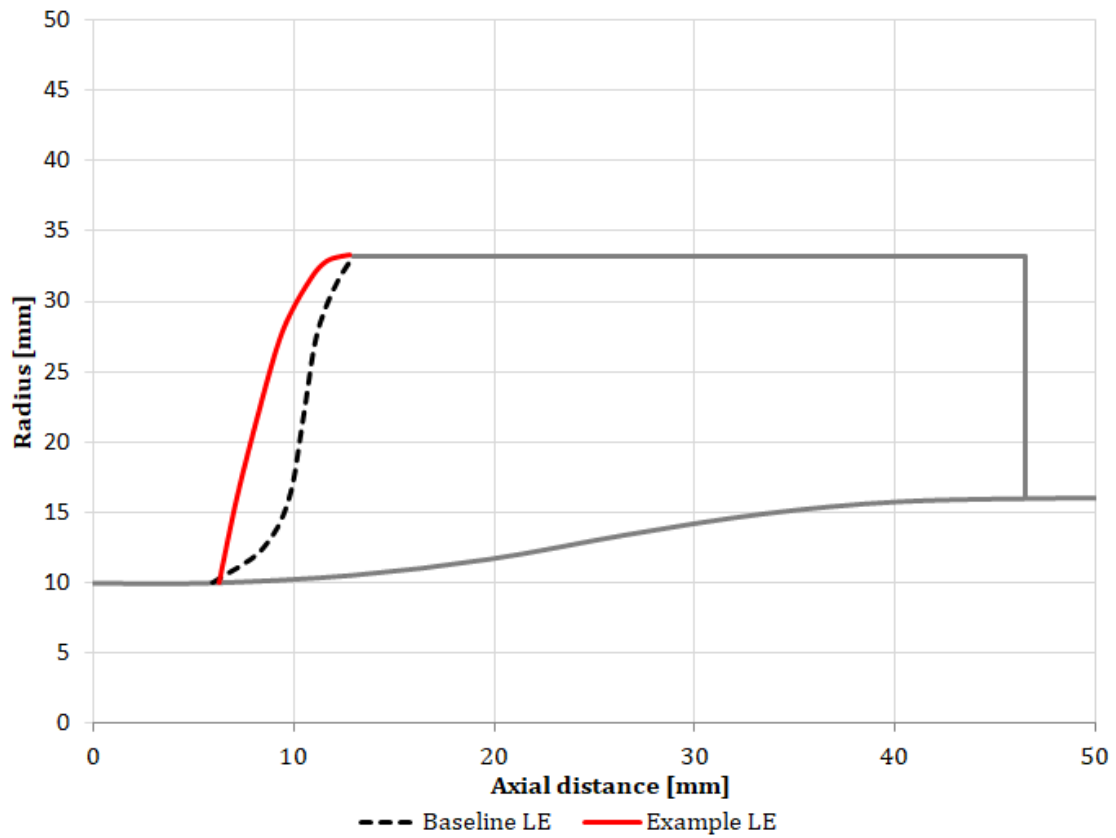


Figure 4.13: Comparison between baseline and example inducer blade meridional profiles.

4.7. Meshing

High quality mesh is crucial for fast and accurate CFD simulations. It is especially important during an optimisation, because high number of elements may significantly increase the computational cost of the entire process. At the same time the mesh must be adaptive, which means that it has to automatically adjust to a new geometry. It is necessary as a large number of geometries will be evaluated. To simplify mesh generation process, the mesh is divided into three pieces: inducer mesh, impeller mesh and outlet mesh. The entire fluid domain in the meridional view with highlighted divisions between parts is shown in Figure 4.14. The inlet length is equal to five diameters of the inducer because of the backflow that may occur through the tip gap of the inducer. To reduce the size of the mesh, only one flow channel is simulated. It is possible because both inducer and impeller are rotationally symmetrical, with segments rotated by 120° with respect to each other. Inducer and impeller meshes are created in *TurboGrid*. It is a meshing software in Ansys Workbench package that is dedicated to meshing turbomachinery flow channels. TurboGrid can be easily connected with Design Modeller to automatically share the geometry data of the blade and entire flow path. This feature allows for fast mesh update when the geometry changes. The mesh created by TurboGrid is structural, which means that it is made of hexahedra cells. This type of mesh gives better convergence and higher resolution when compared to unstructured mesh (made of tetrahedra) with the same number of elements. Figure 4.15 shows the structured topology of the mesh in the middle of the span of the inducer blade.

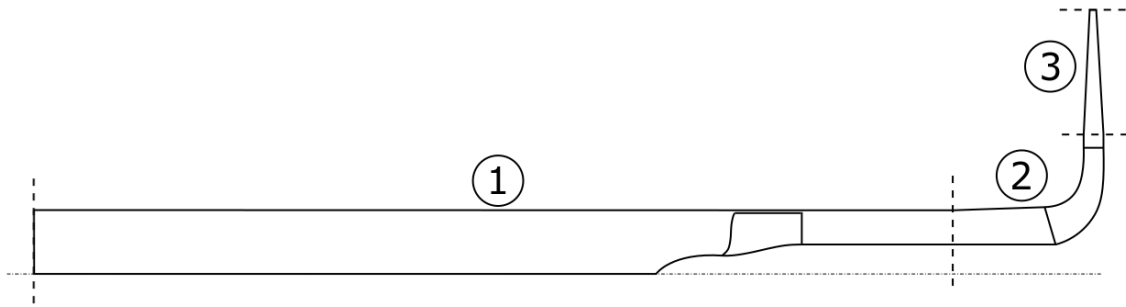


Figure 4.14: The division of the computational domain into three parts of the mesh: inlet with inducer, impeller and outlet.

Structured mesh allows to reduce the number of elements in the mesh. Still, nearly 3 million elements are required to obtain mesh independent solution. Grid independence was judged by looking at two head coefficients: of the inducer and of the entire pump. The result of the study are shown in Figure 4.16. The mesh is considered converged when the solution changes by less than 1% with increasing cell count. In this case it happens when the mesh has around 2.87 million cells: 1.53 million in the inducer part, 0.99 million in the impeller part and 0.34 million in the outlet mesh.

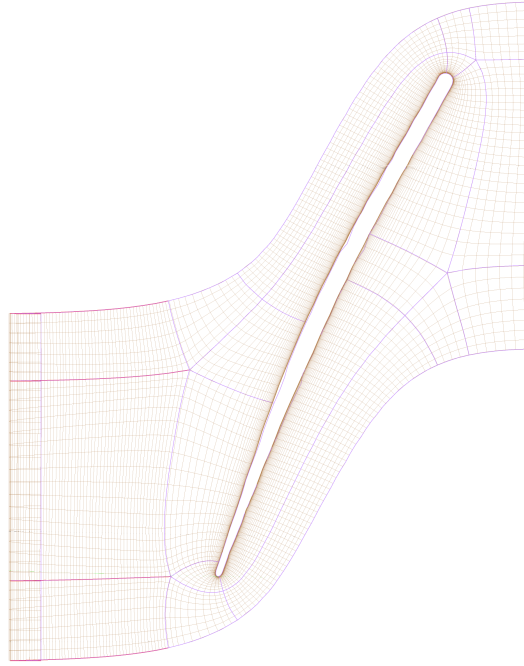


Figure 4.15: Mesh topology in blade-to-blade view.

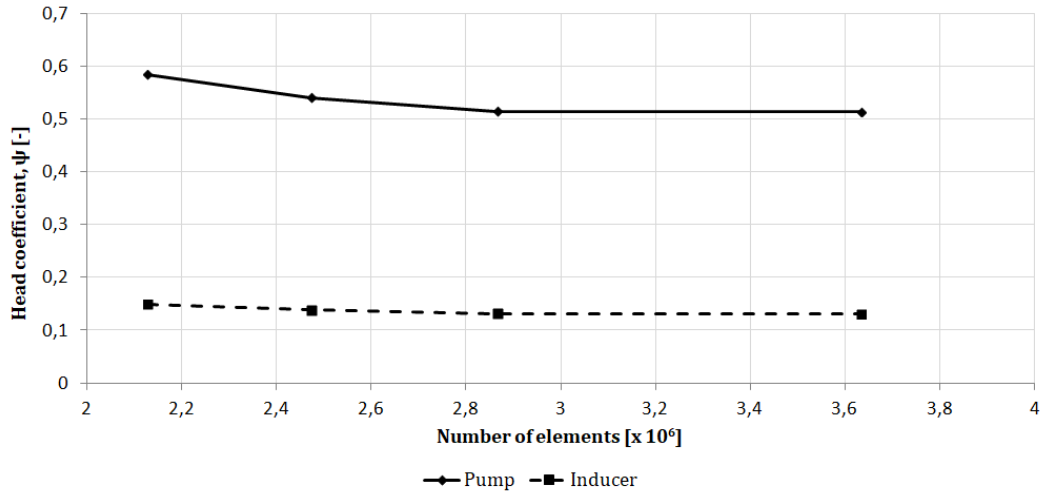


Figure 4.16: Solution convergence with increasing number of elements.

The outlet geometry visible in Figure 4.14 had to be introduced because of adapting single flow channel calculation method. The real pump is enclosed by a volute that is connected to the discharge pipe. Unfortunately the volute is not symmetrical and cannot be used in this kind of calculations. The influence of this change was already investigated in a MSc thesis investigating the the influence of splitter blades on the suction performance of the impeller used in this project [22]. The difference between the simplified outlet and the real volute is shown in Figure 4.17. The biggest difference is the absence of the leakage flow between the casing and the shroud of the impeller, indicated by an arrow in Figure 4.17. In return the simulated performance is higher than the experimental one. However, during an optimisation process the absolute performance is less important than the relative differences between different designs. Additionally, a simplified geometry provides faster convergence and stability of the numerical

simulations. Because of these reasons the simplified outlet was used through the entire project.

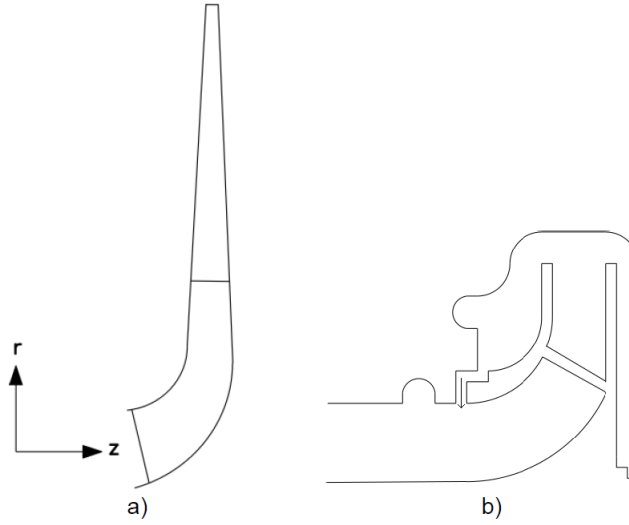


Figure 4.17: Two versions of the outlet: a) simplified for calculations, and b) the real volute [22]

4.8. Solver setup

Two types of simulations were done during this project: without cavitation and with cavitation. Both of them are done in Ansys CFX solver. It uses a finite volume method to numerically solve Reynolds Average Navier-Stokes equations. RANS equations are used with $k-\omega$ Shear Stress Transport turbulence model. This model allows to predict flow separation under adverse pressure gradients what can occur in a pump. Flow is considered incompressible and RANS equations are solved in a rotating reference frame to simulate the rotation of the blades in a steady state simulation. The boundary conditions of the simulations are presented in Figure 4.18. This setup is recommended for cavitation simulations in CFX manual [31]. As mentioned in the previous section 1/3 of the fluid domain is simulated with periodic interface used on the side walls.

The flow coefficient of the simulation is adjusted by changing the mass flow at the outlet of the domain. Cavitation number is controlled by two parameters, inlet pressure and vapour pressure of the fluid at given temperature. Basic operating condition of the simulation are presented in Figure 4.4. They describe the nominal design point of the pump and at these conditions the cavitation does not occur.

Rotational speed	3600 RPM
Mass flow at the outlet	2.77 kg/s
Total pressure at the inlet	101.325 kPa
Water vapour pressure at 25 °C	3.169 kPa

Table 4.4: Pump operating conditions used during simulation.

To simulate cavitation in the flow channel a two-phase model must be used. In this case a homogeneous model is recommended which assumes that there is one flow field for both phases

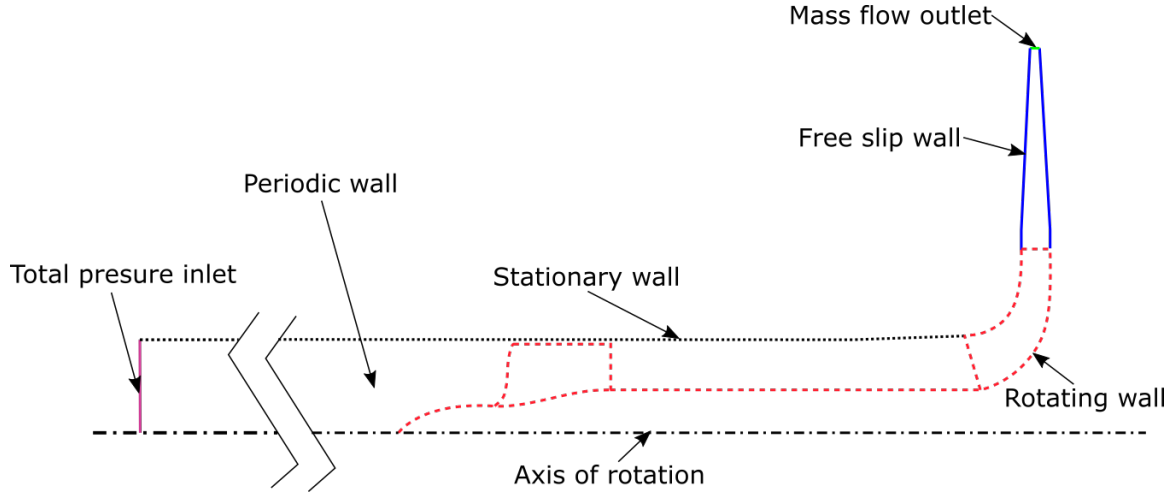


Figure 4.18: Boundary conditions of the simulation.

[32–34]. The mass transfer between phases is controlled by Rayleigh-Plesset equation, that defines vapour generation and condensation rates of a spherical bubble. With this equation the change of bubble volume, V_B , is expressed in the following way:

$$\frac{dV_B}{dt} = 4\pi R_B^2 \sqrt{\frac{2}{3} \frac{p_v - p}{\rho_f}} \quad (4.8)$$

where R_B is the radius of the bubble, p_v is the pressure inside the bubble (equal to vapour pressure), p is the pressure of the liquid around the bubble and ρ_f is the density of the fluid. The summary of the basic solver settings is shown in Table 4.5. More information about all the models and their implementation can be found in the Ansys CFX manual [31].

Multiphase model	Homogenous, Isothermal (25 °C)
Turbulence model	k- ω SST
Cavitation model	Rayleigh–Plesset
Spatial discretisation	Second order

Table 4.5: CFX solver setup.

4.9. Baseline simulation results

Simulation setup explained in the previous sections was used to simulate the performance of the baseline design. The results provide the reference level for the optimisation. First the wet performance was evaluated that is shown in Figure 4.19. The static head coefficients of the entire pump and the inducer at a nominal flow coefficient $\phi = 0.204$ are equal to 0.515 and 0.132 respectively. As expected the the head of the pump decreases with increasing flow coefficient. At the highest simulated flow coefficient, $\phi = 0.331$ the inducer is no longer able to increase the pressure. The efficiency of the pump is calculated from its definition presented in Chapter 2:

$$\eta = \frac{Q \Delta p_s}{\omega T} \quad (4.9)$$

Volume flow Q and rotational speed ω are the inputs to the simulation. Static pressure rise p_s and torque T acting on the rotor must be extracted from the solution file. The torque is estimated by integrating the forces acting on the rotor. Such force consists of two components:

- Pressure component calculated from the pressure distribution on the given surface
- Viscous component calculated from the shear stresses in the boundary layer

In the case of the baseline pump the efficiency calculated in this way peaks at the design point at a value of 84.6%. The efficiency is likely to be largely overestimated due to the lack of modelling of the leakage flow through the gap between the impeller shroud and casing. Because of that it is impossible to tell how much torque is required to overcome the friction in this gap and how much the static pressure at the outlet is decreased.

Simulation of suction performance allowed to estimate the critical cavitation number. In literature, a critical cavitation is defined as a cavitation number at which 5% drop of head occurs. Simulated cavitating characteristic shows that for the baseline design 5% drop of head occurs at $\sigma = 0.0473$. This number was adapted as a reference value during the optimisation process. Figure 4.20 presents the entire cavitation characteristic of the pump.

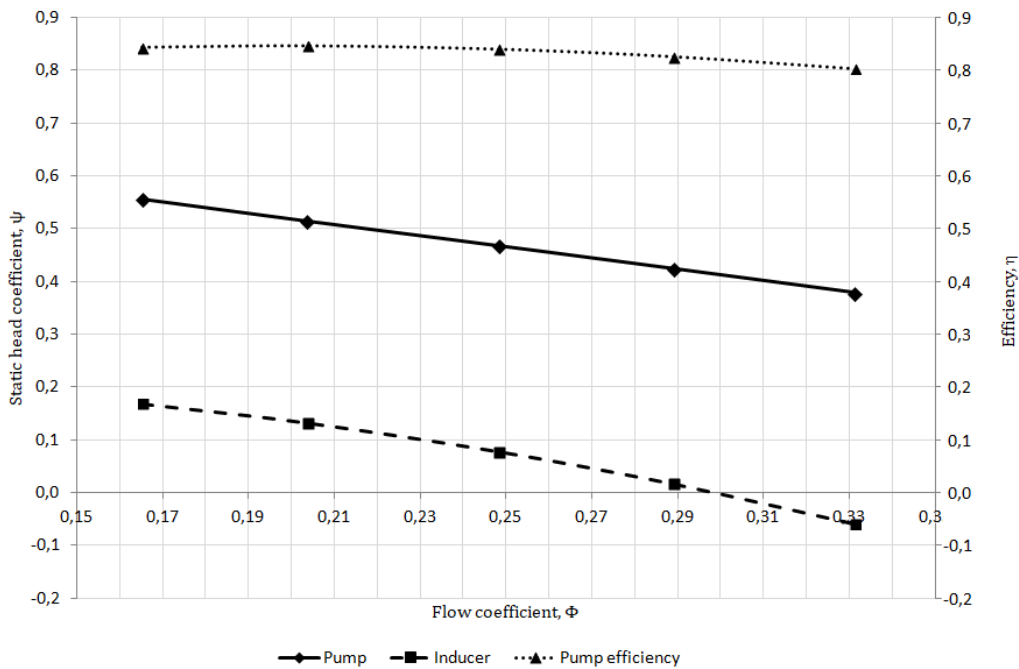


Figure 4.19: Simulation results of baseline wet performance.

4.10. Response surface

Once the design space is sampled and the performance of all the designs is known a response surface may be built. Generally speaking a response surface is a function that approximates the real relationship between the input and output parameters. Ansys Workbench provides several types of response surfaces. They can be divided into two categories: parametric and

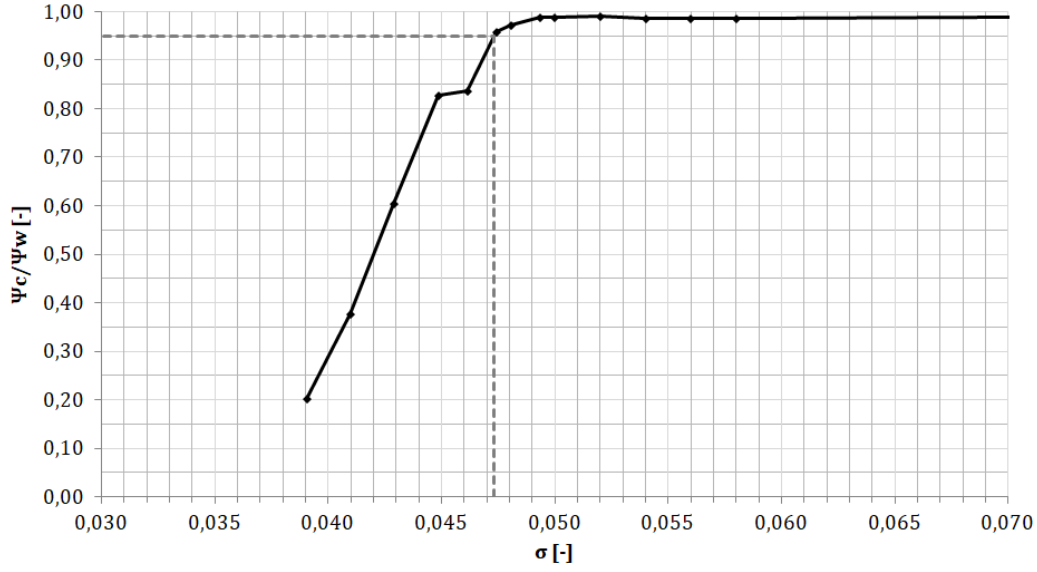


Figure 4.20: Simulation results of baseline suction performance.

non-parametric regressions methods. Parametric response surface takes a predetermined form, while non-parametric one is but is constructed according to information derived from the data. The choice of the response surface is aided by information provided by Workbench and estimating goodness of fit for a given surface. Three main parameters are used:

- Coefficient of Determination (R^2) - The percent of the variation of the output parameter that can be explained by the response surface regression equation. The best value is 1 and it occurs when the response surface passes directly through all the sampling points. Mathematically expressed as:

$$R^2 = 1 - \frac{\sum_{i=1}^N (y_i - \hat{y})^2}{\sum_{i=1}^N (y_i - \bar{y})^2} \quad (4.10)$$

where y_i is the value of the output parameter at the i -th sampling point, \hat{y}_i is the value of the regression model at the i -th sampling point, \bar{y} is the arithmetic mean of the values y_i , and N is the number of sampling points.

- Root Mean Square Error - the square root of the average square of the residuals at the DOE points for regression methods. The best value is 0. Mathematically expressed as:

$$RMS = \sqrt{\frac{1}{N} \sum_{i=1}^N (y_i - \hat{y})^2} \quad (4.11)$$

- Relative Maximum Absolute Error - the absolute maximum residual value relative to the standard deviation of the actual output data, modified by the number of samples. Best value is 0. Mathematically expressed as:

$$RMAE = \frac{1}{\sigma_y} \frac{1}{N} \sum_{i=1}^N Abs(y_i - \hat{y}) \quad (4.12)$$

The procedure of response surface type choice is based on those parameters. It is recommended to start with the simplest parametric type based on 2nd-order polynomials and verify the goodness of fit. If they are far from the ideal values then the non-parametric approach should be used. This situation occurs when the response contains higher order terms. It is expected that the non-parametric response surface will be used due to complexity of the 3D cavitating flow.

4.11. Optimisation algorithm

Optimisation algorithm is required to choose the best possible design from the response surface. During the process of response surface generation and refinement a Screening algorithm is used. It chooses a specified number of samples from the response surface and sorts them by the value of the objective function. This simple approach proves to be very powerful as it is quick, avoid problems with convergence, supports multiple goals and constraints and is able to find the global maximum. When the response surface is converged and the potential optimal candidate found by the screening method, a gradient-based optimisation algorithm called Nonlinear Programming by Quadratic Lagrangian. More information about both algorithms can be found in Optimisation Toolbox manual [31].

Optimisation results

5.1. Design space size

The size of the design space is defined by the range of the values that can be taken by the parameters. The ranges used at the beginning of the optimisation are showed in Table 5.1.

Parameter	Lower limit	Upper limit
Sweep angle, λ	20°	70°
Sweep radius, r_s	20% span	60% span
Incidence angle, i	1°	3°
Solidity, s	1.5	2

Table 5.1: Design space size.

The ranges of both sweep angle and sweep radius are in this case limited by the ability of the mesh to adapt to the blade. The mathematical model used to generate the geometry of the leading edge works for sweep angle from 0 to 90° and for sweep radius from 0 to 100% of the span. However, at the extreme values of these parameters the blade geometry is less accurately generated in the Design Modeller and errors in the mesh may occur. The lower limit of the incidence angle is to ensure that the vapour bubbles will form only on the suction side of the blade. The upper limit is driven by the off-design performance of the pump. High incidence angle at the tip of the blade leads to high back-flow and occurrence of cavitation surge at partial flow rates [35]. Additionally, sharp leading edges often used in the inducers do not operate efficiently with high incidence angles. The choice of lower solidity limit is based on the information from the literature that suggest 1.5 as a minimal value for a good inducer. The upper limit was chosen so that the trailing edge would not be placed too far from the tapered part of the hub. This makes finding the difference between the baseline and optimise designs easier. If during optimisation the optimum is found at the edge of the specified design space, the limits should be changed and sampling redone.

With the results of the baseline inducer simulations the values of constraints imposed on the wet pump performance can be given:

$$\begin{aligned} 0.509 < \psi_{opt} < 0.540 \\ \eta_{opt} &\geq 84.6\% \end{aligned} \tag{5.1}$$

5.2. Optimisation

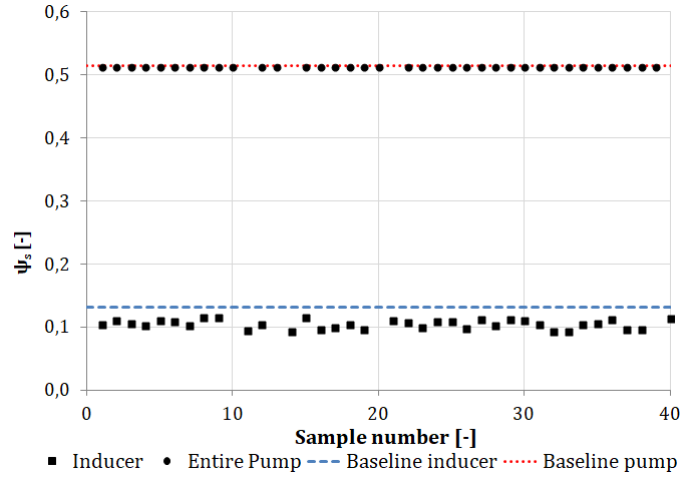


Figure 5.1: Wet performance the sampled designs.

To build a full quadratic model for 4 input parameters 16 samples are required. This number was doubled in the first Design of Experiment, because the quadratic model is expected to be a bad approximation of the real response surface. Additional 8 samples were added to compensate for the possibility of simulation crashing for certain designs. This may happen when the flow around the given blade separates or creates other unfavourable patterns. The geometry of such blade is then automatically discarded. Out of 40 designs in total this happened in 8 cases. The performance of each design was then simulated at two cavitation numbers: $\sigma_1 = 1.2$ and $\sigma_2 = 0.0473$. The former correspond to design, wet conditions and the latter to the critical cavitation number of the baseline design. The wet simulation must be done first to provide input for the cavitation simulation. The results of wet simulations are presented in Figure 5.1. It is clearly visible that generated inducers have a smaller static head coefficient than the baseline design. However, this characteristic has a little impact on the wet performance of the entire pump, because it is determined by the design of impeller that remained unchanged.

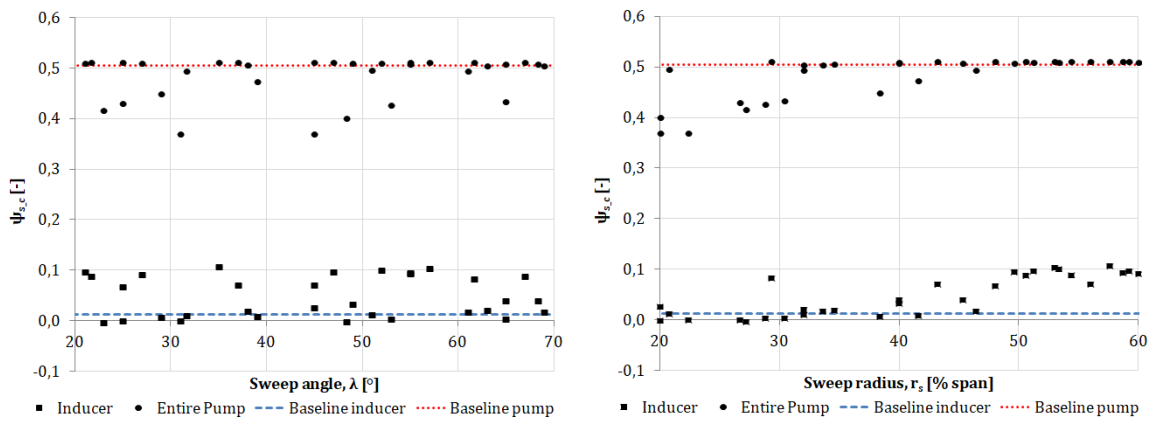


Figure 5.2: Suction performance of sampled designs as a function of sweep angle and sweep radius.

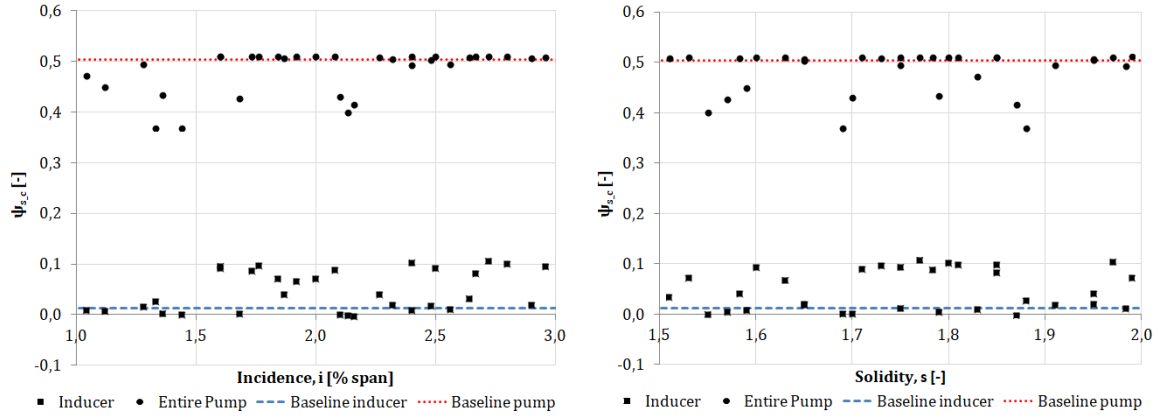


Figure 5.3: Suction performance of sampled designs as a function of incidence angle and solidity.

Much more variation between designs can be seen when looking at the results of cavitation simulations. They are presented as functions of each parameter in Figures 5.2 and 5.3. The performance of the sampled designs is compared with the performance of the baseline pump working with the same cavitation number. In case of sweep angle, incidence angle and solidity no trend can be observed - both bad and good designs are existing in the entire range of these parameters. However, this is not the case for the sweep radius, as high sweep radius (above 50% of the leading edge span) results in higher suction performance. These samples were used to create a response surface, predicting the wet and cavitating head coefficients, as well as efficiency at the design point. Both 2-nd order polynomial method and non-parametric regression methods were used and compared with the earlier specified criteria.

Parameter	Best value	2-nd order polynomial	Non-parametric regression
R^2	1	0.550	0.998
RMS	0	2.0e-4	1.3e-5
RMAE	0	182.2	4.4

Table 5.2: Quality of fit for two kinds of response surface.

Response surface based on non-parametric regression provides a much more accurate prediction of the objective function and was used for optimisation. Part of the response surface might be represented graphically as a function of two parameters, with the other two parameters fixed. Figure 5.4 presents the response surface as a function of sweep angle and sweep radius together with the design points used for its creation. Two major conclusions may be made from the shape of this response surface. The red area suggests that the optimum is within the selected design space. Unfortunately, the value of the cavitating head coefficient is overestimated, as it reaches 0.53, that is higher than the wet head coefficient of any of the sampled designs.

A screening algorithm with 3000 samples was used to find two candidate designs with the best suction performance that fulfil the requirements imposed on the performance at the design point. They are called C1 and C2. The values of parameters defining optimised designs are given in Table 5.3. The designs are very similar to each other, suggesting that there is one optimal region within the design space.

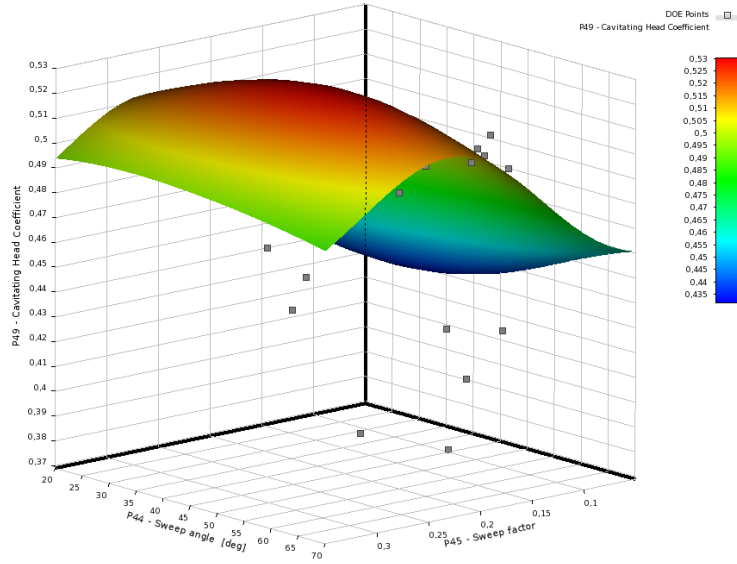


Figure 5.4: Response surface based on two parameters: sweep angle and sweep radius.

ID	λ [°]	r_s [% span]	i [°]	s [-]
C1	42.2	50	2.3	1.70
C2	38.2	48	2.5	1.75

Table 5.3: Parameters of the first candidate points of the optimisation.

These points were used to verify the accuracy of the response surface. Their predicted performance was compared with the actual simulation results. Table 5.4 presents this comparison. Subscript *pre* refers to the response surface prediction and *sim* to simulation results. As it was noticed before, the suction performance of the pump is overestimated.

ID	$\psi_{w,pre}$ [-]	$\psi_{w,sim}$ [-]	Diff [%]	$\psi_{c,pre}$ [-]	$\psi_{c,sim}$ [-]	Diff [%]	η_{pre} [%]	η_{sim} [%]	Diff [%]
C1	0.514	0.514	0	0.529	0.511	3.6	84.6	84.6	0
C2	0.514	0.513	0.2	0.526	0.510	3.1	84.7	84.6	0.1

Table 5.4: Comparison between the predicted and simulated performance of the first candidate designs.

The difference between prediction of the cavitating head coefficient based on the generated response surface and actual simulation results for candidate points is larger than 1% so the response surface is not converged yet. However, the difference is not significantly higher than the threshold value (3% compared to 1%) what suggests that an optimum exists in the specified area but its value is slightly overestimated. To refine the response surface it was decided to limit the design space and generate ten new points near the previously generated candidate points. The boundaries of the refined area are shown in Table 5.4.

Parameter	Lower limit	Upper limit
Sweep angle, λ	30°	60°
Sweep radius, r_s	50% span	70 % span
Incidence angle, i	1.5°	2.5°
Solidity, s	1.6	1.9

Table 5.5: Size of the refined design space.

Figure 5.5 shows the refined response surface. It can be seen that the response surface in this region is basically flat as the head coefficient changes between 0.5105 and 0.512. Figure 5.6 shows how efficiency changes with sweep angle and sweep radius. Although the difference between minimal and maximal efficiency are very small, it can be concluded that higher sweep angle and sweep radius result in lower efficiency. Therefore the trade-off must be made between ultimate suction performance and the best possible efficiency. Two optimisation algorithms were used on this surface: screening and gradient-based NLQPL. The candidate designs found by these algorithms are showed in Table 5.6.

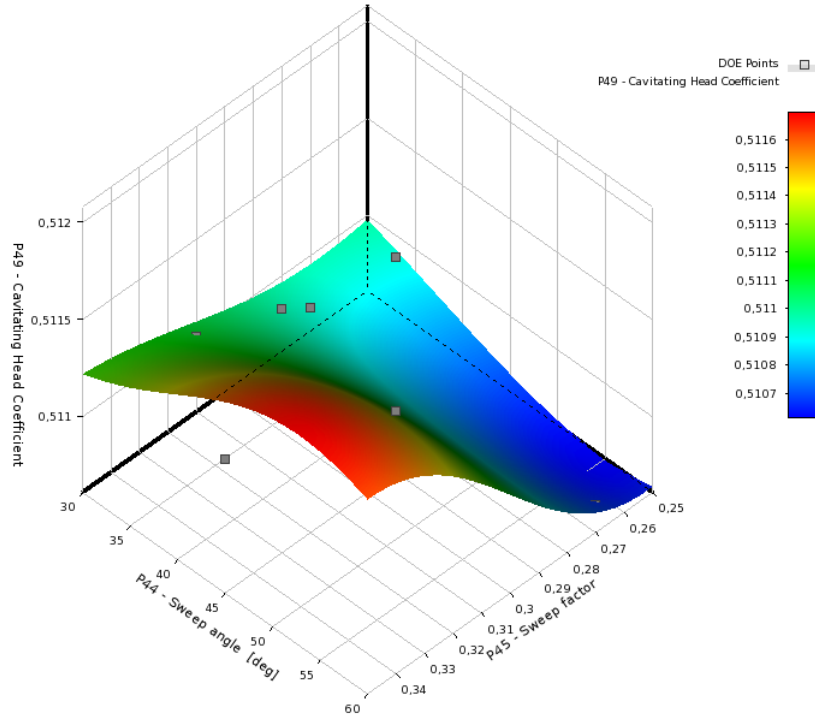


Figure 5.5: Refined response showing cavitating head coefficient based on two parameters: sweep angle and sweep radius.

ID	Method	λ [°]	r_s [% span]	i [°]	s [-]
C3	Screening	33.7	54	2.5	1.74
C4	NLQPL	33.9	57	2.4	1.79

Table 5.6: Candidate points obtained from the refined response surface.

The predicted and simulated performance of new candidate designs is shown in Table 5.7. This time the difference is smaller than 1% and the response surface is converged. Selected inducers are very similar to each other and so is their performance. However, the C4 candidate shows a

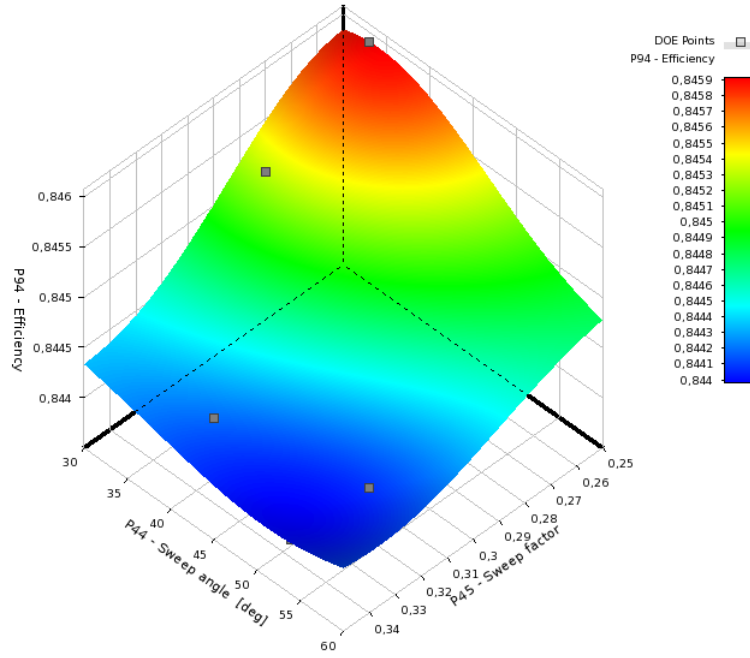


Figure 5.6: Refined response showing efficiency based on two parameters: sweep angle and sweep radius.

slightly higher head coefficient at chosen critical number and therefore was selected for further investigation.

ID	$\psi_{w.pre}$ [-]	$\psi_{w.sim}$ [-]	Diff [%]	$\psi_{c.pre}$ [-]	$\psi_{c.sim}$ [-]	Diff [%]	η_{pre} [%]	η_{sim} [%]	Diff [%]
C3	0.514	0.513	0.2	0.511	0.510	0.2	84.6	84.6	0
C4	0.514	0.513	0.2	0.511	0.511	0	84.6	84.6	0

Table 5.7: Comparison between the predicted and simulated performance of the candidate designs obtained from the refined response surface.

The performance of the C4 inducer was simulated at other cavitation numbers in order to determine the new critical cavitation number and estimate the improvement of the suction performance. Figure 5.7 shows the comparison between cavitating characteristics of the baseline pump and inducer and cavitating characteristic of the optimised pump and inducer. The critical cavitation number for the entire pump is decreased from 0.0473 to 0.043, resulting in 9.1% improvement of suction performance.

5.3. Improved blade design optimisation

The optimisation process described in the previous section proved that it is possible to obtain an inducer designed according to the specified method with a better suction performance than the baseline design. However, the static head coefficient of the optimised inducer is 18% lower than for the baseline design, despite the same outlet angle (optimised: 0.108, baseline: 0.132). Lower head of the optimised inducer operating without cavitation is clearly visible in Figure 5.1. It was found that the decrease of the head coefficient is caused by the increase of the slip angle, what can be seen while looking at spanwise profile of the absolute circumferential velocity

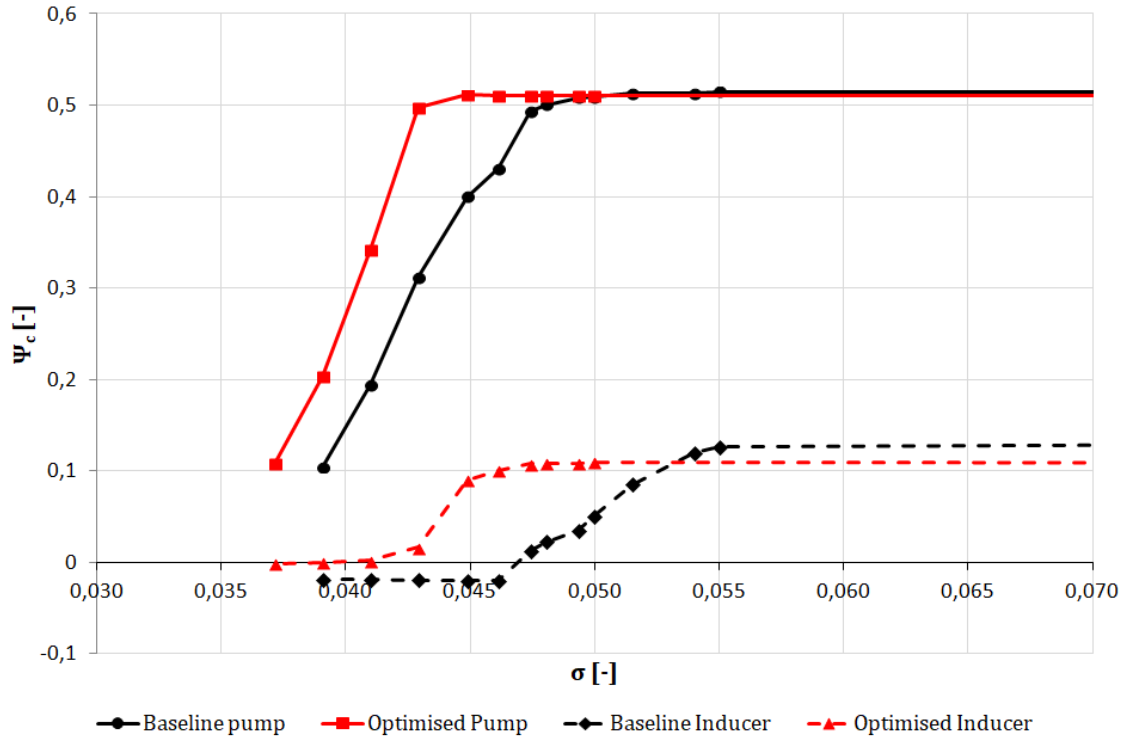


Figure 5.7: Comparison between the suction characteristics of baseline and optimised design.

just after the trailing edge of the inducer. Figure 5.8 shows that it is higher for the baseline design. This velocity determines the pressure rise of the inducer, as it was shown in Chapter 2, and therefore the head coefficient of the optimised design is lower. Wet performance of entire pump is higher than the specified threshold equal to 99% of the baseline head coefficient and suction performance improvement was achieved. Therefore the C4 candidate design could be the final product of the optimisation process. However, lower inducer head means that the cavitation develops earlier in the impeller than it would in case of the inducer with higher head coefficient at the design conditions. A solution to this issue was found quite unexpectedly, as it sometimes happens in the world of inventions. During creation of the early version of the blade geometry in the Design Modeller the leading edge position was accidentally shifted upstream with respect to the baseline design. The Excel model uses baseline value to calculate blade angle distribution, so when the two models were connected the blade angles were mapped to a longer blade than it was anticipated. As a result the final blade angle distribution used for CFD simulations was modified. At the same time the shape of the leading edge (sweep angle, sweep radius) remained unchanged. This difference can be seen in the meridional profiles of two designs based on the same parameters, shown in Figure 5.9. Before this mistake was noticed, the performance of several designs was already evaluated. It turned out that the static head coefficient of such "class" of inducers is generally higher than for the originally intended inducers. It was decided to continue optimisation with this kind of design. At that time it was suspected that the improvement was achieved by lowering the blade angle and/or decreasing the slip angle. The optimisation strategy was the same as before. The sampling started with 40 samples and after the first optimisation the response surface was refined by reducing its size and adding ten more points. The increase of static head coefficient of the inducer can be seen when the results of the sampling, showed in Figure 5.10, is compared. The modified design can achieve higher or equal head coefficient than the baseline design, while the original design

is always worse. Slight improvement can be also seen in the cavitating head coefficient. The refined response surface shown in Figure 5.11

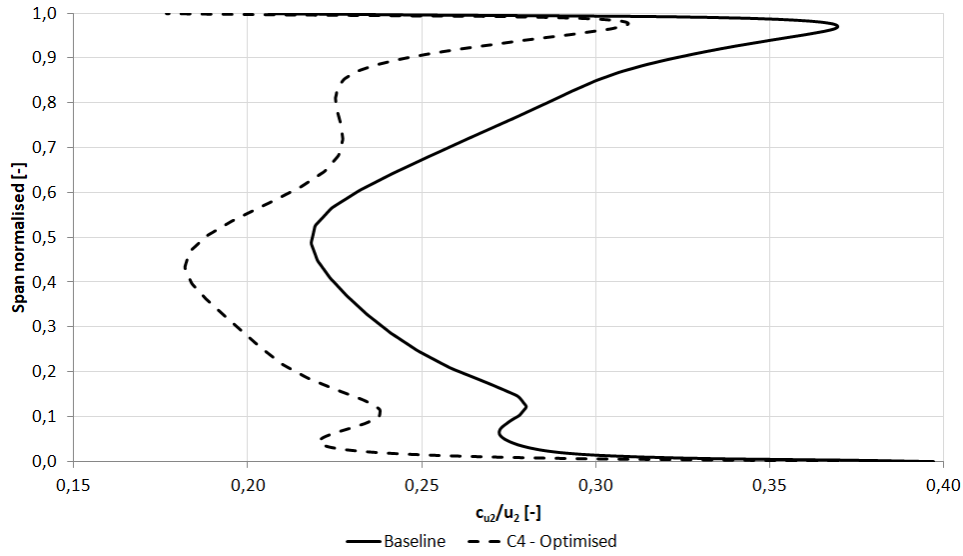


Figure 5.8: Comparison of the absolute circumferential velocity distribution at the outlet between the baseline and optimised inducer.

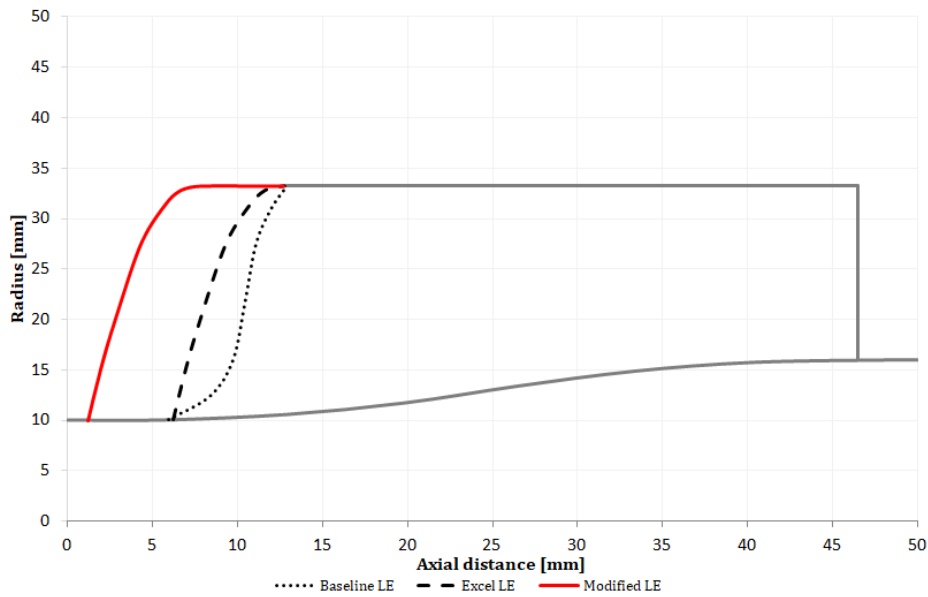


Figure 5.9: Position of the leading edge in the case of baseline, excel and modified design.

The shape of the response surface is similar to the previous one, with an expected maximum near the edge of the chosen design space. The maximal predicted cavitating head coefficient of the entire pump is slightly higher than previously. The optimised design was obtained with a NLQPL algorithm and its parameters are included in Table 5.8. Please note that due to the modified blade shape in Design Modeller, the values of incidence angle and solidity do not match with the actual simulated design. The solidity of the modified blade is higher and the incidence angle is not constant along the span. Nevertheless, the same parameters may still be used to generate distinguishable designs and produce an inducer with improved suction

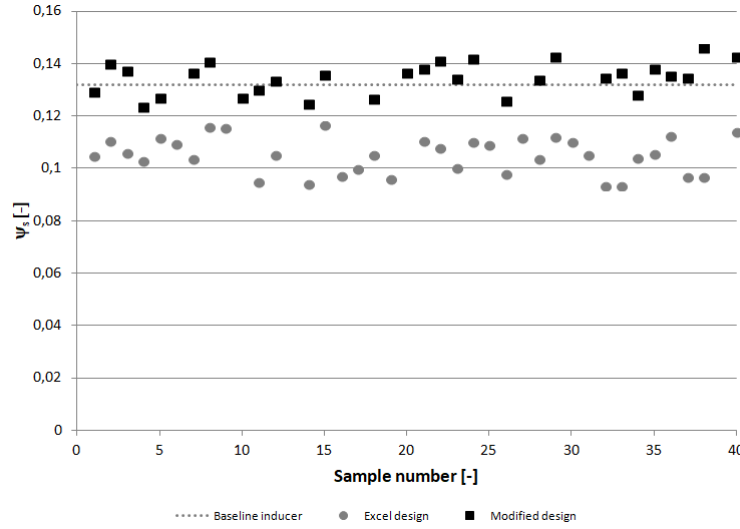


Figure 5.10: Wet head coefficient of the sampled inducers with the modified designs.

performance.

ID	Method	λ [°]	r_s [% span]	i [°]	s [-]
C5	NLQPL	40.7	64	2.5	1.79

Table 5.8: Parameters of the modified candidate design.

ID	$\psi_{w,pre}$ [-]	$\psi_{w,sim}$ [-]	Diff [%]	$\psi_{c,pre}$ [-]	$\psi_{c,sim}$ [-]	Diff [%]	η_{pre} [%]	η_{sim} [%]	Diff [%]
C5	0.515	0.515	0.0	0.513	0.512	0.2	84.6	84.6	0

Table 5.9: Comparison between the predicted and simulated performance of the modified candidate design.

The accuracy of the C5 performance prediction is similar as in the previous case - less than 1% difference. Therefore this response surface is also converged and the entire cavitating characteristic of the C5 design was simulated. Once again the entire cavitating characteristic was simulated in order to estimate the new critical cavitation number. Figure 5.12 shows the results of the simulations. As it was expected, higher static head coefficient of the second optimised inducer resulted in further improvement of suction performance. The critical cavitation number of the pump was decreased to 0.039 by 17.6% to with respect to the baseline design. This design was used during flow analysis to identify the reasons for performance change.

5.4. Simulation verification

The CFD simulations were verified by testing the baseline and optimised designs in Osaka Institute of Technology. The Fluidmachinery Laboratory of OIT is equipped with a closed-loop testing rig that allows to measure the static head coefficient of a pump with inducer at different flow coefficients and cavitation numbers. A scheme of the testing rig is presented in Figure 5.13.

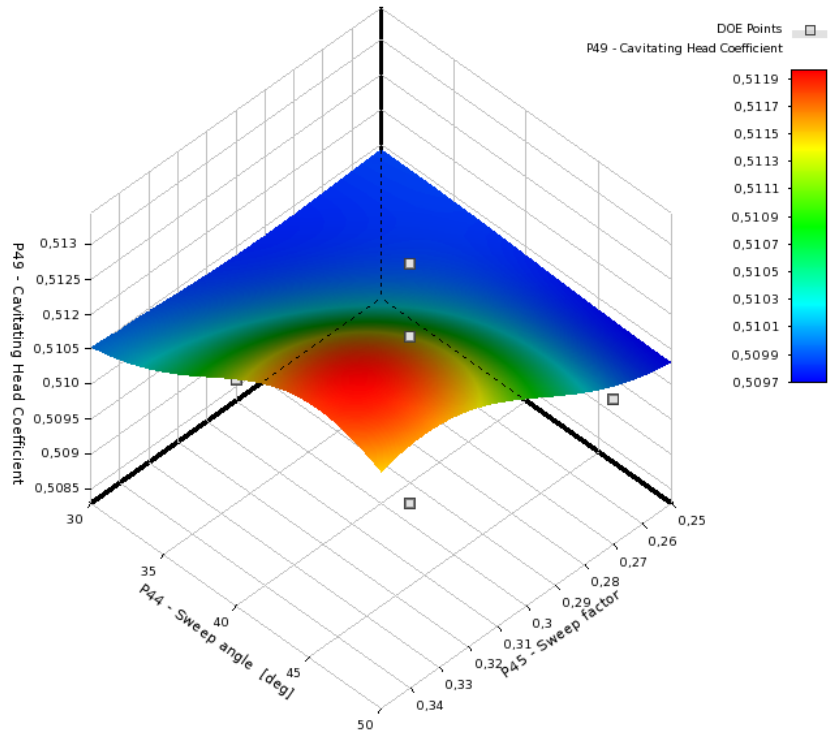


Figure 5.11: Response surface of the cavitating head coefficient based on sweep angle and radius.

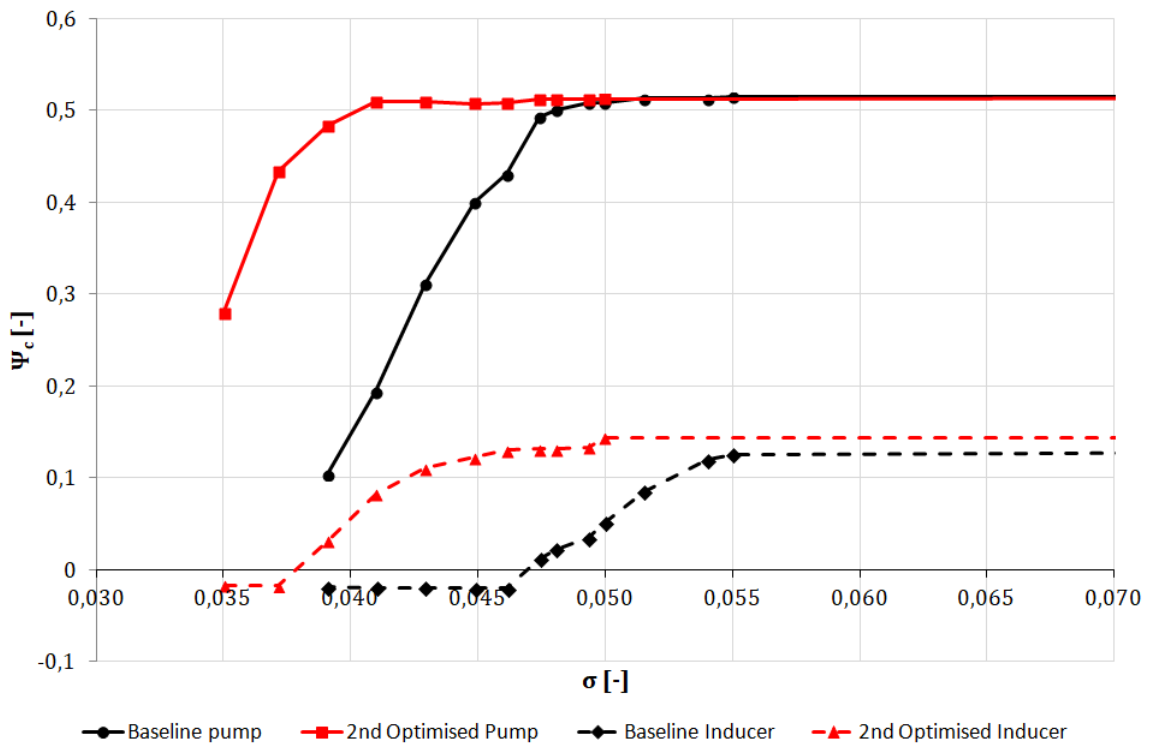


Figure 5.12: Comparison of the cavitating characteristic between the baseline and the modified optimised inducer

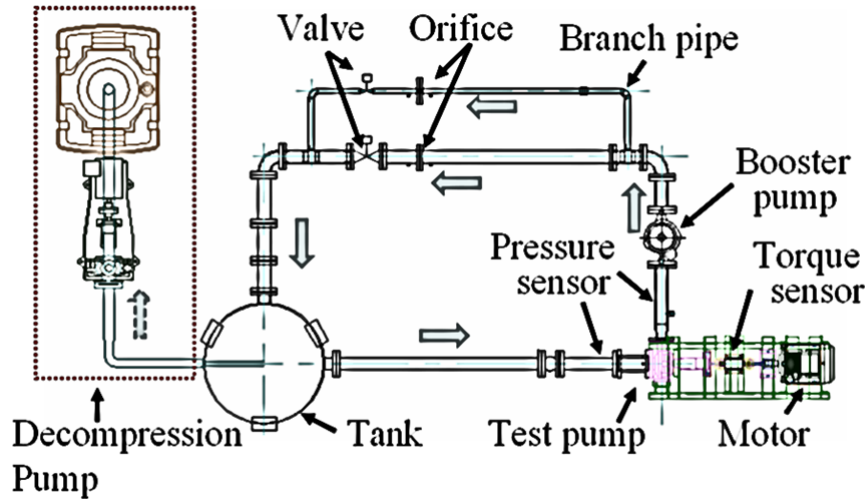


Figure 5.13: Test loop schematic.

The pump is driven by an electric motor running at a desired rotational speed. The shaft is connected to torque sensor that is used to calculate the efficiency of the pump. Head of the pump is measured by a differential pressure sensor connected to the inlet and outlet of the pump. At the inlet a second pressure sensor is connected which is measuring the absolute static pressure required to calculate the cavitation number during the test. The vapour pressure of the water is determined by measuring its temperature in the loop. The cavitation number is changed by reducing the static pressure inside a water tank. This is done with a vacuum pump connected to the top of the tank. Measurement of cavitating characteristic starts with adjusting the valve position to obtain required flow coefficient. Then the pump is turned on for an hour to deaerate the water inside the loop. During this process the pressure inside the tank is lowered by a vacuum pump to ensure that deaeration process is successful. The same vacuum pump is used to control the cavitation number during the test, that starts at high pressure and then the static pressure in the tank is gradually reduced. The data acquisition system is based on LabView software and is able to record pump head and inlet conditions. The samples are taken at a rate of 1kHz and then averaged over the time of one second to mitigate the scatter in the measurement, especially at the cavitation numbers near the critical cavitation number and sudden head breakdown. Table 5.10 provides basic capabilities of the test loop. More information about the hardware used in the test loop is given in Appendix B.

Property	Value
Max. rotational speed	4000 RPM
Electric motor power	5.5 kW
Max. flow rate	0.7 m ³ /min
Min. inlet pressure	4 kPa
Max. inducer diameter	67.5 mm
Max. impeller diameter	133 mm

Table 5.10: Closed-loop testing rig specifications.

It also important to understand how the pressure sensors were connected to the flow channel because their placement is important for the quality of the results. The inlet pressure was measured by a single pressure transducer attached to a tap placed on the bottom side of the inlet pipe. The tap was placed three pipe diameters upstream of the inducer. The same connection

point was shared by an analog pressure gauge and differential pressure sensor channel used to measure the head of a pump. The second channel was connected to the discharge pipe that connected a volute of the tested pump with the booster pump. A diagram showing the inlet pressure sensor mounting system is shown in Figure 5.14. This setup is far from ideal because the readings of only one sensor can be easily disturbed when cavitation occurs. It is one of the major factors contributing to measurement uncertainty.

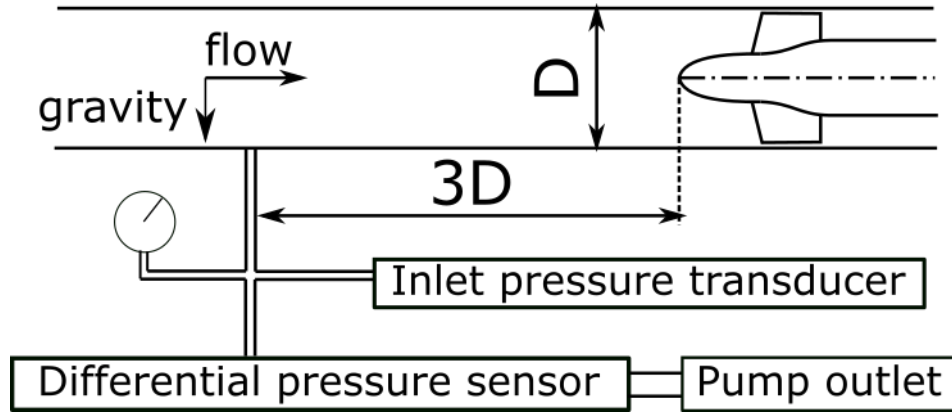


Figure 5.14: Inlet pressure measurement position.

The impeller and inducer were 3D printed in ABS plastic and polished to achieve smooth blade surface. Figure 5.15 shows the baseline inducer just after printing and the impeller already mounted on the shaft of the test stand. 3D printing process can be used to easily manufacture complex geometries in one piece. However, its accuracy is limited by minimal achievable width and height of one plastic layer extruded by the printer. Additionally the shape of the model can be affected by uneven layer cooling during printing. It is important to control the dimensions of a print to be sure that tested inducer matches the one that was simulated. In this case a layer width of 0.4mm and height of 0.1mm was used. 10 geometric parameters were chosen to be monitored. These include: leading and trailing edge thickness's at the hub and tip of the blade (4 parameters), tip and hub diameters at the leading and trailing edges and the diameters of the hub and tip (4 parameters) and finally the diameter of the shaft hole at the inlet and outlet (2 parameters). Figure 5.16 shows the placement of the measurement on the inducer model. These values were chosen before their either impact the suction performance (like blade thickness) or interface with the test rig (tip gap, shaft hole). They should also be the same in both optimised and baseline inducers. Each dimension was measured 5 times with a calliper. The results of the measurements of the baseline and optimised inducers are included in Table 5.11 and Table 5.12 respectively. The maximal difference between nominal and actual dimensions is 0.35mm, with the majority within 0.1mm. The print is generally smaller than the CAD model, what can be attributed to the shrinkage of the ABS as it cools down. The biggest difference (0.35mm) was found at the hub diameter at the inlet, but this is still below 1% of the nominal dimension. The tolerance on the LE/TE thickness is within 0.1mm (this corresponds to 7% at the LE, and 0.3% at TE). However, LE thickness was relatively hard to measure because of the curvature of the blade - it was hard to make a clear 'perpendicular' measurement. Most importantly, in both cases the leading edge is thicker than in the CAD model so that the influence of this dimension change should be similar. It was concluded that the quality of the prints is good enough for testing.

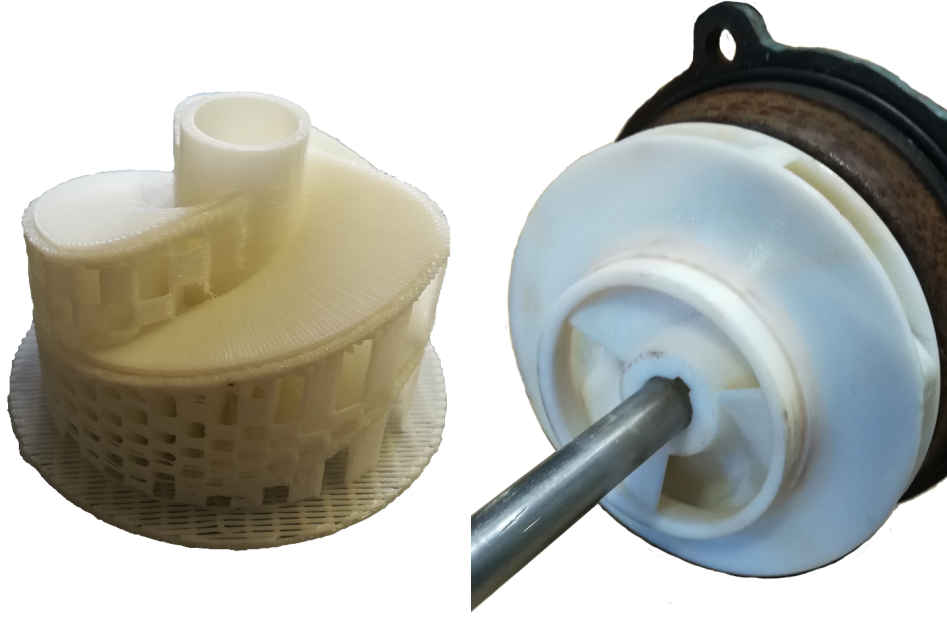


Figure 5.15: 3D printed inducer and impeller.

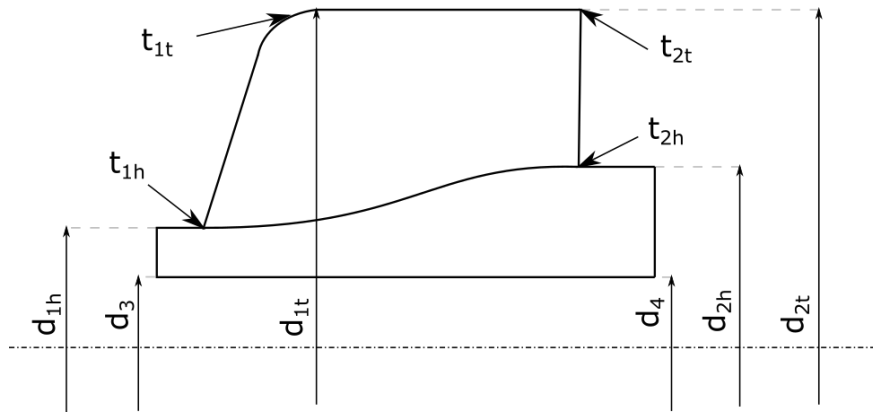


Figure 5.16: Dimensions measured to verify the accuracy of the 3D printing process.

Baseline										
Parameter	t_{1h}	t_{1t}	t_{2h}	t_{2t}	d_{1t}	d_{1h}	d_{2t}	d_{2h}	d_3	d_4
Base [mm]	0.90	0.90	2.60	2.60	66.50	20.00	66.50	32.00	16.20	16.20
M1 [mm]	0.95	0.95	2.65	2.55	66.60	19.65	66.55	31.80	16.15	16.25
M2 [mm]	1.00	0.95	2.60	2.50	66.55	19.70	66.45	32.10	16.10	16.15
M3 [mm]	1.00	1.00	2.65	2.50	66.45	20.00	66.40	31.95	16.20	16.10
M4 [mm]	0.95	1.00	2.65	2.55	66.50	20.05	66.60	31.80	16.10	16.25
M5 [mm]	1.00	0.95	2.60	2.60	66.65	19.70	66.50	31.90	16.25	16.25
Average [mm]	0.98	0.97	2.63	2.54	66.55	19.82	66.50	31.91	16.16	16.20
Max error [mm]	0.10	0.10	0.05	0.10	0.15	0.35	0.10	0.20	0.10	0.10
Std dev [-]	0.03	0.03	0.03	0.04	0.08	0.19	0.08	0.03	0.07	0.07

Table 5.11: Measurements of the dimensions of baseline inducer after 3D printing.

Optimised											
Parameter	t_{1h}	t_{1t}	t_{2h}	t_{2t}	d_{1t}	d_{1h}	d_{2t}	d_{2h}	d_3	d_4	
Base [mm]	0.90	0.90	2.60	2.60	66.50	20.00	66.50	32.00	16.20	16.20	
M1 [mm]	1.00	1.00	2.65	2.55	66.60	19.60	66.65	32.05	16.20	16.25	
M2 [mm]	1.00	1.00	2.55	2.60	66.50	19.80	66.35	31.90	16.15	16.15	
M3 [mm]	1.00	0.95	2.60	2.60	66.65	19.85	66.45	32.05	16.10	16.10	
M4 [mm]	0.95	0.95	2.55	2.65	66.45	19.80	66.40	31.85	16.10	16.25	
M5 [mm]	0.95	0.95	2.60	2.60	66.40	19.70	66.50	32.05	16.15	16.25	
Average [mm]	0.98	0.97	2.59	2.60	66.52	19.75	66.47	31.98	16.14	16.11	
Max error [mm]	0.10	0.10	0.05	0.05	0.15	0.40	0.15	0.15	0.10	0.15	
Std dev [-]	0.03	0.03	0.04	0.04	0.03	0.10	0.12	0.07	0.04	0.04	

Table 5.12: Measurements of the dimensions of optimised inducer after 3D printing.

During the tests both wet and cavitation performance was measured. Figure 5.17 shows the measured wet characteristic compared to the simulated results. As expected the simulations significantly overestimate the performance because the gap between the impeller and the casing is not modelled. Nevertheless, the offset between simulated and tested characteristics is almost constant in the simulated region what allows to correctly predict the slope of the $\phi - \psi$ curve. The difference between the baseline and optimised designs is negligible, because wet performance is determined by impeller which is the same in both cases.

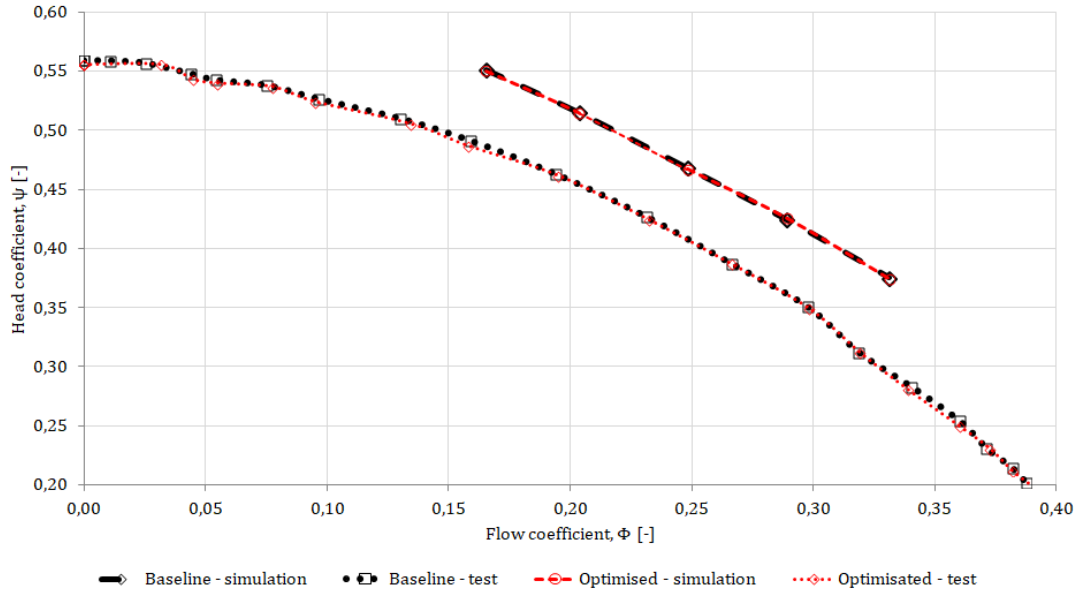


Figure 5.17: Simulated and measured wet characteristics of the baseline and optimised designs.

Efficiency measurements are shown in Figure 5.18. The results show that the efficiency reaches 69.1%, that is significantly lower than 84.6% predicted by the simulation. Once again this difference can mainly be attributed to lack of leakage flow around the impeller in the simulation. Similarly to the $\phi - \psi$ curve, the efficiency of both designs is almost the same. This confirms that the constraints imposed on the wet performance during optimisation process are fulfilled by the optimised design. Contrary to the wet performance, suction performance of optimised design is significantly different from the baseline performance. Figure 5.19 shows the results of suction performance measurements. Unfortunately, a large scatter exists in both data sets, what makes exact estimation of the critical cavitation number quite inaccurate. The measured

value for the baseline design ranges between 0.044 and 0.048 (0.047 predicted) and for the optimised design between 0.036 and 0.046 (0.039 predicted). In the best case scenario it would mean 25.6% decrease of the critical cavitation number and 5% increase in the worst case. This uncertainty is a result of flow rate oscillations present in the test loop as the head of the test pump decreases. A more powerful booster pump is likely to solve this problem, however it was not available during this project. Nevertheless, it is clear that the head drop occurs more slowly and the critical cavitation number is likely to be decreased even if exact improvement can not be determined.

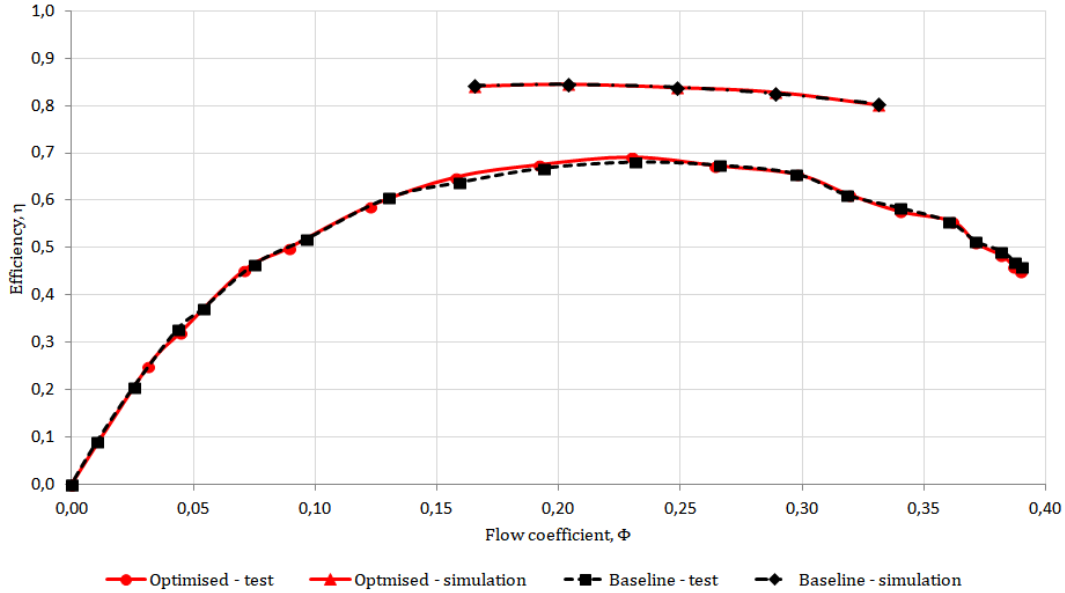


Figure 5.18: Simulated and measured efficiency of the baseline and optimised designs.

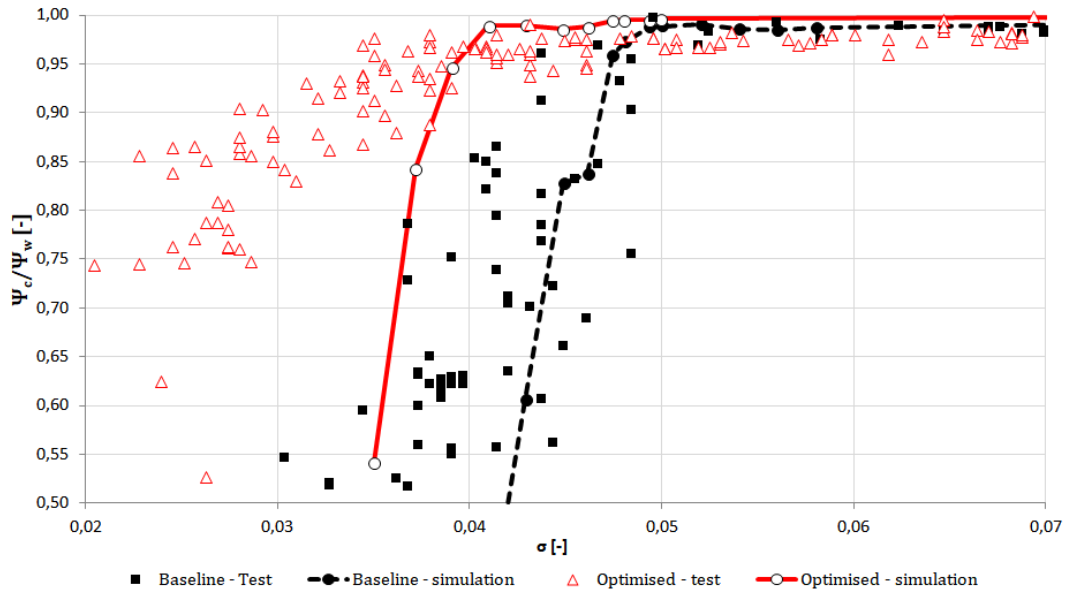


Figure 5.19: Simulated and measured cavitating characteristics of the baseline and optimised designs.

Performance improvement analysis

In the previous chapter the optimisation process was explained and the optimised design with an improved suction performance was chosen. In this chapter the baseline and optimised inducers are compared and the performance gain further investigated.

6.1. Geometry comparison

Geometry comparison starts from comparing the leading edge shape as seen from the front of the inducer and in the meridional view. Figure 6.1 shows that the sweep angle of the leading edge decreased, while the sweep radius and length of the blade both increased.

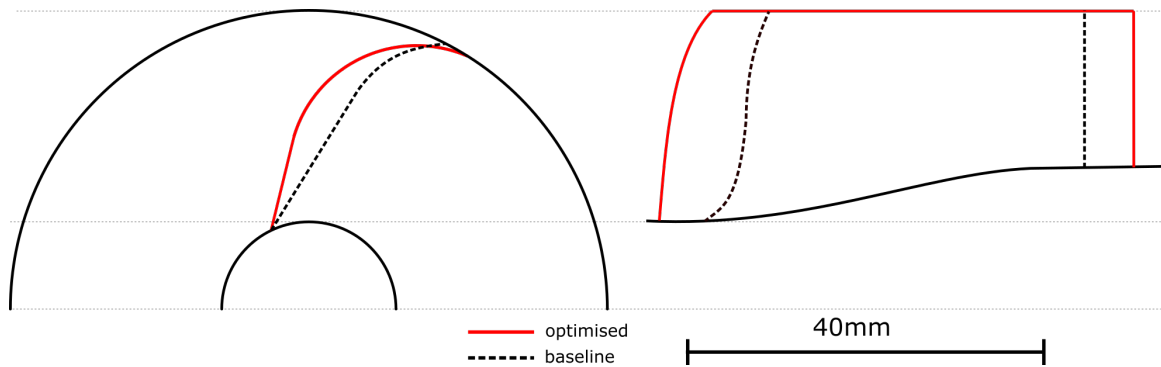


Figure 6.1: Comparison of leading edge and meridional shapes between the baseline and optimised design.

Although the original inducer was not designed according to the design approach used in this thesis, the shape of the leading edge and solidity may still be expressed using those parameters. The value of the solidity was recalculated, taking into account that the leading edge of the optimised design was moved upstream. Table 6.1 shows the exact comparison between the baseline and optimised designs. The biggest difference can be observed in the sweep radius, that is more than twice as big as in the baseline design. It was already noticed during sampling that the sweep radius has a big impact on suction performance and optimisation confirms that.

Parameter	Baseline	Optimised	Difference [%]
λ [°]	56.0	40.7	-27
r_s [% span]	26.0	64.0	+146
s [-]	1.45	1.90	+31

Table 6.1: Comparison of the parameters defining the baseline and optimised design.

The blade angle distribution also changed, what is shown in Figure 6.2. Although blade angles in the midspan and close to middle of the blade length are similar in both designs, changes can be observed at the leading and trailing edges. This change lead to change of incidence and outlet angles distribution along the span of the blade.

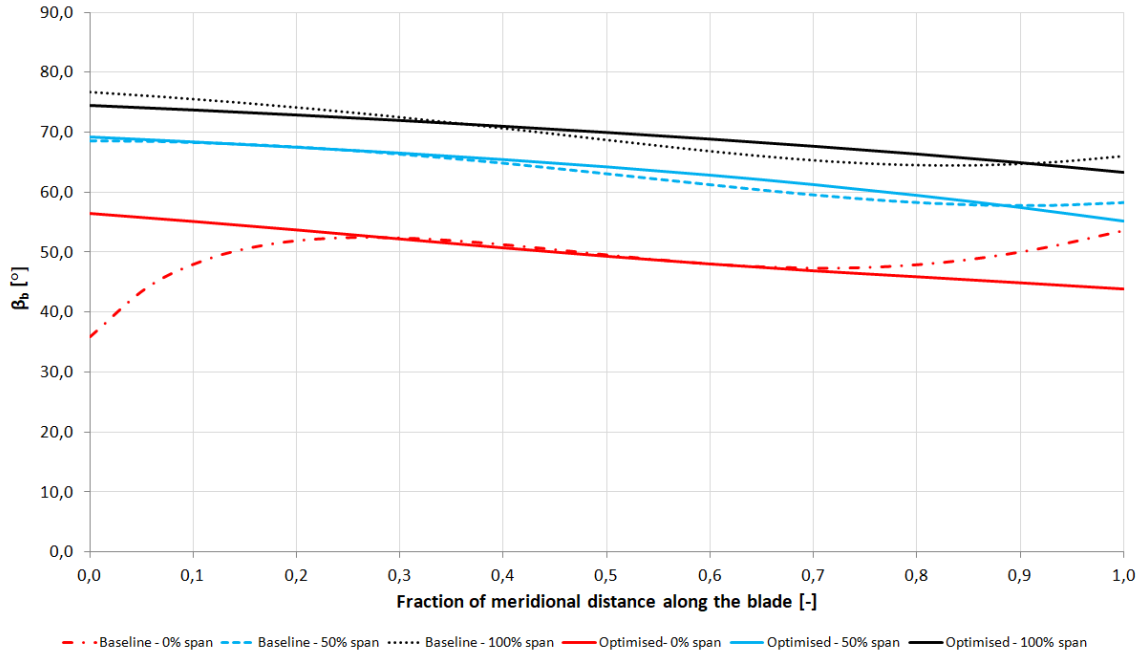
Figure 6.2: Comparison of the β blade angle distribution between the baseline and optimised design.

Figure 6.3a shows the distributions of incidence angle of the leading edge and the absolute circumferential velocity at the outlet of the blade. The incidence angle distribution changed significantly, especially near the hub where the excess incidence angle decreased to from 20° to 0.5°. At the tip the opposite happens - the incidence angle increased from 2.1° to 3.7°. The blade angle at the outlet decreased along the entire span of the trailing edge. Figure 6.3b shows the blade angle distribution at the outlet together with the resulting flow angle distribution. It can be noticed that not only the blade angle, but also the slip angle, was reduced. The decrease of slip angle and decrease of blade angle lead to increase of absolute circumferential velocity what can be seen Figure 6.4. This change explains the increase of static head coefficient, that is determined by the change in circumferential velocity between the inlet and outlet of the inducer.

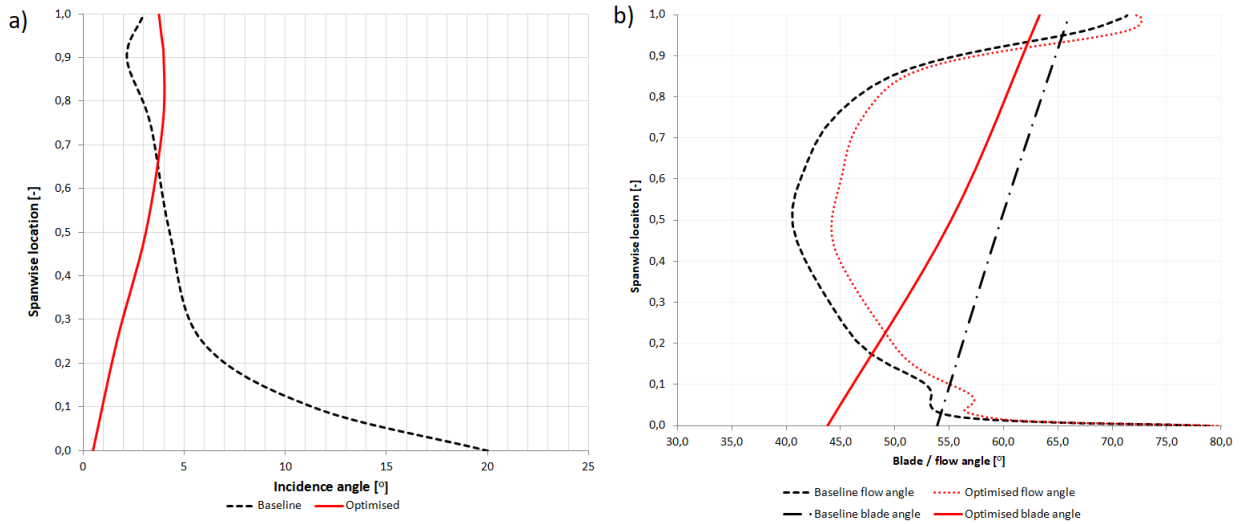


Figure 6.3: Comparison of: a) incidence angle b) outlet angle, between the baseline and optimised design.

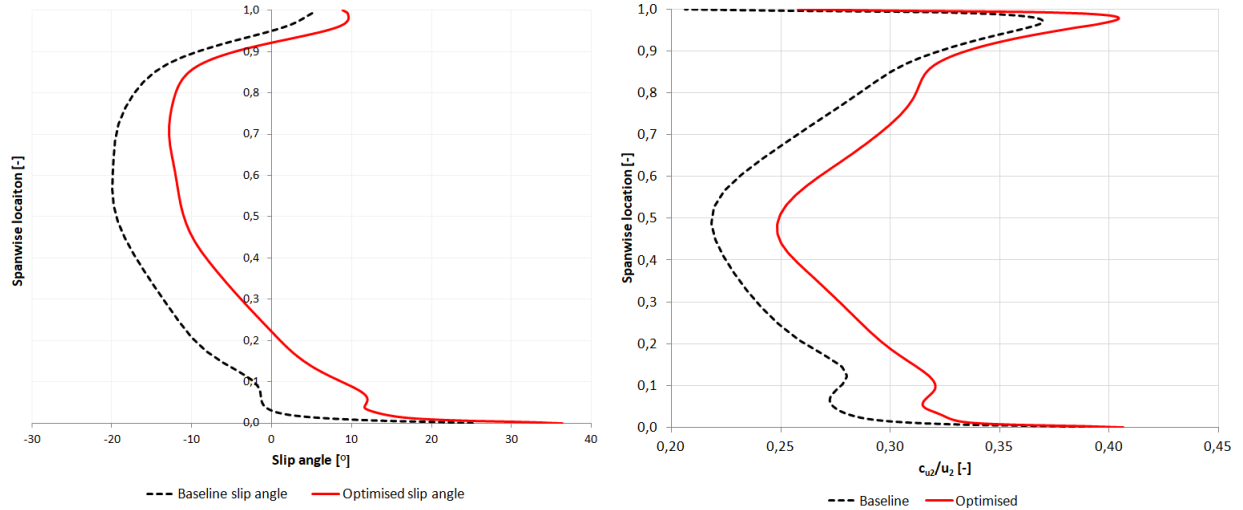


Figure 6.4: Comparison of: a) slip angle b) absolute circumferential velocity at the outlet of the inducer, between the baseline and optimised design.

6.2. Inducer suction performance analysis

As a result of the optimisation the critical cavitation number of the entire pump was decreased by 17.6% according to CFD simulations. The improvement is caused by the improved suction performance of the inducer that is able to maintain its head at lower cavitation numbers. Figure 6.5 shows exactly how the static head coefficient is decreasing for both inducers with decreasing cavitation number. At cavitation number $\sigma = 0.055$ a sudden breakdown occurs for the baseline inducer, while the head of the optimised inducer remains above 90% of the wet value until $\sigma = 0.047$. As a result the static pressure at the inlet of the impeller is higher at lower inducer cavitation numbers and cavitation in the impeller is suppressed. This relationship can be expressed by plotting the cavitation number based on the impeller inlet conditions as a function of inducer cavitation number, as shown in Figure 6.6. As the inducer cavitation

number decreases, the impeller cavitation number also decreases and when the head of the inducer is close to 0 both cavitation numbers are almost equal. Line $y = x$ that corresponds to equal cavitation numbers is provided for reference.

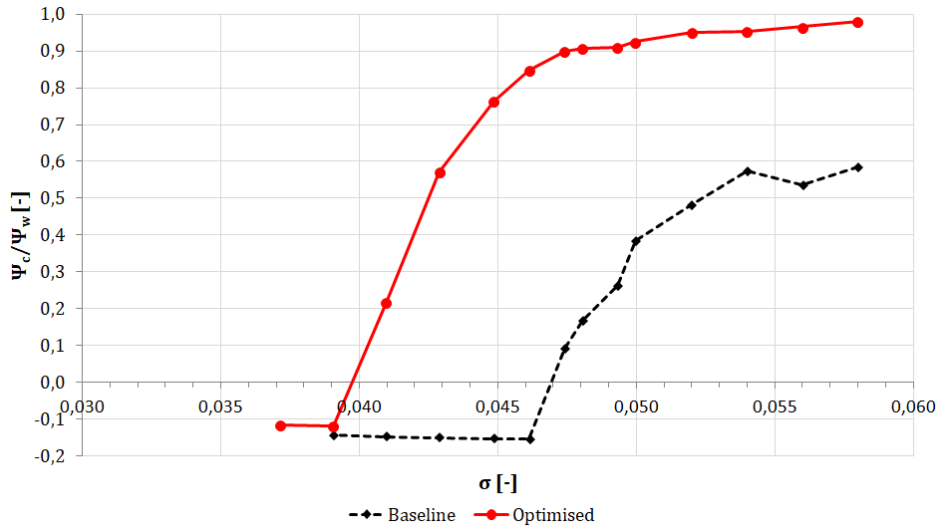


Figure 6.5: Simulated cavitating characteristic of baseline and optimised design.

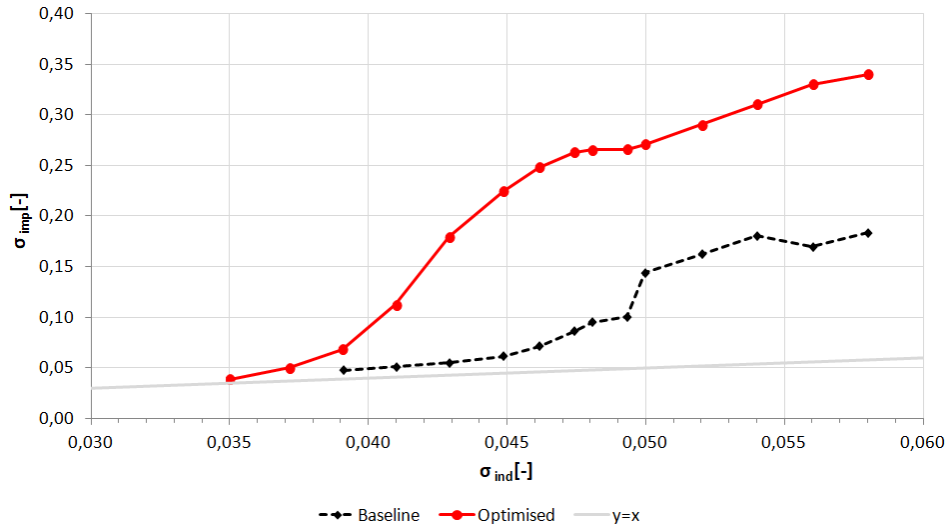


Figure 6.6: Impeller cavitation number as a function of inducer cavitation number for baseline and optimised design.

This clear improvement of suction performance of the optimised inducer is caused by decreased vapour volume in the flow channel. In order to compare two designs the absolute vapour volume V_{va} must be related to the entire volume of the flow channel V_{fc} , what allows to tell how much blockage is created by the vapour. Figure 6.7 how percentage of the entire flow channel volume taken by vapour changes with decreasing cavitation number for both designs. There is much less vapour being created in the optimised case what directly influences the suction performance. Additionally, the optimised design performs better even if compared at the same vapour volume percentage. Figure 6.8 shows the relationship between amount of

vapour in the flow channel and the head coefficient of the pump. It shows that not only the vapour volume is reduced but also that the inducer can operate with higher percentage of the vapour within the flow channel.

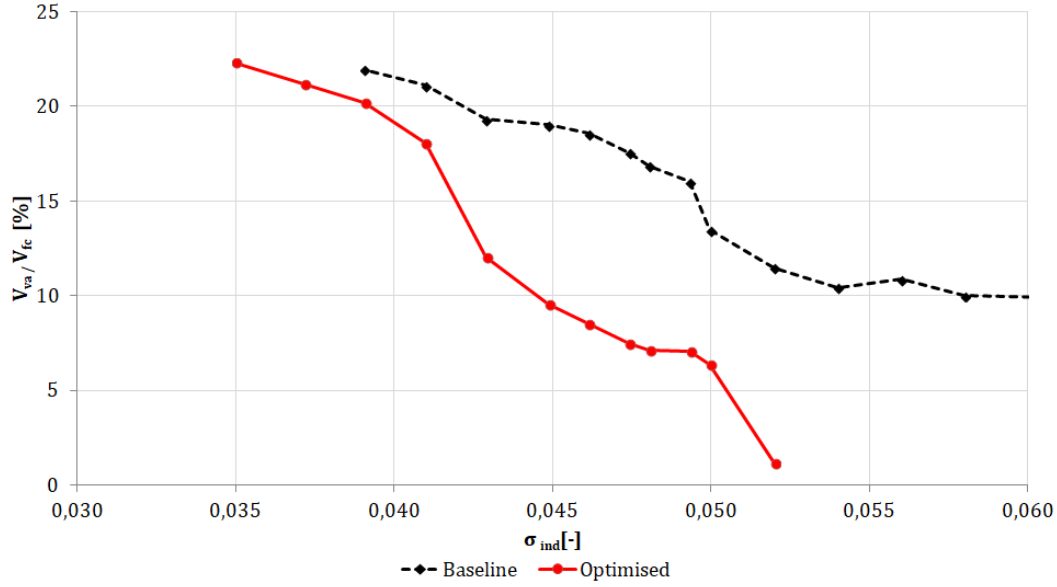


Figure 6.7: Percentage of vapour volume in the flow channel a function of inducer cavitation number for baseline and optimised design.

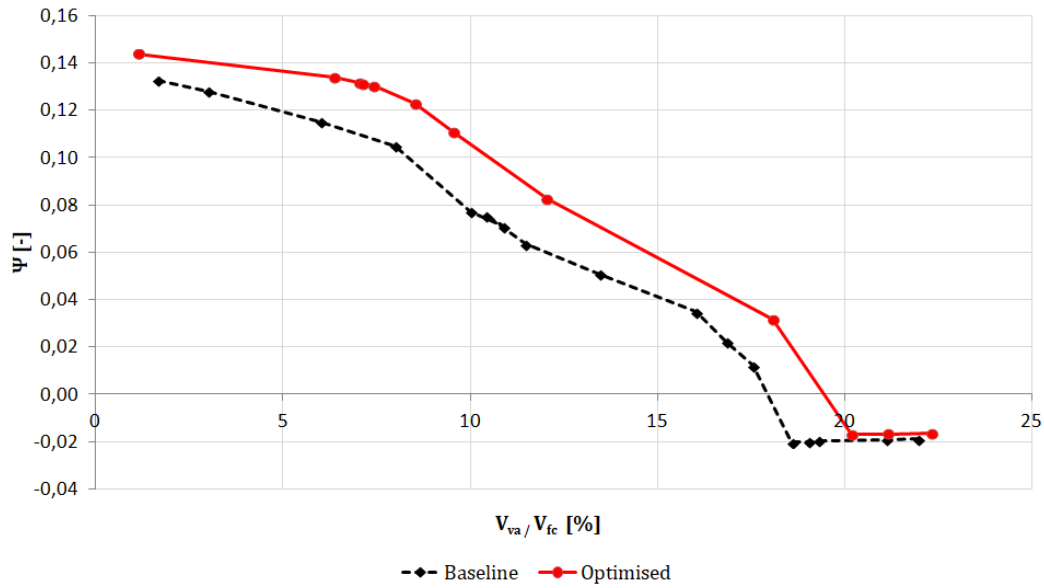


Figure 6.8: Inducer head coefficient as a function of percentage of vapour volume in the flow channel for baseline and optimised design.

Examining the distribution of vapour in the flow channel at different cavitation numbers gives a first indication of the reason for performance improvement. Figure 6.9 shows the isosurfaces of vapour volume fraction equal to 10% for both inducers at two cavitation numbers $\sigma = 0.111$ and $\sigma = 0.050$. The absolute length of the region influenced by the cavity is similar for both

designs at both cavitation numbers. However, in the case of the baseline inducer the cavity at $\sigma = 0.050$ is already extending past the trailing edge. This is not the case for the optimised inducer with longer blade. In addition, in the baseline inducer the vapour is already blocking the entire flow channel at $\sigma = 0.111$, while in the optimise case there is still a region free of cavitation. The reason for reduction of vapour volume can be found by looking at total pressure distribution along the inducer, which is a measure of energy transfer between the blades and the flow. To calculate its distribution, total pressure is averaged by mass at several cross sections with constant streamwise location. Figure 6.10 shows the difference between the average total pressure at a given location and the inlet total pressure in wet conditions and at a cavitation number $\sigma = 0.050$. The difference is scaled by the value of the inlet total pressure in order to make the comparison easier. The total pressure rise is higher for the optimised design along the entire blade. Higher average total pressure near the leading edge effectively leads to higher static pressure and lower vapour volume. When cavitation occurs the energy transfer at the front of the inducer it influenced first and the majority of the pressure rise must be generated at the back of the inducer.

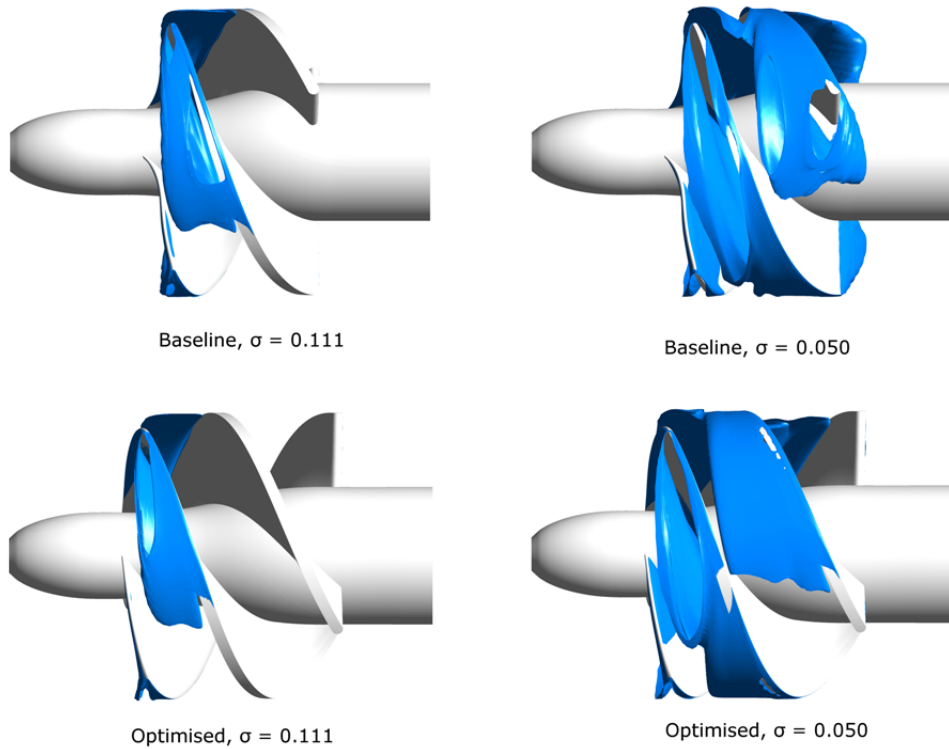


Figure 6.9: Isosurfaces of vapour volume fraction equal to 10% at two cavitation numbers: 0.111 and 0.050 for baseline and optimised design.

Even more insight into the performance of the inducer with and without cavitation can be gained by looking at blade loading distribution of a blade. Blade loading represents the energy transferred through the blades to the fluid in terms of force exerted by the blades on the fluid. This force results in the pressure difference between the suction and the pressure side of the blade. The same pressure difference may be associated with the change of the circumferential velocity of the flow along the meridional length of the blade. The pressure difference might be presented in the absolute units (Pa, bar etc.) but usually a dimensionless pressure coefficient

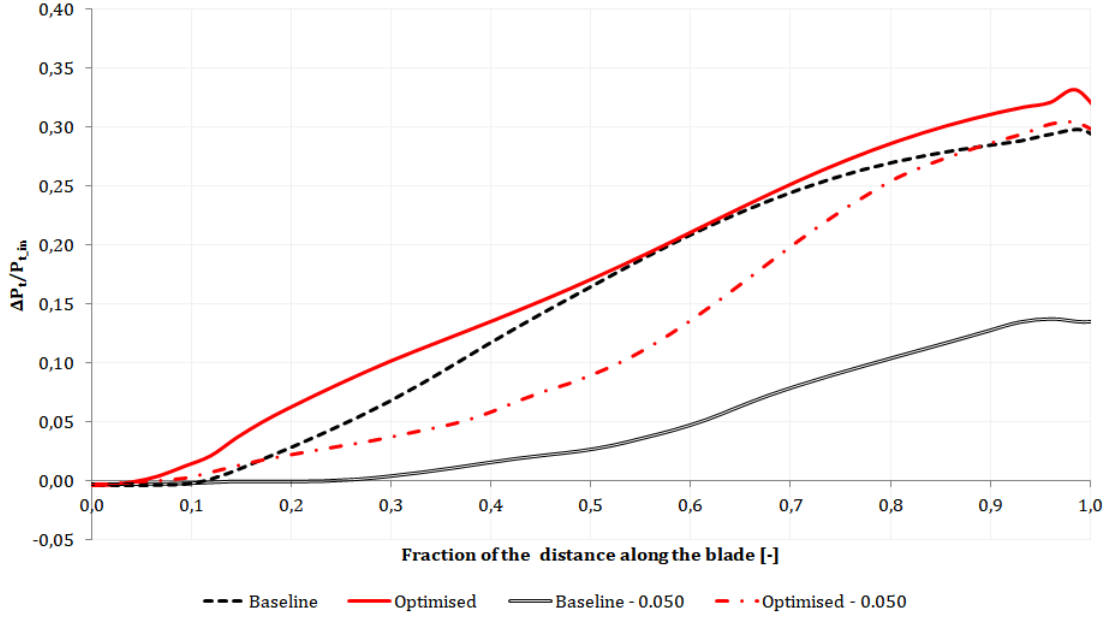


Figure 6.10: Total pressure rise distribution along the inducer blade without and with cavitation for the baseline and optimised design.

C_p is used:

$$C_p = \frac{p - p_1}{0.5\rho U^2} \quad (6.1)$$

where p is the static pressure in the given location, p_1 is the inlet static pressure, ρ is the density of the fluid and U is the reference velocity (usually blade velocity). The blade loading usually is presented as a plot of pressure coefficient along the length of blade at both sides of the blade (pressure and suction side). Figure 6.11 shows the pressure coefficient distribution in the wet conditions at 95% of the span of the blade, which is the region near the tip where cavitation develops fastest. It shows that static pressure on the suction side of the optimised inducer is higher or equal from around 5% of the edge length. The region influenced by high pressure drop near the leading edge is larger in the optimised case, but the minimal value of the static pressure remains higher. It is also worth noticing that the loading of the optimised blade is lower in its first half as the difference between suction and pressure side is lower.

Figure 6.12 shows blade loading distribution at the same location but at $\sigma = 0.050$. In the region influenced by cavitation the static pressure remains constant what confirms that entire length of the baseline blade is covered in vapour. In the optimised case the vapour ends at 70% of the blade length. Both blade loadings distribution show that the minimal static pressure occurs at the leading edge. This minimal value can be found at several spanwise locations to obtain its distribution along the span of the leading edge. Figure 6.13 shows such distributions for baseline and optimised designs. As expected the pressure is initially decreasing with increasing span due to increasing blade circumferential speed. In the case of the baseline inducer this trend continues until the end the blade. However, in the case of the the optimised inducer the minimal pressure starts increasing near 90% of the span. This phenomena has a great impact on the suction performance of the inducer, because the vapour starts forming near the tip of the blade. Increasing static pressure in this area delays cavitation development. This change may be attributed to the higher high sweep radius.

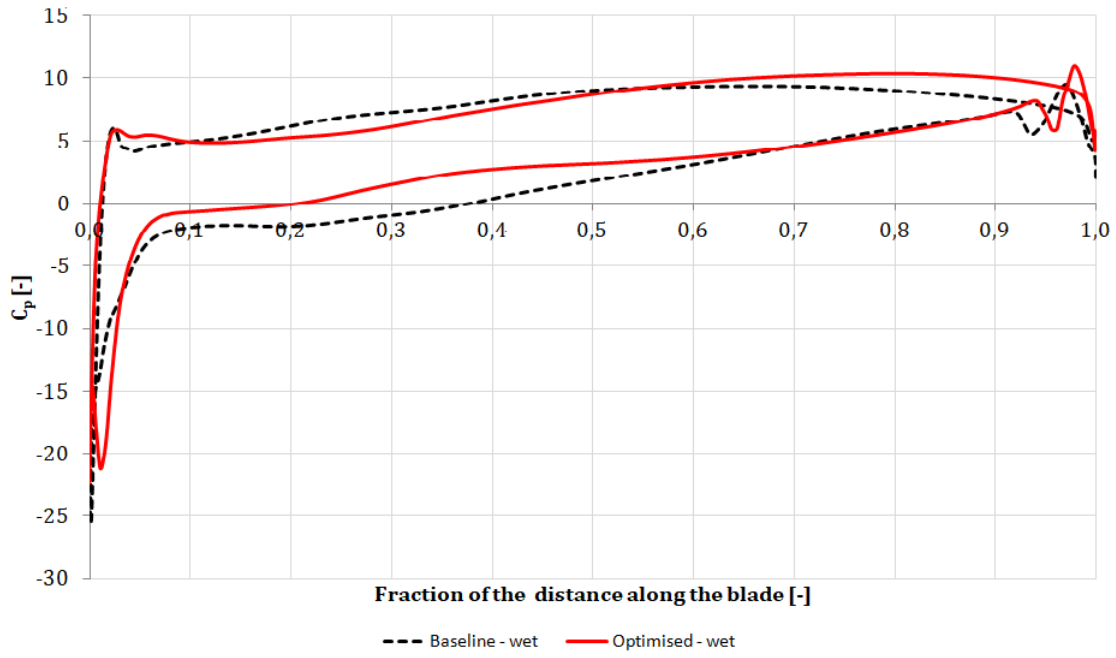


Figure 6.11: Blade loading distribution without cavitation at 95% of span for the baseline and optimised design.

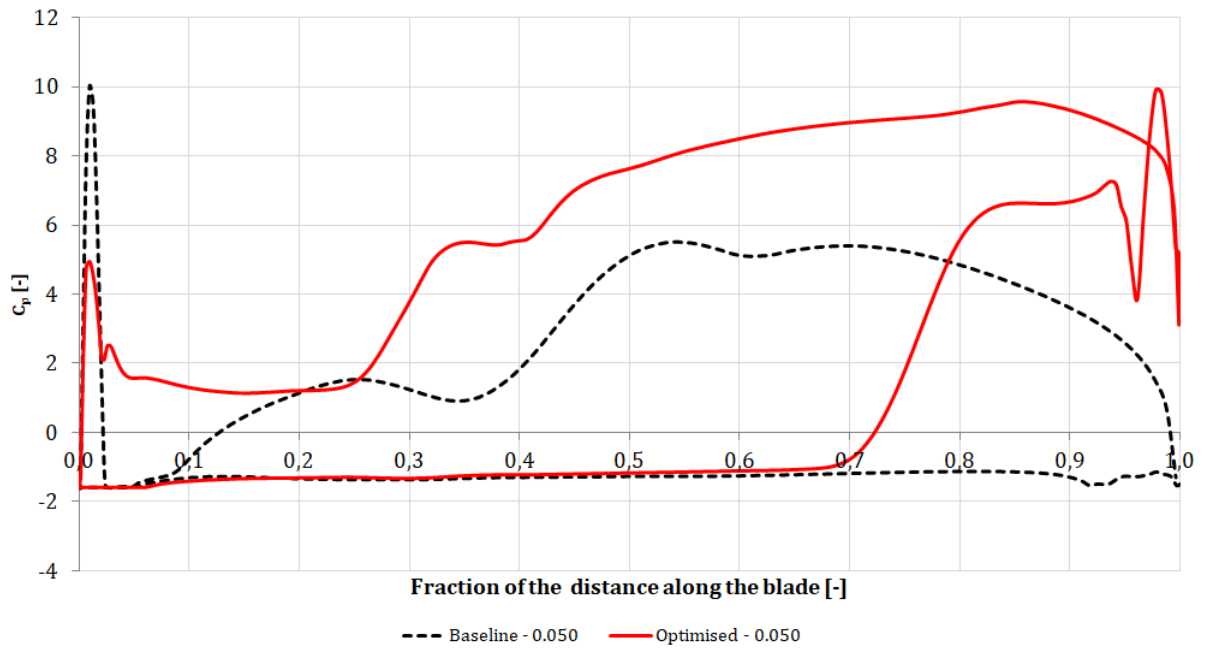


Figure 6.12: Blade loading distribution at $\sigma = 0.050$ at 95% of span for the baseline and optimised design.

In order to confirm this relationship two additional designs were generated: one with low and one with high sweep radius. The rest of the parameters remained the same, as shown in Table 6.2. The same table also contains the head coefficients calculated at wet and cavitating conditions. The decrease of sweep radius lead to a slight decrease of wet head coefficient and

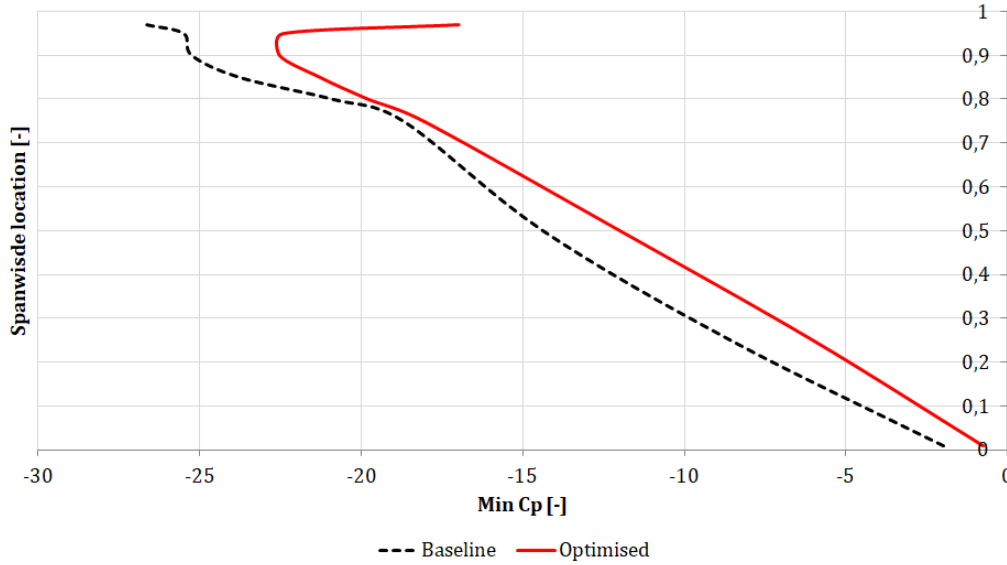


Figure 6.13: The distribution of minimal pressure coefficient along the leading edge span for the baseline and optimised design.

huge drop of cavitating head coefficient. The plot of minimal pressure coefficient along the span of leading edge reveals similar shape to the one presented in the case of baseline and optimised designs, as shown in Figure 6.14. Additionally it shows that the sweep and incidence angles have influence on the pressure drop near the hub of the inducer. When they are the same there is no difference in minimal pressure below the rounded part of the leading edge.

Parameter	Low sweep design	High sweep design
r_s [% span]	20	64
λ [°]	40.7	
s [-]	1.90	
i [°]	2.4	
ψ_w	0.136	0.146
$\psi_{c-0.047}$	-0.023	0.124

Table 6.2: Parameters defining high and low sweep designs and simulated performance of these designs.

The highest difference between the designs occurs around 75% of the span. Investigation of the flow in this area revealed that the high sweep radius introduces a region of higher radial velocity which is absent in the low sweep case, what is presented in Figure 6.15. As a result the fluid does not only move around the leading edge but is also displaced radially. Figure 6.16 shows the resulting velocity in the relative reference frame. Both velocities are shown in nondimensional form created by dividing the actual value of velocity by the tip speed u_t . In the high sweep case the region of higher velocity is smaller what reduces the region of low pressure. Figure 6.17 shows the distribution of the pressure coefficient which agrees well with the changed distribution of relative velocity. In the region of higher relative velocity static pressure decreases. The size of this region is effectively decreased in the high sweep case.

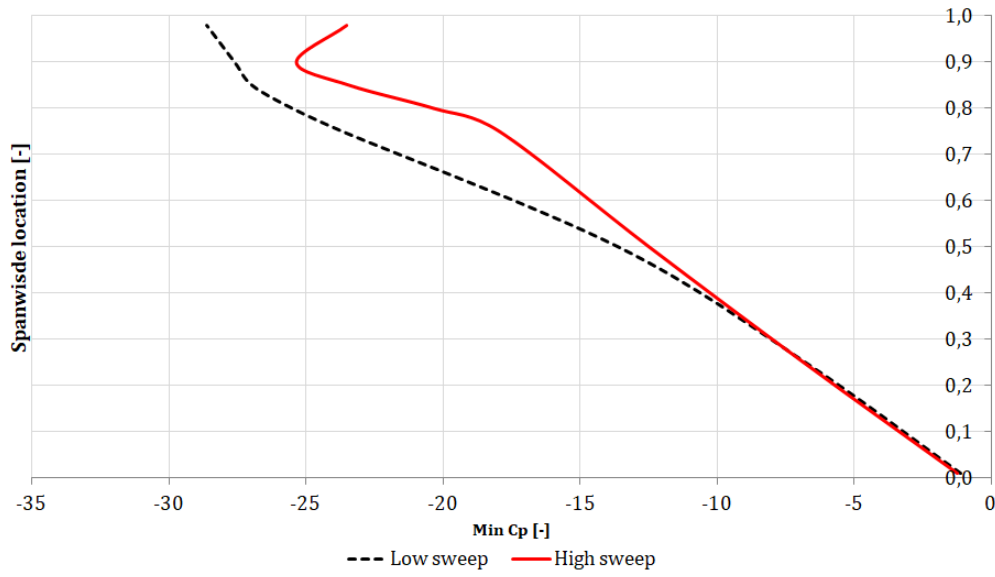


Figure 6.14: The distribution of minimal pressure coefficient along the leading edge span for the high and low sweep design.

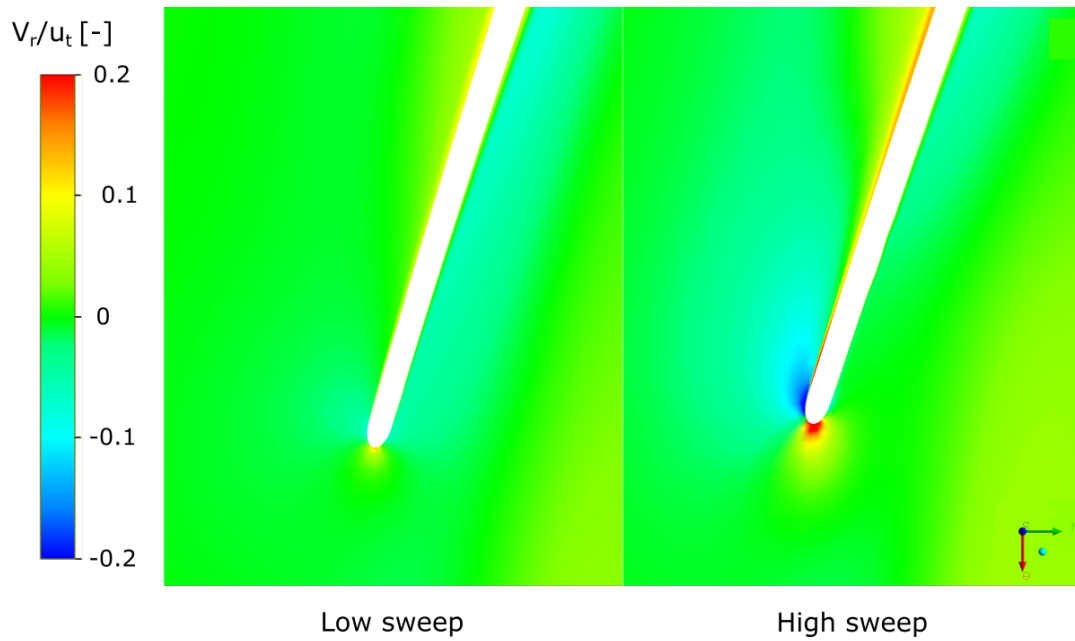


Figure 6.15: Comparison of radial velocity distribution V_r at 75% of the span around the leading in blade-to-blade view.

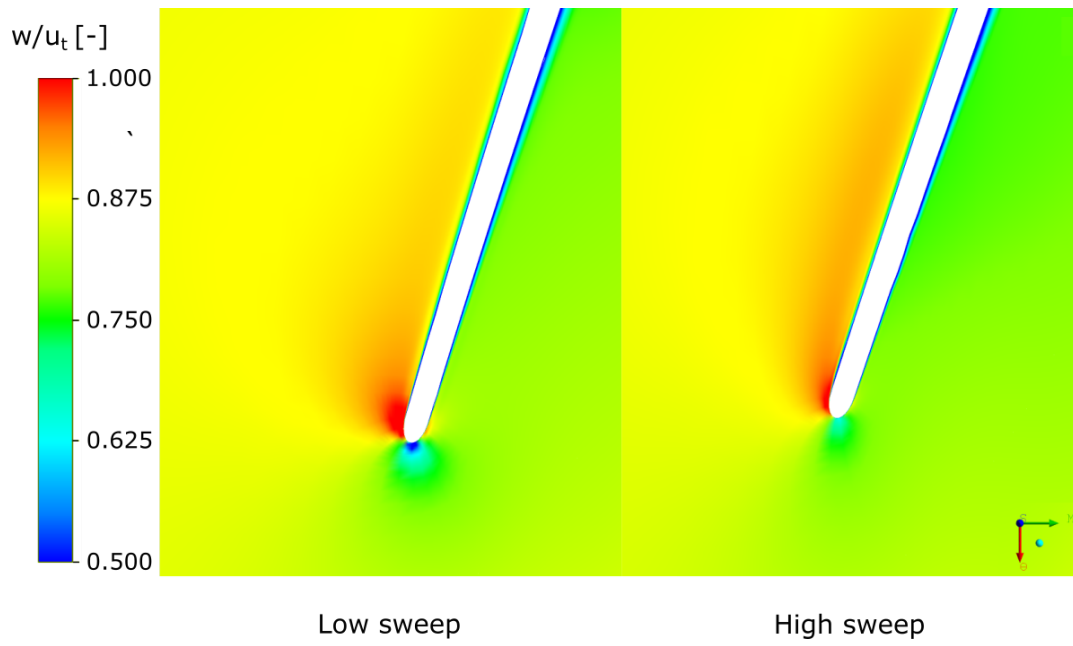


Figure 6.16: Comparison of relative velocity distribution w at 75% of the span around the leading in blade-to-blade view.

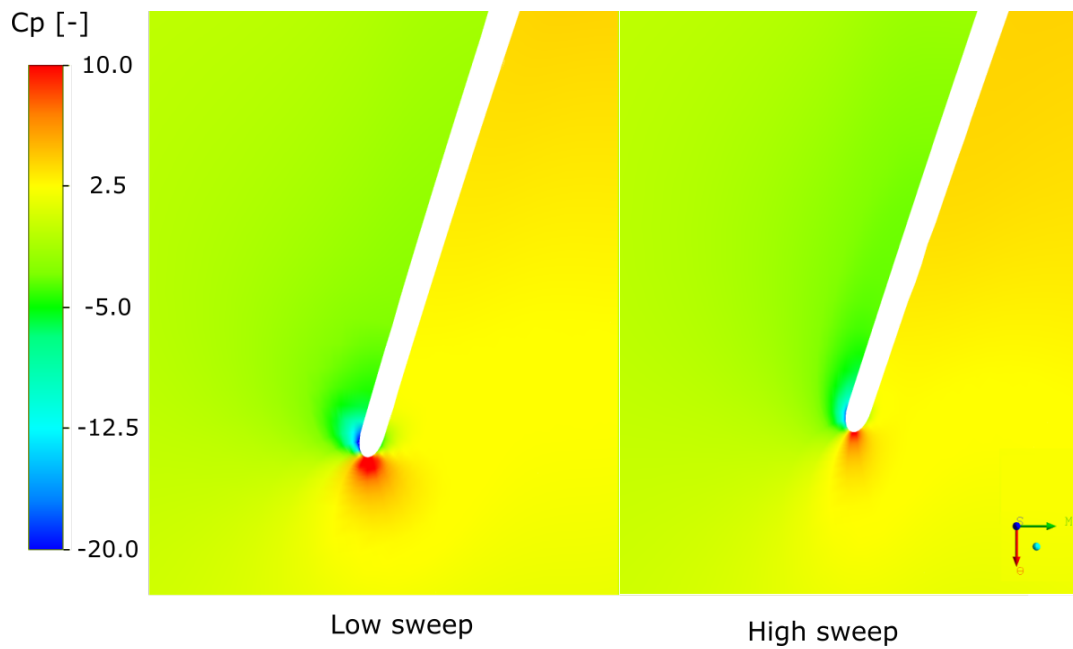


Figure 6.17: Comparison of pressure coefficient C_p distribution at 75% of the span around the leading in blade-to-blade view.

Conclusions and recommendations

7.1. Conclusions

The main goal of this thesis was to identify the key geometrical features of an inducer blade that lead to the improvement of the suction performance of the entire pump. In order to achieve this goal an optimisation framework was built which uses CFD simulations to predict the influence of selected inducer parameters on cavitation development inside the pump. The geometry of the optimised inducer is controlled by four parameters that define the design space during optimisation. The rest of the pump design is based on the baseline pump that was a starting point of the entire optimisation process. The performance of this pump was also used as a reference point to characterise the achieved improvement. The optimisation results are used to answer the research questions stated in the Introduction and form final conclusions of this thesis.

How big improvement of suction performance can be achieved by optimising the shape of the inducer blades?

The optimisation of the inducer blade controlled by four parameters (sweep angle, sweep radius, solidity and incidence angle) leads to a decrease of the critical cavitation number of the entire pump from 0.0473 to 0.0391, according to CFD simulations. This 17.6% decrease of the critical cavitation number means that the rotational speed of the optimised design can be raised by 10% at the same value of inlet pressure and still achieve the same pressure increase as in the baseline design. To verify this result the baseline and optimised designs were 3D printed and tested at the Osaka Institute of Technology. The tests confirmed that the head of the pump remains higher at lower cavitation numbers. An exact determination of the critical cavitation number was not possible due to the large scatter in the test data.

What blade shape gives the improved suction performance?

The optimised blade is characterised by four parameters: sweep angle, sweep radius, incidence angle and blade solidity at the tip. The sweep radius proved to be the most critical parameter and it changed most, increasing by 146% with respect to the baseline design. The sweep angle, the second parameter controlling leading edge shape, the sweep angle decreased by 27%. The length of the blade increased resulting in 31% increase of solidity. The main changes in the incidence angle distribution is the reduction of excessive incidence at the hub and increased incidence at the tip - from 3° to 3.8°.

Why the optimised blades improved the suction performance?

The improvement of suction performance is caused primarily by a decrease of vapour volume in the inducer flow channel. Additionally the optimised inducer has a higher wet head coefficient due to the change of the outlet angle. This means that a higher drop of performance due to cavitation is required before the cavitation will develop in the impeller. Improved vapour handling can be connected with an increased length of the blade that is less affected than the short blade by the cavity growing from the leading edge. The reduction of vapour volume is achieved by increasing the static pressure at the suction side of the blade and minimising the static pressure drop at the leading edge. This drop is decreased due to a high sweep radius which reduces the excess velocity around the leading edge by allowing the fluid to move radially.

What design guidelines can be formulated regarding the shape of inducer blades for suction performance improvement?

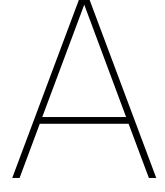
The results of the optimisation process showed that the shape and the position of the leading edge tip are the most crucial parameters when the highest suction performance is required. By rounding the tip and moving it downstream the critical cavitation number of the inducer and the entire pump can be significantly reduced. The recommended value of the sweep radius is at least 50-60% of the leading edge span. Higher values are also likely to further increase the suction performance, however it may come at a price of reduced efficiency as it was indicated by the response surface. The angle at which the leading edge connects to the hub is less important, with the optimal value ranging from 30° to 40°. Increase of suction performance can also be achieved by increasing the length of the blade to achieve optimal blade solidity at the tip that ranges from 1.8 to 1.9. Less clear conclusions can be made about the incidence angle. Higher values (2°-3°) increase slightly the head of the inducer without cavitation but lower values are proffered (1°-2°) for improved suction performance.

7.2. Recommendation for future work

The results obtained with the optimisation framework created during this project proved that it is capable of delivering a design with the desired performance. As always, several steps may be made to either further improve the suction performance of the pump or to adopt the presented approach to reach other similar goals. To begin with, the initial blade angle distribution used in the Excel-based model resulted in lower head of the inducer. Changing it to the final version will give a better control over the inducer design and may give even further performance improvement. Additionally, the optimisation may be repeated with a higher number of parameters. Obvious candidates are the parameters controlling the meridional shape of the leading edge. In this thesis they were defined as a fixed function of the sweep angle and sweep radius. Treating them as individual parameters will help to understand better how leading edge shape influences cavitation development. It is also possible to make a joint inducer-impeller optimisation, however the exact set of parameters in this case is yet to be determined.

During this thesis the suction performance was investigated only at the design flow rate. This might not be enough for applications requiring variable flow rate from the pump. Therefore it may be beneficial to verify if the presented conclusions hold at other flow rates. Finally,

improvements can be made with respect to the accuracy of the simulations and testing. Firstly the scatter in the test data should be reduced as it makes the simulation verification very difficult. As mentioned earlier the scatter is likely to be caused by flow rate changes during cavitation characteristic measurements. This problem can be solved by adding a more powerful booster pump or active control system adjusting the flow rate automatically during the test. Additional computing power can be used to model the gap between the impeller shroud and the casing to able to predict pump head and efficiency more accurately.



Inducer design method

This appendix describes in detail how the blade angle distribution and meridional shape of the inducer were calculated during optimisation. The design process starts from calculating the θ_0 angle along the leading edge span from sweep angle λ and sweep radius r_s .

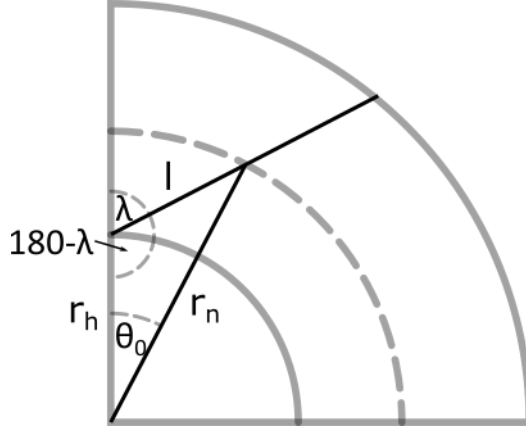


Figure A.1: Calculation of θ_0 angle from λ angle.

This angle can be calculated from the law of cosines used in a triangle visible in Figure A.1. First the length of l is calculated from the resulting quadratic equation:

$$r_n^2 = r_h^2 + l^2 + 2lr_h \cos(180^\circ - \lambda) \quad (\text{A.1})$$

Where r_n is the radius of the n-th layer for which θ_0 is calculated and r_h is the radius of the hub. Solving this equation gives the following result:

$$l = \frac{2r_h \cos(180^\circ - \lambda) + \sqrt{[2r_h \cos(180^\circ - \lambda)]^2 - 4(r_h^2 - r_n^2)}}{2} \quad (\text{A.2})$$

The cosine law may be used again to calculate θ_0 :

$$\theta_0 = \arccos \left(\frac{l^2 - r_h^2 - r_n^2}{-2r_h r_n} \right) \quad (\text{A.3})$$

This angle is calculated at 25, 50, 75, 90, 95, 97.5 and 100% of the leading edge span. Increasing resolution near the tip is required to accurately model the round part of the leading edge.

Calculation of the θ_{0r} angle for this round part of the leading edge starts from determining the centre of the circle. It is assumed that the round part of the leading edge is tangent both to the outer circle defining tip diameter and to the straight part of the leading edge, as shown in Figure A.2. The centre of this circle is located on a straight parallel to the straight defined by the first part of the leading edge. The distance between these straights is equal to r_s what allows to easily calculate the parameters of both straights.

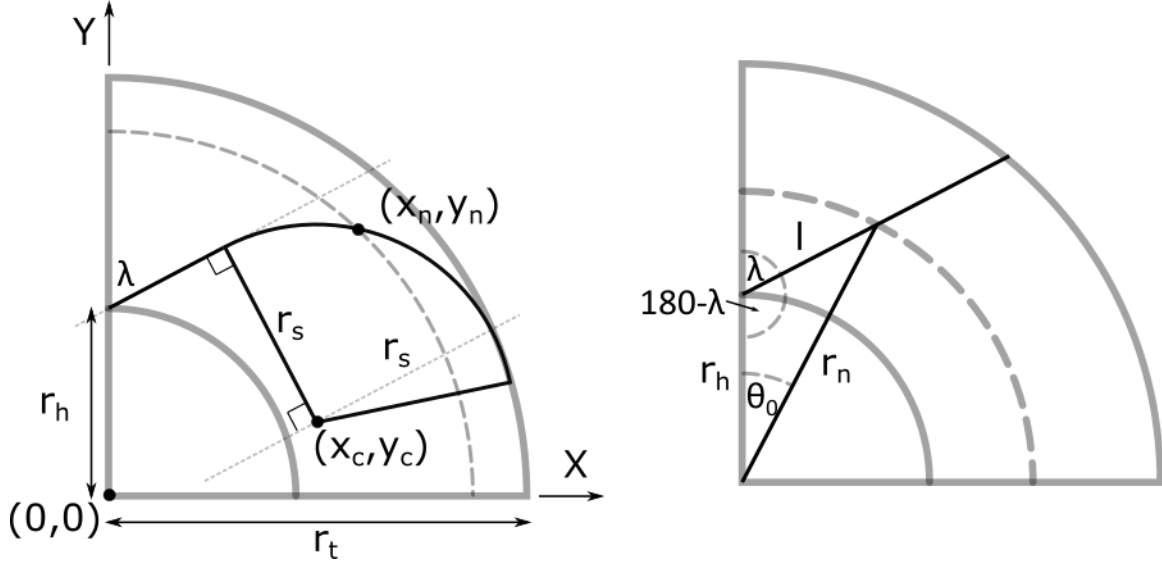


Figure A.2: Calculation of θ_0 angle from sweep radius r_s .

The axis of the inducer is taken as a (0,0) point. The equation of the line passing through the straight part of the leading edge is:

$$y = \tan(90^\circ - \lambda)x + r_h \quad (\text{A.4})$$

The second straight has the same slope defined by λ angle but is shifted down by Δb equal to:

$$\Delta b = \frac{r_s}{\sqrt{1 + \tan^2(90^\circ - \lambda)}} \quad (\text{A.5})$$

The centre of the circle is located on another circle, with a centre located in (0,0) point. The intersection point of the previously found straight and this circle is the centre point that is looked for. In order to find it a system of two equations must be solved:

$$\begin{aligned} y_c &= ax_c + b \\ r_c^2 &= x_c^2 + y_c^2 \end{aligned} \quad (\text{A.6})$$

where:

$$\begin{aligned} a &= \tan(90^\circ - \lambda) \\ b &= r_h - \Delta b \\ r_c &= r_t - r_s \end{aligned} \quad (\text{A.7})$$

x_c can be found from the resulting quadratic equation:

$$0 = (1 + a^2)x_c^2 + 2abx_c - r_c^2 + b^2 \quad (\text{A.8})$$

After solving:

$$x_c = \frac{-2ab + \sqrt{(2ab)^2 - 4(1+a^2)(b^2 - r_c^2)}}{2(1+a^2)} \quad (\text{A.9})$$

The y_c coordinate is then easily computed from the straight line equation. Now the (X,Y) coordinates of the round leading edge part may be found and corresponding θ_0 angles calculated. These points are located in the intersections between the leading edge circle and the circle defined by the given spanwise location. Once again this gives two equations:

$$\begin{aligned} (x_n - x_c)^2 + (y_n - y_c)^2 &= r_s^2 \\ x_n^2 + y_n^2 &= r_n^2 \end{aligned} \quad (\text{A.10})$$

Expanding the first equation and subtracting the second one from it gives a simpler relationship between x_n and y_n :

$$y_n = -\frac{1}{2y_c}(r_s^2 - r_n^2 - x_c^2 - y_c^2) - \frac{x_c}{y_c}x_n \quad (\text{A.11})$$

This equation describes a straight line $y_n = a_n x_n + b_n$ with a_n and b_n equal to:

$$\begin{aligned} a_n &= -\frac{x_c}{y_c} \\ b_n &= -\frac{1}{2y_c}(r_s^2 - r_n^2 - x_c^2 - y_c^2) \end{aligned} \quad (\text{A.12})$$

Coefficients a_n and b_n can be used to write a quadratic equation containing only x_n as an unknown:

$$0 = (1 + a_n^2)x_n^2 + 2a_nb_nx_n + b_n^2 - r_n^2 \quad (\text{A.13})$$

This structure of this equation is the same as in Equation A.8 and so is the solution:

$$x_n = \frac{-2a_nb_n - \sqrt{(2a_nb_n)^2 - 4(1+a_n^2)(b_n^2 - r_n^2)}}{2(1+a_n^2)} \quad (\text{A.14})$$

Now the y_n coordinate can be calculated from Equation A.11. When both x_n and y_n are known the θ_0 may be calculated:

$$\theta_0 = \text{atan}\left(\frac{x_n}{y_n}\right) \quad (\text{A.15})$$

Once again the θ_0 angle is calculated at 25, 50, 75, 90, 95, 97.5 and 100% of the leading edge span. Then it is decided which calculated value (straight or round) should be used for a given spanwise location. The decision is done by comparing the radius of the layer with the threshold established by the sweep radius. For example, if sweep radius $r_s = 40\% \text{ span}$, then layers from 0 to 60% span use straight leading edge values, and above 60% span the values for the round leading edge. The θ_0 at the hub is always 0. Figure A.3 shows an example of leading edge shape for $\lambda = 40^\circ$ and $r_s = 40\% \text{ span}$.

When the shape of the leading edge from the front view is known, its meridional view is established. The position of the leading at the hub is fixed with a radius $r_h = 10\text{mm}$ and axial position of $z_h = 6.25\text{mm}$, as it is in the case of the baseline design.

The meridional profile of the leading edge is also made of two parts, one being a part of a straight and the other a part of an ellipse. In order to simplify the calculations the ellipse part is treated as a straight line. This simplification introduces an error in the calculation of the blade length, however it remains below 5% even in the worst case scenario. The coordinates

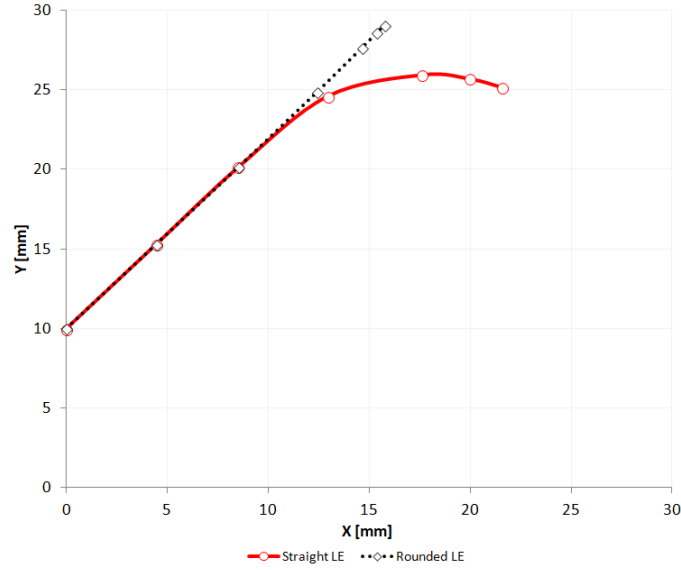


Figure A.3: Example of leading edge shape for $\lambda = 40^\circ$ and $r_s = 40\%$ span.

r_2, z_2 of a transition point are calculated from a straight line equation defined in the following way:

$$\begin{aligned} r_n &= \tan(90^\circ - \frac{\lambda}{7})z_n + b_n \\ b_n &= r_h - \tan(90^\circ - \frac{\lambda}{7})z_h \end{aligned} \quad (\text{A.16})$$

then:

$$\begin{aligned} r_2 &= r_t - r_s \\ z_2 &= \frac{r_2 - b_n}{\tan(90^\circ - \frac{\lambda}{7})} \end{aligned} \quad (\text{A.17})$$

$$\begin{aligned} r_t &= 33.25\text{mm} \\ z_t &= z_2 + 0.4r_s \end{aligned}$$

This allows to calculate the coefficients defining the second part of the straight:

$$\begin{aligned} a_t &= \frac{r_t - r_2}{z_t - z_2} \\ b_t &= r_2 - a_t z_2 \end{aligned} \quad (\text{A.18})$$

The leading edge coordinates are calculated for all previously defined layers. This position is required to establish the length of the blade at each layer which is used to determine the θ angle distribution along the meridional distance along the blade, denoted as $\theta(M)$. First, the blade angle distribution at the tip is calculated. Because the tip is cylindrical, meridional distance is equal to the axial distance. The distribution at the tip must fulfil four conditions:

- Correct θ_0 angle resulting from the previously calculated leading edge shape
- Correct inlet angle β_1 according to the chosen value of incidence angle

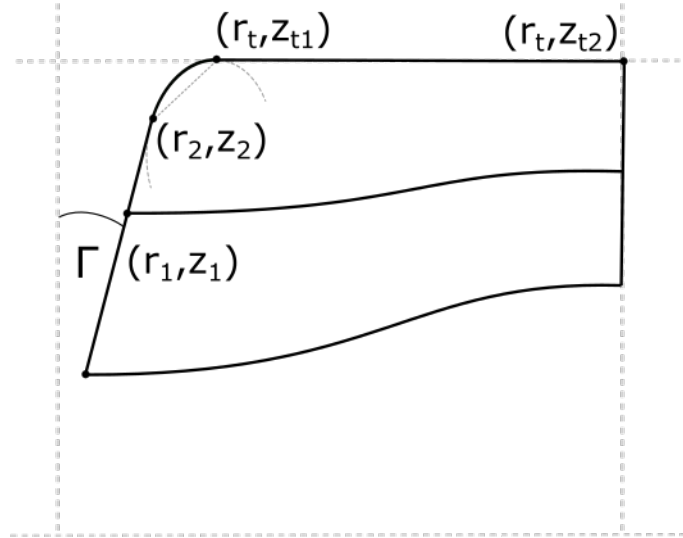


Figure A.4: Coordinates of the most important points defining the meridional view of an inducer.

- Correct outlet angle β_2 according to the baseline design
- Correct solidity s at the tip according to the chosen value

First three conditions can be expressed as a system of equations:

$$\begin{aligned}\theta(0) &= \theta_0 \\ \frac{d\theta}{dM}(0) &= \frac{\tan\beta_1}{r_t} \\ \frac{d\theta}{dM}(M_{max}) &= \frac{\tan\beta_2}{r_t}\end{aligned}\tag{A.19}$$

With three conditions a second order polynomial can be defined:

$$\begin{aligned}\theta(M) &= aM^2 + bM + c \\ \frac{d\theta}{dM} &= 2aM + b\end{aligned}\tag{A.20}$$

The a,b and c coefficient can be calculated:

$$\begin{aligned}a &= \frac{\left(\frac{\tan\beta_1}{r_t} - b\right)}{2M_{tmax}} \\ b &= \frac{\tan\beta_1}{r_t} \\ c &= \theta_0\end{aligned}\tag{A.21}$$

where M_{tmax} is equal to: $M_{tmax} = z_{t2} - z_{t1}$. z_{t1} is of course defined by the position of the leading edge while z_{t2} is calculated to achieve desired solidity at the tip. This is done in an iterative way. First the target blade length l is calculated:

$$l = \frac{2\pi r_t}{n}\tag{A.22}$$

where n is the number of blades. Then a certain value of z_{t2} is assumed, in this case 46.5mm taken from the baseline design. Now the $\theta(M)$ function is known and the length of the blade can be calculated. The change of the blade length is given as:

$$dl = \sqrt{(r_t d\theta)^2 + dz^2} \quad (\text{A.23})$$

To avoid integrating the length of the blade is divided into 20 pieces and the length of each piece is calculated separately. The full length is a sum of lengths of individual pieces. If the calculated length is too small then the trailing edge is moved backwards and of course opposite happens if it is too big. The search is done by a built-in Excel function that minimises the difference between the target and calculated value. Finally the value of θ_2 at the trailing edge may be calculated. In order to have a radial trailing edge this value must be maintained for all the other layers.

To calculate blade angle distribution at other layers once again a polynomial function was used, but this time a fourth order one. This is because one more condition must be fulfilled, regarding the θ at the outlet. The θ angle is also no longer an explicit function of the meridional distance along the blade, but instead is a function of a fraction of a distance along the blade, denoted as k . This change was made because at other layers the radius is not constant and the value of dM changes along the blade.

$$\theta(k) = ak^3 + bk^2 + ck + d \quad (\text{A.24})$$

To calculate the coefficients the following equations are used:

$$\begin{aligned} \theta(0) &= \theta_0 \\ \theta(1) &= \theta_2 \\ \frac{d\theta}{dk}(0) &= \frac{\tan\beta_1 dM(0)}{r(0)} \\ \frac{d\theta}{dk}(1) &= \frac{\tan\beta_2 dM(1)}{r(1)} \end{aligned} \quad (\text{A.25})$$

To calculate $r(k)$ and $dM(k)$ distributions used to calculate this coefficients the blade is divided into 20 pieces along the axial direction. The radius is calculated according to the chosen spanwise location:

$$\begin{aligned} r_n(z) &= n(r_t - r_h(z)) + r_h(z) \\ r_h(z) &= 2.92 \cdot 10^{-7} z^5 - 3.61 \cdot 10^{-4} z^4 + 0.0014 z^3 - 0.0138 z^2 + 0.0537 z + 10 \end{aligned} \quad (\text{A.26})$$

where n is the percentage of span and $r_h(z)$ is a function describing how hub radius changes along the blade, based on the hub of the baseline design. The values of M are then calculated by adding ΔM to the value of M from the previous fraction of a blade:

$$\begin{aligned} M(0) &= 0 \\ M(z + \Delta z) &= M(z) + \Delta M = M(z) + \sqrt{\Delta z^2 + \Delta r^2} \\ dM(z) &\approx \Delta M \end{aligned} \quad (\text{A.27})$$

The coefficients may now be represented as:

$$\begin{aligned}d &= \theta_0 \\c &= \frac{\tan\beta_1\Delta M(0)}{r(0)} \\b &= \frac{\tan\beta_2\Delta M(1)}{r(1)} + 3\theta_2 - 2c - 3d \\a &= \theta_2 - b - c - d\end{aligned}\tag{A.28}$$

The calculated distribution is then transferred to Design Modeller, where it is translated to the 3D shape.

B

Test loop components specifications



Inverter		Test pump	
			
Manufacturer	Fuji Electric	Manufacturer	Teral
Model	FREQROL-A700	Model	SJ-65×50L63.7
Rated power	10kVA	Flow rate	0.25 - 0.7 m ³ /min
		Total head	7.5 - 16 m

Table B.1: Inverter and test pump specifications.



Vacuum pump		Booster pump	
			
Manufacturer	ULVAC	Manufacturer	Teral
Model	DTP-180S	Model	LP65B61.5
Flow rate	198 l/min	Flow rate	0.28 - 0.7 m ³ /min
Min. suction pressure	4 kPa	Total head	7.5 - 16 m

Table B.2: Vacuum and booster pump specifications.



Inlet pressure sensor		Differential pressure sensor Head measurement	
			
Manufacturer	Kyowa Electric	Manufacturer	Kyowa Electric
Model	PGMC-A-200KP	Model	PDU - A - 1 MP
Type	strain gauge	Type	strain gauge
Rated capacity	200 kPa	Rated capacity	200 kPa
Rated output	0.6 mV/V	Rated output	1.5 mV/V
Nonlinearity	Within 1.5% RO	Nonlinearity	Within 0.2% RO
Hysteresis	Within 1.5% RO	Hysteresis	Within 0.2% RO

Table B.3: Inlet pressure sensor and differential pressure sensor specifications.



Differential pressure sensor Flow rate measurement		Torque transducer	
			
Manufacturer	Nagano Keiki	Manufacturer	Kyowa Electric
Model	GC50	Model	TPS-A-100NM
Type	silicon capacitance	Rated capacity	± 100 Nm
Rated capacity	± 100 kPa	Rated output	± 5 V ± 0.2 V
Rated output	4-20 mA DC	Nonlinearity	Within 0.3% RO
Output accuracy	$\pm 0.5\%$ F.S.	Hysteresis	Within 0.3% RO
Responsiveness	< 2 s	Max. bending moment	15 Nm
		Max. shaft load	600 N

Table B.4: Differential pressure sensor (used for flow rate measurements) and torque transducer (used for efficiency measurement) specifications.

Bibliography

- [1] Avio. *LIQUID-OXYGEN TURBOPUMP VULCAIN*. <http://www.avio.com/en/ariane/ariane-6/vulcain-2-turbopomp/>. [Accessed 2017-11-19].
- [2] A. J. Sobin and W. R. Bissel. *Turbopump Systems for Liquid Rocket Engines*. NASA, 1974.
- [3] R. Bosson, P. Sabin, and G. Turin. Improvements of the hydrogen turbopump for the vulcain 2 engine. Los Angeles, 1999. 35th AIAA/ASME/SAE/ASEE Joint Propulsion Conference and Exhibit.
- [4] A.J. Acosta. Experimental study on cavitating inducers. In *Proceedings from Second Symposium on Naval Hydrodynamics*, Washington, D.C., 08 1958.
- [5] J. F. Gulich. *Centrifugal pumps*. Springer, Berlin, 2008.
- [6] G. P. Sutton and O. Biblarz. *Rocket propulsion elements*. John Wiley and Sons, New York, 2001.
- [7] C. E. Brennen. *Hydrodynamics of pumps*. Oxford University Press, 1994.
- [8] A. A. Sonin. *The Physical Basis of Dimensional Analysis*. Department of Mechanical Engineering MIT, Cambridge, 2001.
- [9] S. L. Dixon. *Fluid Mechanics Thermodynamics of Turbomachinery*. Butterworth-Heinemann, Oxford, 1998.
- [10] Y. Nakatama. *Introduction to Fluid Mechanics*. Butterworth-Heinemann, Oxford, 2000.
- [11] *Effect of blade outlet angle*. http://nptel.ac.in/courses/112104117/chapter_8/8_6.html, 2009. [Accessed 2017-12-05].
- [12] J. M. Chapallaz, P. Eichenberger, and G. Fischer. *Manual on Pumps Used as Turbines*. Gesellschaft für Technische Zusammenarbeit, 1992.
- [13] d’Agostino et al. An introduction to cavitation in inducers and turbopumps. In Salvetti M. V. d’Agostino L., editor, *Cavitation Instabilities and Rotordynamic Effects in Turbopumps and Hydroturbines*, chapter 1. Springer, Cham, 2017.
- [14] S. S. Rao. *Engineering Optimization: Theory and Practice*. John Wiley and Sons, New Jersey, 2009.
- [15] J. Onoue, A. Okamoto, M. Hayakawa, and Y. Kawata. Study on improvement of suction performance for industrial pumps by applying splitter blade. *Turbomachinery*, 44(2):73–80, 2016.
- [16] A. Furukawa and K. Ishizaka. *Inducer design and instability phenomena*. Japan Society of Mechanical Engineers RC 178, 2002.

- [17] F. Torre and S. Konno. Design optimisation of splitter blades for rocket engine turbopump. Oslo, 2018. ASME 2018 Turbo Expo.
- [18] R. W. Westra. *Inverse-design and optimization methods for centrifugal pump impellers*. Gildeprint, 2006.
- [19] H. Watanabe and H. Tsukamoto. Design optimization of cryogenic pump inducer considering suction performance and cavitation instability. Hamamatsu, Japan, 2011. ASME-JSME-KSME 2011 Joint Fluids Engineering Conference.
- [20] S. Kim, K. Lee, J. Kim, and Y. Choi. A numerical study on the improvement of suction performance and hydraulic efficiency for a mixed-flow pump impeller. *Mathematical Problems in Engineering, Volume 2014*, 2014.
- [21] T. Krátký, L. Zavadil, and V. Doubrava. Cfd and surrogates-based inducer optimization. *International Journal of Fluid Machinery and Systems, Vol. 9, No. 3*, 2016.
- [22] F. Torre. Design optimisation of splitter blades for a rocket engine turbopump. Master's thesis, Delft University of Technology, Delft, the Netherlands, 2018.
- [23] D.K. Huzel and D.H. Huang. *Design of liquid propellant rocket engines*. NASA, 1967.
- [24] J. K. Jakobsen. *Liquid Rocket Engine Turbopump Inducers*. NASA, 1971.
- [25] R. B. Furst. *Liquid Rocket Engine Centrifugal Flow Turbopumps*. NASA, 1973.
- [26] Martin Seidl, Jiří Šafka, Jiri Bobek, Luboš Běhálek, and Jiri Habr. Mechanical properties of products made of abs with respect to individuality of fdm production processes. *MM Science Journal*, 2017:1748–1751, 02 2017.
- [27] 3D Printing Systems Limited. *UP Plus 2 User Manual*. 2013.
- [28] A. J. Acosta, Y. Tsujimoto, Y. Yoshida, S. Azuma, and P. Cooper. Effects of leading edge sweep on the cavitating characteristics of inducer pumps. *International Journal of Rotating Machinery*, 7(6):397–404, 2001.
- [29] M. Arpit and P. Ghosh. Effect of leading edge sweep on the performance of cavitating inducer of lox booster turbopump used in semicryogenic engine. *IOP Conference Series: Materials Science and Engineering*, 2017.
- [30] F. Bakir, S. Kouidri, R. Nogra, and R. Rey. Experimental analysis of an axial inducer influence of the shape of the blade leading edge on the performances in cavitating regime. *Journal of Fluids Engineering*, 2003.
- [31] Ansys Inc. *Ansys Workbench 17.1 User Guide*. 2016.
- [32] E. Goncalves and R. F. Patella. Numerical simulation of cavitating flows with homogeneous models. *Computers and Fluids*, 38:1682–1696, 2009.
- [33] I. Senocak and W. Shyy. A pressure-based method for turbulent cavitating flow computations. *Journal of Computational Physics*, 176:363–383, 2002.
- [34] M. Deshpande, J. Feng, and C. L. Merkle. Numerical modeling of the thermodynamic effects of cavitation. *Journal of fluids engineering*, 119:420–427, 1997.
- [35] J. Friedrichs and G. Kosyna. Rotating cavitation in a centrifugal pump impeller of low specific speed. *Journal of Fluids Engineering - Transactions of The Asme*, 124, 06 2002.